ABSTRACT

EXPERIMENTAL TECHNIQUE FOR STUDYING HIGH-TEMPERATURE PHASE EQUILIBRIA IN REACTIVE MOLTEN METAL BASED SYSTEMS

by
Alexandre Ermoline

The general objective of this work is to develop an experimental technique for studying the high-temperature phase compositions and phase equilibria in molten metal-based binary and ternary systems, such as Zr-O-N, B-N-O, Al-O, and others. A specific material system of Zr-O-N was selected for studying and testing this technique.

The information about the high-temperature phase equilibria in reactive metal-based systems is scarce and their studying is difficult because of chemical reactions occurring between samples and essentially any container materials, and causing contamination of the system.

Containerless microgravity experiments for studying equilibria in molten metal-gas systems were designed to be conducted onboard of a NASA KC-135 aircraft flying parabolic trajectories. A uniaxial apparatus suitable for acoustic levitation, laser heating, and splat quenching of small samples was developed and equipped with computer-based controller and optical diagnostics. Normal-gravity tests were conducted to determine the most suitable operating parameters of the levitator by direct observations of the levitated samples, as opposed to more traditional pressure mapping of the acoustic field. The size range of samples that could be reliably heated and quenched in this setup was determined to be on the order of 1-3 mm. In microgravity experiments, small spherical specimens (1-2 mm diameter), prepared as pressed, premixed solid components, ZrO_2, ZrN, and Zr powders, were acoustically levitated inside an argon-filled chamber at one atmosphere

and heated by a CO_2 laser. The levitating samples could be continuously laser heated for about 1 sec, resulting in local sample melting. The sample stability in the vertical direction was undisturbed by simultaneous laser heating. Oscillations of the levitating sample in the horizontal direction increased while it was heated, which eventually resulted in the movement of the sample away from its stable levitation position and the laser beam.

The follow-up on-ground experiments were conducted to study phase relations in the Zr-O-N system at high-temperatures. Samples with specific compositions were laser-heated above the melt formation and naturally cooled. Recovered samples were characterized using electron microscopy, energy-dispersive spectroscopy, and x-ray diffraction. Results of these analyses combined with the interpretations of the binary Zr-O and Zr-N phase diagrams enabled us to outline the liquidus and the subsolidus equilibria for the ternary $Zr-ZrO_2-ZrN$ phase diagrams.

Further research is suggested to develop the microgravity techniques for detailed characterization of high-temperature relations in the reactive, metal based systems.

EXPERIMENTAL TECHNIQUE FOR STUDYING HIGH-TEMPERATURE PHASE EQUILIBRIA IN REACTIVE MOLTEN METAL BASED SYSTEMS

by
Alexandre Ermoline

A Dissertation
Submitted to the Faculty of
New Jersey Institute of Technology
in Partial Fulfillment of the Requirements for the Degree of
Doctor of Philosophy in Mechanical Engineering

Department of Mechanical Engineering

January 2005

APPROVAL PAGE

EXPERIMENTAL TECHNIQUE FOR STUDYING HIGH-TEMPERATURE PHASE EQUILIBRIA IN REACTIVE MOLTEN METAL BASED SYSTEMS

Alexandre Ermoline

Dr. Edward L. Dreizin, Dissertation Advisor   Date
Professor of Mechanical Engineering, NJIT

Dr. Boris Khusid, Committee Member   Date
Associate Professor of Mechanical Engineering, NJIT

Dr. Kurt Sacksteder, Committee Member   Date
Senior Scientist, NASA Glenn Research Center, Cleveland, OH

Dr. Mirko Schoenitz, Committee Member   Date
Research Assistant Professor of Mechanical Engineering, NJIT

Dr. Chao Zhu, Committee Member   Date
Associate Professor of Mechanical Engineering, NJIT

BIOGRAPHICAL SKETCH

Author: Alexandre Ermoline

Degree: Doctor of Philosophy

Date: January 2005

Undergraduate and Graduate Education:

- Doctor of Philosophy in Mechanical Engineering,
  New Jersey Institute of Technology, Newark, NJ, 2005

- Master of Science in Engineering Physics,
  Tomsk State University, Tomsk, Russia, 1995

Major: Mechanical Engineering

Presentations and Publications:

A. Ermoline, M. Schoenitz, V. Hoffmann, and E. L. Dreizin. (2004). Experimental Technique for Studying High-Temperature Phases in Reactive Molten Metal-Based Systems, *Review of Scientific Instruments, 75*, 5177-5185.

A. Ermoline, M. Schoenitz, V. Hoffmann, and E. L. Dreizin. (2004). Experimental Technique for Studying High-Temperature Phases in Reactive Molten Metal-Based Systems, *AIAA Paper 2004-1310*.

Y. L. Shoshin, A. Ermoline, and E. L. Dreizin. (2003). Effect of Aluminum Particle Size and Surface Morphology on the Laminar Aerosol Flame Speed. *The 2003 Technical Meeting of the Eastern States Section of the Combustion Institute*, 321-324.

A.Ermoline, M.Schoenitz, and E.L.Dreizin. (2002). Experimental Technique for the Study of High-Temperature Phase Equilibria in Reactive Molten Metal-Based Systems. *Proceedings of 2002 Microgravity Materials Science Conference*, 178-187.

A. Ermoline, M. Schoenitz, E. L. Dreizin, and N. Yao. (2002). Production of Carbon-Coated Aluminum Nanopowders in Pulsed Microarc Discharge. *Nanotechnology, 13*, 638-643.

A.Ermoline, Y. Shoshin, and E. L. Dreizin. (2001). Production of Coated Aluminum Nanopowders in Pulsed Microarc Discharge. *The 2001 Technical Meeting of the Eastern States Section of the Combustion Institute*, 288-291.

A. Ermoline, S. S. Rybanin, N. I. Peregudov. (1996). Heterogeneous Self-Ignition of the Metal Slab at Internal and External Diffusional Regimes. *The 11th International Symposium on Combustion and Explosion, Chernogolovka, Russia.*

S. S. Rybanin, N. I. Peregudov, A. Ermoline. (1996). Numerical Modeling of the Spot Ignition and Arising of the Heterogeneous Combustion. *11th International Symposium on Combustion and Explosion, Chernogolovka, Russia.*

To my wife, **Irina**, and to my sons
Dennis and Anthony

ACKNOWLEDGMENT

I am indebted to many people who helped and inspired me in many direct and indirect ways during my work on this project. First and foremost, I would like to express my deepest appreciation to my advisor, Professor E.L. Dreizin. for his encouragement, support and strengthening my resolve. Many times his insight and incredible intuition helped me to find the right direction in my research.

Special thanks are given to my committee members, Dr. B. Khusid, Dr. K. Sacksteder, Dr. M. Schoenitz and Dr. C. Zhu for their help and interest in my work, reading the original manuscript and providing valuable suggestions.

I owe a special debt to Dr. M. Schoenitz whose partner I had a pleasure to be in conducting microgravity experiments onboard a KC-135 aircraft in Houston, TX. Dr. M. Schoenitz taught me many secrets in materials characterizations techniques, such as microscopy or XRD, that can not be learned from textbooks but only by working with an expert.

Dr K. Sacksteder's (NASA Glenn Research Center, Cleveland, OH) support and assistance in experimental hardware design and safety evaluation are gratefully acknowledged. My sincere gratitudes go to the NASA JSC microgravity crew led by John Yaniec for their help and guidance during experiments in zero-g conditions.

My colleagues, members of Dr. Dreizin's research group, deserve special recognition. Assistance of V.Hoffmann in designing and building the experimental setup hardly could be overestimated. His great contribution to the structural analysis of the experimental setup must also be acknowledged here. Thanks to S. Jones for many valuable suggestions concerning the experimental apparatus design. I'm very greateful to

Dr. Y. Shoshin and M. Trunov for their constructive criticism and extremely helpful discussions. I also wish to express my appreciation to my fellow NJIT students and friends S. Umbrajakar and X. Zhu who were always ready to help me in different situations.

Finally, my eternal gratitude goes to my wife, Irina, for her patience, encouragement and love.

TABLE OF CONTENTS

LIST OF TABLES

LIST OF FIGURES

NOMENCLATURE

A – area

a – constant

b – constant

a_0 – lattice parameter, length

b_0 - lattice parameter, length

c - specific heat (in Chapter 4), maximum distance from the neutral axis (in Appendix A), constant (in Appendix C)

c_0 - lattice parameter, length

c_i - fraction of the load carried by member i

d – diameter

D – diffusivity

d_i - distance from a line to the point i

dx - tangential distortion

E - modulus of elasticity (Young's modulus)

f_x - x-component of a 'reduced' focal length in pixels

f_y - y-component of a 'reduced' focal length in pixels

h - heat transfer coefficient

I - area moment of inertia

i – number of iteration

J - moment of inertia

k - effective spring rate

l – distance

$$\mathbf{M} = \begin{pmatrix} f_x & 0 & x_o \\ 0 & f_y & y_0 \\ 0 & 0 & 1 \end{pmatrix}$$ - calibration matrix

of a camera

M - moment of force

MS - margin of safety

MS_{UBR} - margin of safety with respect to the ultimate bearing strength

MS_{US} - margin of safety with respect to the ultimate shear strength

MS_{UT} - margin of safety with respect to the ultimate tensile strength

MS_{YBR}- margin of safety with respect to the yield bearing strength

MS_{YS} - margin of safety with respect to the yield shear strength

MS_{YT} - margin of safety with respect to the yield tensile strength

Nu - Nusselt number

P - load, usually applied to the whole structure

p - pressure

Q - laser power

$$r^2 = \left(\frac{X_c}{Z_c}\right)^2 + \left(\frac{Y_c}{Z_c}\right)^2$$

R - rotation matrix

R - universal gas constant (in Chapter 4), reaction or load (in Appendix A)

R$_L$ - rotation matrix describing position of the left camera reference frame relative to the world camera reference frame

R$_{RL}$ - rotation matrix describing position of the right camera reference frame relative to the left camera reference frame

R$'$ - reflection matrix

R_S - shear load

R_T - tensile load

S - surface area

s_1, s_2, s_2, s_3, s_4, s_5 - distortion coefficients

S_{BRU} - ultimate bearing strength

S_{BRY} - yield bearing strength

S_{US} - ultimate shear strength

S_{UT} - ultimate tensile strength

S_{YT} - yield tensile strength

T - temperature

t - time

T - translation matrix

T_0 - environment temperature, initial temperature

T$_L$ - translation matrix describing position of the left camera reference frame relative to the world camera reference frame

T_m - melting temperature

T$_{RL}$ - translation matrix describing position of the right camera reference frame relative to the left camera reference frame

V - volume

$$\mathbf{X_c} = \begin{pmatrix} X_c \\ Y_c \\ Z_c \end{pmatrix}$$ - coordinates in camera reference frame

$$\mathbf{X_w} = \begin{pmatrix} X_w \\ Y_w \\ Z_w \end{pmatrix}$$ - coordinates in world reference frame

x_0 - pixel coordinate x_p of a camera principal point

$$\mathbf{x_d} = \begin{pmatrix} x_{d1} \\ x_{d2} \\ 1 \end{pmatrix}$$ - distorted coordinates

x$_d$ - distorted pixel image coordinates of a point

X$_L$ - coordinates in the left camera reference frame

NOMENCLATURE
(Continued)

$$\mathbf{x_n} = \begin{pmatrix} \dfrac{X_c}{Z_c} \\ \dfrac{Y_c}{Z_c} \\ 1 \end{pmatrix}$$ - normalized coordinates in camera reference frame

$$\mathbf{x_p} = \begin{pmatrix} x_p \\ y_p \\ 1 \end{pmatrix}$$ - pixel coordinates of projection of a point on camera image

$\mathbf{x_{nl}}$ - normalized coordinates in the left camera reference frame

$\mathbf{x_{nr}}$ - normalized coordinates in the right camera reference frame

$\mathbf{X_R}$ – coordinates in the right camera reference frame

y_0 - pixel coordinate y_p of a camera principal point

γ - lattice parameter, angle

ε – emissivity

ρ – density

λ_g - gas thermal conductivity

σ – stress

σ_I - principal tensile stress

σ_{BR} - bearing stress

σ - Stephan-Boltzmann constant

τ - shear stress

τ_1 - principal shear stress

CHAPTER 1

INTRODUCTION

1.1 Statement of the Problem

Phase transitions and equilibria in metal-based systems at elevated temperatures have been widely explored in the past (Massalski et al.,1990, Levinski, 1990, Okamoto and Massalski, 1994). However, the phase equilibria existing at the high temperatures in the molten, metal-based systems that contain chemically active components with greatly different melting temperatures, such as Al-O-N, Mg-O, Zr-O-N, Ti-C-O-N, B-C-O, etc., are not well known. Knowledge of the phase equilibria in these systems is important for both fundamental understanding of mechanisms of interaction between metal and gas atoms in various melts/solutions and for development of many material processing technologies. For example, new ionic conductors based on zirconium (and other transition metals), oxynitrides and doped zirconium oxides are being developed for use in oxygen sensors and fuel cells (Chiacci et al., 1994, Kartha and Grimes, 1994). These devices are often employed at elevated temperatures at which the stability of the known oxynitride phases is not well known. Knowledge of the high-temperature phase equilibria for the boron-oxygen and boron-carbon-oxygen systems is essential for development and fabrication of many new semiconductors, glasses, and ultra-hard materials (Zehringer et al., 1990, Kervalishvili et al., 1992, Belyanski et al., 1995).

Understanding of systems of metals with their respective oxides, nitrides, and carbides is also critical for modeling of combustion mechanisms of high-energy density materials used in propellants, explosives, and incendiaries. Recent research has shown
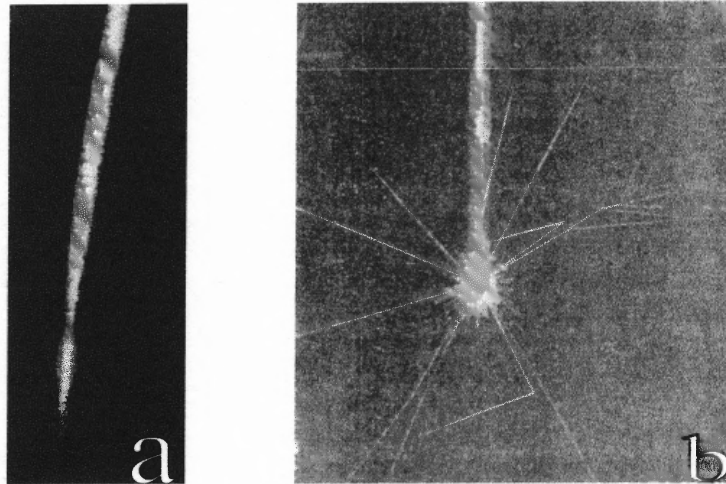
Figure 1.1 Photographed streaks of the free-falling particles burning in air: (a) boron (b) zirconium.

that phase transitions occurring in molten metal-gas systems can play significant role in metal combustion processes. Explosions of burning metal particles and brightness jumps were observed in metal particle combustion as illustrated in Figure 1.1, where photographs of the streaks of burning metal particles are presented. These phenomena can be explained taking into account the phase transitions in burning particles (Price, 1984, Nelson, 1965, Nelson et al., 1968, Dreizin et al., 1993, Dreizin, 1996, Molodetsky et al., 1997, Molodetsky et al., 1998). Most of the phase transition processes occurring in such systems are not well known and the basis on which they are described is the elemental analysis of the partially burned and rapidly quenched metal particles. Using this approach, it was shown that the non-stoichiometric metal-gas phases including supersaturated metal-gas solutions, e.g. aluminum-oxygen (Dreizin, 1996, Dreizin, 1998), zirconium-oxygen, titanium-oxygen-nitrogen (Molodetsky et al., 1997, Molodetsky et al., 1998), and boron-oxygen-carbon (Dreizin et al., 1997) are produced within burning metal particles.

One reason for the lack of data on the high temperature phase equilibria in such systems is that their studying is difficult: reactions occur between samples and essentially any container materials and cause contamination. This work is an attempt to develop a new technique for studies of such reactive systems using containerless sample processing at high temperatures followed by rapid quenching of the samples and their subsequent studying at room temperature.

1.2 Background Information

1.2.1 Zirconium-Oxygen-Nitrogen System

Experiments in which zirconium particles burned in air (Molodetsky et al., 1997) indicated that both oxygen and nitrogen are dissolved in pure molten zirconium. The particles which burned in the 2400-2700 K temperature range (higher than the Zr melting point of 2125 K), were quenched by impinging onto aluminum foil. This method gives a rapid cooling rate ($\sim 10^5$ K/s) and minimal particle deformation. The internal composition history of burning Zr was determined by analyzing many identically produced and ignited particles that were quenched after different combustion times. Examples of micrographs of 240 µm initial diameter Zr particles quenched after a period of combustion are shown in Figure 1.2 (Molodetsky et al., 1997). The results of elemental analyses for the same particles produced using energy-dispersive spectroscopy are shown in Figure 1.3. The particles quenched in a foil were fairly uniform in both morphology and composition. A particle that burned for the same time period but quenched slower, by cooling in Ar is also shown in Figure 1.2 and respective elemental analyses are shown in Figure 1.3. Comparison of the results for particles quenched from the same initial state with different
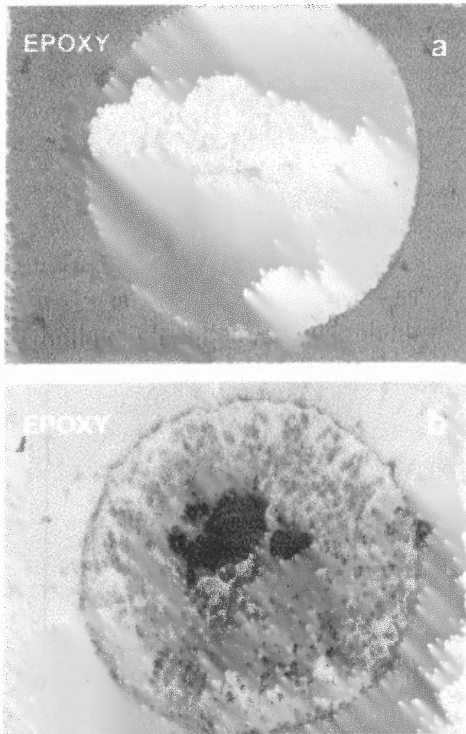
Figure 1.2 Cross-sections of 240 μm diameter Zr particles partially burned in air (Molodetsky et al., 1997): a) rapidly quenched on aluminum foil after ~180 ms of combustion; b) slowly quenched in argon gas after ~120 ms of combustion.
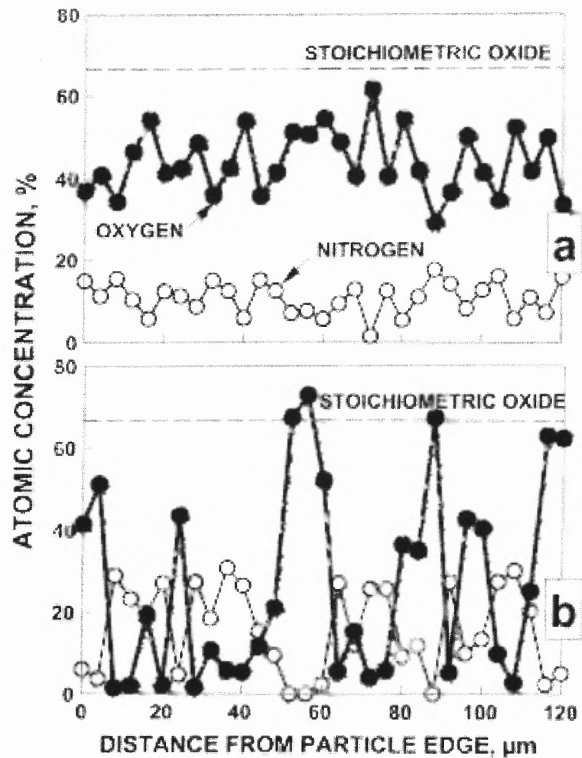
Figure 1.3 Radial oxygen and nitrogen atomic concentrations measured for particles shown in Figure 1.2 (Molodetsky et al., 1997).

techniques shows that the rapid cooling rate suppressed phase separation and, essentially, froze the composition of the burning liquid particle. The particle bulk composition history is shown in Figure 1.4. The observed trends indicate that the rate of nitrogen dissolution was initially higher than that of oxygen but this rate attained a maximum and was decreased later during combustion. The observed decrease in the dissolved nitrogen concentration indicated a solubility limit for nitrogen in the molten Zr-O-N system.
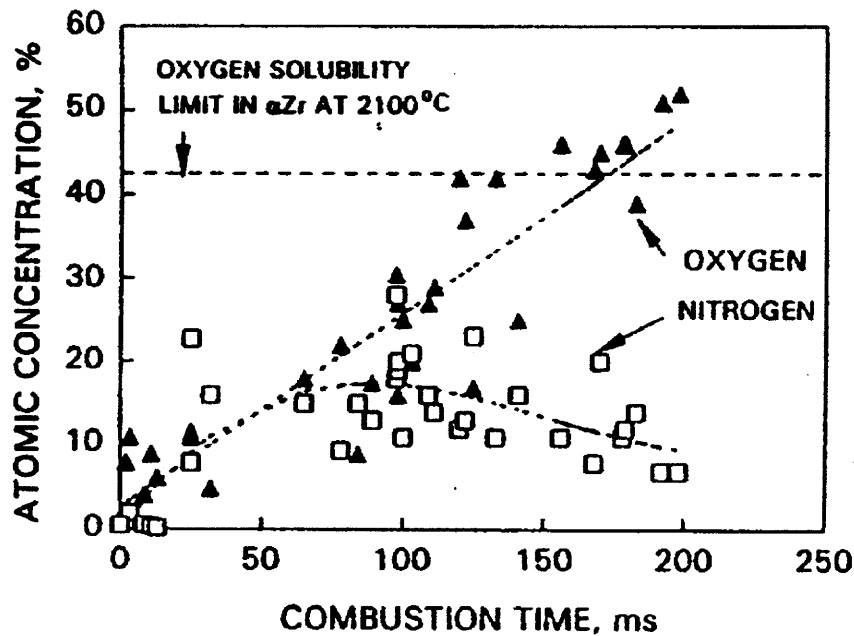
Figure 1.4 Internal composition history of 240 μm diameter Zr particles burning in air (Molodetsky et al.,1997).

At a temperature close to 2340 K, the eutectic transition in the binary Zr-O system, the burning particles exploded with a popping sound indicative of a gas release. After explosion, stoichiometric ZrO_2 was found in the fragmented combustion products. Based on these observations, the following scenario was formulated: both oxygen and nitrogen dissolve in the molten zirconium and produce a liquid solution in which the solubility limits for oxygen and nitrogen are different. At a temperature close to the eutectic in binary Zr-O system (2340 K), a phase transition occurs in the Zr-O-N system producing a solid zirconium-oxygen solution, nitrogen gas and zirconium oxide. Dissolved nitrogen concentration indicates the solubility limit for nitrogen in the molten Zr-O-N system which previously has not been reported in the literature.

1.2.2 Boron-Oxygen-Carbon System

A recent study of ignition and combustion of electrically heated boron filaments (Dreizin et al., 1997) showed that they burned in two distinct stages, consistent with earlier boron particle combustion studies (Li, 1990, Li and Williams, 1990, King, 1993). The onset of stage one combustion always occurred in the same narrow temperature range of 1770 ± 70 K. It is known that two phase transitions, amorphous to β and α to β, rhombohedral boron structures occur in pure solid boron in the same temperature range. Surprisingly, analyses of the filaments quenched at the instant they reached 1770 K showed spherical voids (as shown in Figure 1.5) indicative of the production of both liquid and gaseous phases even though the boron melting point is 2350 K and is much higher than the experimental temperatures. The compositions measured in the cross-sections included boron, oxygen, and carbon (present in the original boron as an impurity). It was thus hypothesized that the presence of oxygen and carbon affected the phase transitions occurring in pure boron and resulted in the production of new liquid and gaseous phases. The filaments burned in two distinct stages separated by well-resolved in time optical signals. The transition from the stage one to stage two combustion was accompanied by the release of internal gas resulting in the formation of very large spherical voids (bubbles) in the boron filaments (shown in Figure 1.6). Significant amounts of dissolved oxygen were detected in the interiors of partially burned boron filaments quenched during the stage two combustion. These findings were interpreted as indicating that oxygen dissolution occurs in heterogeneous boron combustion in oxygen. They also suggest that the oxygen solubility limit was reached and exceeded so that a phase transition accompanied by the gas (e.g., BO_2 and/or BO) release occurred and produced large voids.
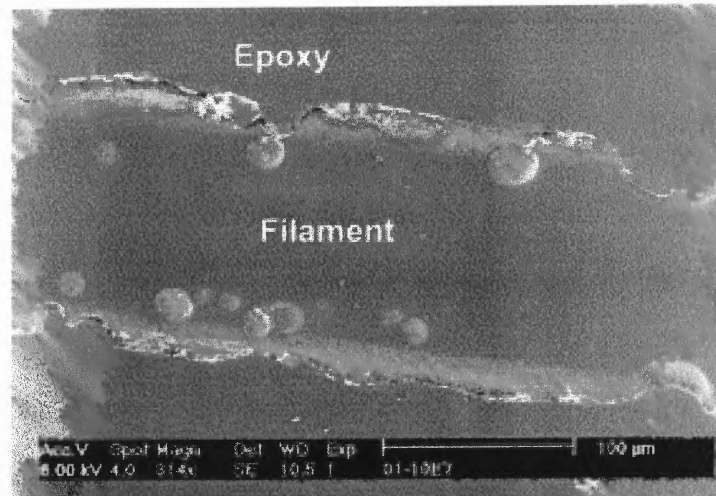
Figure 1.5 SEM image of the cross-section of a boron filament heated in air to 1770 K and quenched at the moment of stage one combustion onset (Dreizin, Keil et al., 1997).
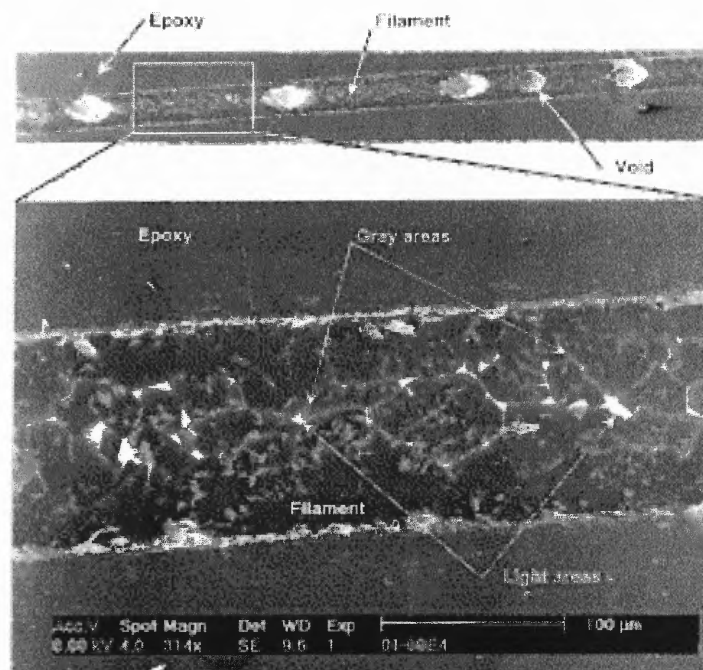
Figure 1.6 SEM image of the cross-section of a boron filament extinguished after the second-stage combustion in air (Dreizin, Keil et al., 1997).

1.3 Approach and Objectives

Detailed descriptions of the high temperature phase equilibria and phase transitions, similar to those described above are lacking as well as reliable and reproducible experimental data. Such data, as mentioned above should rely on experiments employing containerless techniques uniquely suited to deal with high-temperature, reactive materials systems. Containerless techniques use various types of forces to counteract gravity and levitate samples. These techniques become particularly useful under conditions of microgravity, reducing the role of the levitation forces to initial sample positioning and counteracting small residual gravity. Microgravity also eliminates natural convection and thus removes driving forces for phase segregation in systems with different phase densities. Therefore, it is proposed here to combine microgravity conditions with the containerless technique.

The general objective of this research is to develop an experimental technique for studying the high-temperature phase compositions and phase equilibria in molten metal-based binary and ternary systems. Specific objectives are to design and conduct containerless microgravity experiments addressing the phase equilibria in a selected metallic system. A NASA KC-135 aircraft flying parabolic trajectories was chosen as a platform for the microgravity experiments. Although the microgravity based technique that will be developed can be applied to many materials systems, we have selected a zirconium-oxygen-nitrogen system to be addressed in this work. This material system is of interest to applications in energetic materials, sensors, and fuel cells.

CHAPTER 2

DESIGN OF THE EXPERIMENT

2.1 Materials

Binary Zr-O and Zr-N diagrams are known fairly well (Massalski et al., 1990), however, information is scarce on phase equilibria in the ternary Zr-O-N system. While both zirconium oxide and nitride are refractory (melting points are 2710 and 3410 K, respectively), zirconium melts at a lower temperature, 2128 K, which makes the compounds containing Zr metal as a precursor much more difficult to study than the pseudo-binary ZrO_2–ZrN compounds used more often.

During the microgravity experiment, very high temperatures must be achieved within relatively short times. The available time for microgravity experiments is primarily constrained by the duration of a parabolic trajectory of the KC-135 aircraft (20-25 s). Consequently, samples masses are limited to those that can be heated and equilibrated in this period. High quench rates (about $10^5 - 10^6$ K/s) required to capture the sample compositions and structures representative of those at high temperatures, further limit the sample size.

Equilibria in the Zr-O-N system will be studied using samples prepared as pellets of premixed solid components, e.g., a mixture of ZrO_2, ZrN, and Zr powders. The compositions of the pellets are selected considering available information regarding binary and ternary phase diagrams Zr-O-N, Zr-O, Zr-N. The materials compositions targeted in the experiments are shown in Figure 2.1.
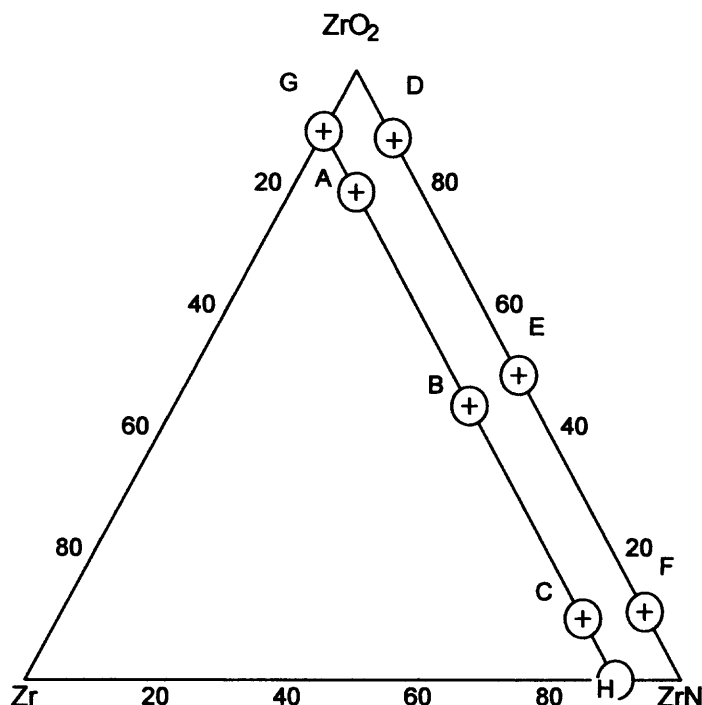
Figure 2.1 Targeted compositions chosen for the experiments.

2.2 Review of Available Containerless Techniques

Different containerless techniques were used in the past. A brief review is given below. It is aimed to justify selection of the acoustic levitation for this work.

2.2.1 Electromagnetic Levitation

<u>Principles.</u> This method allows one to levitate electrically conductive samples. A sample is placed between the coils with the AC current (Figure 2.2). The magnetic field of the coils induces currents inside the sample, which in turn interact with the magnetic field of the coils. As a result of this interaction, the electrodynamic forces stabilize the sample position between the coils.

<u>Advantages and achievements.</u> Electromagnetic levitation combined with heating allows one to study various conductive materials in their molten states. Some of the

applications of the electromagnetic levitation include studying of the crystallization behavior of the undercooled metals, semiconductors, and their alloys (Li et al.,1995, Zhang, 1998, Aoyama et al, 1998, Schenk et al.,1999), structural studies of undercooled metallic melts by X-ray diffraction (Notthoff et al.,1999), surface tension of molten droplets (Fujii, 2000), and various physical properties measurements of molten metals and metallic alloys (Shaefers et al., 1995, Schaefers and Frohberg, 1996, Langen et al., 1998).
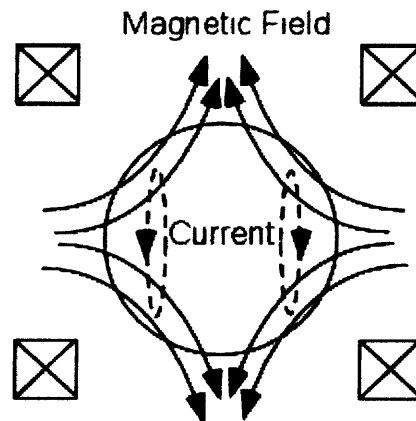
Figure 2.2 Electromagnetic levitation of a sample between coils.

Shortcomings and limitations. Some limitations exist for electromagnetic levitation: high electromagnetic fields are required, that deform the shape of a molten sample and induce turbulent currents inside the sample. In addition, because the required electromagnetic fields are strong, the sample is heated during levitation and it is hard to decouple the levitation and heating processes. The temperature measurement and control are also difficult. If it is necessary to keep a steady temperature regime, the sample must be cooled convectively using an inert gas. Because of the strong gas flow rate required,
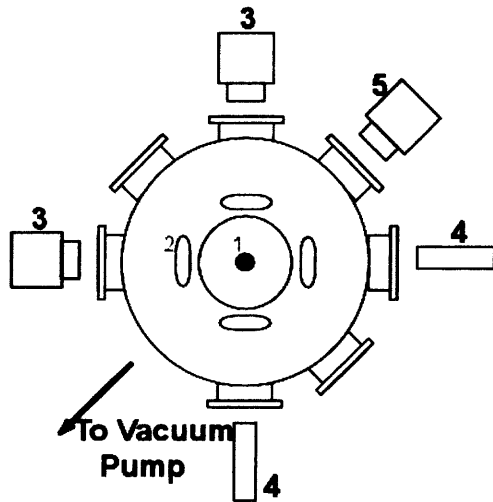
Figure 2.3 Schematic diagram of the electrostatic levitator. 1-Sample, 2-Side Electrodes, 3-Position Laser, 4- Position Detector, 5-Heating device (laser or xenon lamp).
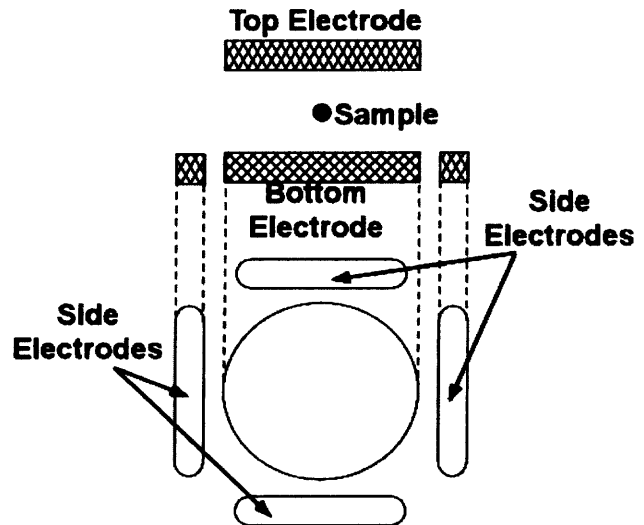
Figure 2.4 Electrode assembly of the electrostatic levitator.

only high purity gases should be used to minimize sample contamination. The significance of the above problems for coupled heating and levitation in microgravity can be reduced, but not completely eliminated. Unfortunately, this technique also provides poor access to the sample for it's quenching. Another serious limitation is that it can be used only with conductive samples.

2.2.2 Electrostatic Levitation

Principles. According to Earnshaw's theorem a charged sample placed in the electrostatic field cannot be in the stable equilibrium (Stratton, 1941). Therefore, to achieve the stability of a sample, a feedback loop is used that changes the electrostatic forces acting on the sample in response to its position. The changes are made in such a manner that the sample is kept at a fixed position. Figure 2.3 illustrates the principle on

which the electrostatic levitation is based. It shows schematically the electrostatic levitator which is similar to that described by Rhim et al. (1993). The device consists of two electrodes placed opposite to each other along the vertical axis and four side electrodes. The electrode assembly is shown in Figure 2.4. The charged sample is placed in the space between the top and the bottom electrodes. Two lasers and two position detectors provide the information about the sample position to a computer, and the computer sends corresponding control signals to the electrodes. The top and bottom electrodes control the vertical position of the sample, and the side electrodes prevent sample oscillations in the lateral direction.

The levitator described above is designed to work in the normal gravity environment. In the microgravity, a different electrode arrangement would be required. Because of the isotropic force environment of microgravity, for example, the tetrahedral configuration with four spherical electrodes can be used (Rhim et al., 1985).

Advantages and achievements. This technique can be used with both electrically conducting and insulating materials. It provides an open environment (as opposed, for example, to electromagnetic or aerodynamic levitation) that allows one to use easily various non-contact diagnostics. The electrostatic levitation is especially useful when the low-pressure environment is allowable or desirable. Sometimes, when the low pressure is necessary, it is the only levitation technique that can be used. It found many applications, such as measurements of thermophysical properties of molten refractory metals (Ishikawa et al., 2003; Paradis et al., 2003), studies of the undercooling and solidification behavior of liquid alloys (Kim et al., 1994) and metals (Sung et al., 2001), in situ x-ray diffraction studies of liquid alloy structure (Kelton et al., 2003), and crystal

growth (Sung et al., 2003). Samples of 2-3mm diameter were used and heated up to 3800 K (Paradis et al., 2003) in high vacuum.

Shortcomings and limitations. Compared to other levitation techniques the electrostatic levitation is, probably the most complex one. It requires a sophisticated feedback loop to stabilize the sample. Some provisions should be made for initial sample charging and maintaining its charge during the sample heating and melting (Ishikawa et al., 2001). The charge is changing during the heating. For example, the electrical charge decreased during heating resulting in the sample levitation failure described by Nakamura et al. (2002). Maintaining the charge is especially important during the sample melting or when other phase transformations occur inside the sample resulting in its inhomogeneity. As was shown theoretically, the electric field can also influence kinetic nucleation in dielectric materials and induce a shift in the glass transition temperature (Dobreva and Gutzow, 1997). The pressure requirements also limit applications of this method to a range of very low pressures (usually of the order 10^{-5} Pa) or at least moderate pressure to avoid the dielectric breakdown of gases. A study is currently in progress in NASA Marshall Space Flight Center where electrostatic levitation is attempted under a pressure of about 3 atm (Rogers et al., 2001). In the ultra-vacuum, even small amount of volatile component released from the specimen containing impurities, void volumes, or high vapor pressure materials, can result in the sample discharging and loss of the levitation capability (Sung et al., 2001). Additional problems caused by the gas release are discussed by Rogers et al. (2001) and include vapor deposition on the optical components of the chamber, impairing ultra violet charging of the sample, pyrometry and a system of sample position detection.

2.2.3 Aerodynamic Levitation

Principles. Aerodynamic levitation supports a sample by a fluid jet. Gas is blown

through a nozzle, a spherical sample is placed above the nozzle and is levitated as a result

of interaction of the gas flow and the sample. Numerous modifications of this method

with various nozzle geometries were used for the high-temperature materials processing

and study of their thermophysical properties. All the modifications of this technique use

one of two categories considered below.
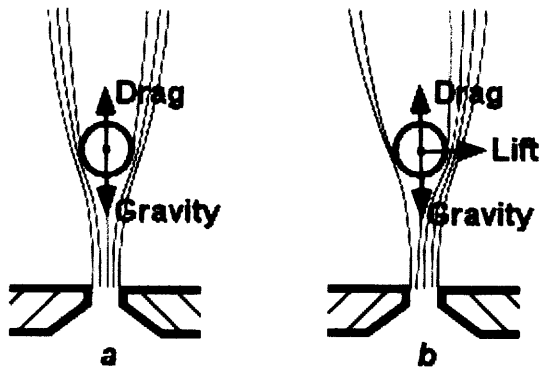
Figure 2.5 Forces exerted on a sample in an aerodynamic levitator.
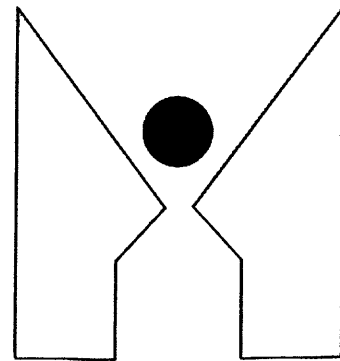
Figure 2.6 Levitation of a sample in an aerodynamic trap.

The first type of levitation uses a free jet. Figure 2.5 represents the idea of the

aerodynamic levitation and its physical principles. When gas passes over a spherical

sample, a drag force is produced. The drag force is exerted on the sample in the vertical

direction and is competing against the gravity force (Figure 2.5 a). With the increasing

distance from the nozzle, the jet diameter increases and drag force decreases. The sample

attains its equilibrium at the height where the drag force is equal to the gravity force

exerted on the sample. The levitation position is stable relative to vertical perturbations.

Indeed, any deviation of the sample from its equilibrium position in the vertical direction causes changes in the drag force that returns the sample into its equilibrium position.

Levitation is also stable in the transverse direction. When the sample is slightly displaced from the jet center, the fluid velocities are different on the sample sides. The speed is higher at the center of the jet. Hence, the lower pressure on this side exists and there is a lift force that shifts the sample back to the center of the jet (Figure 2.5 b).

The described technique cannot be used in microgravity because the gravity force is needed for the sample to be in the equilibrium position. A modification of this method allows one to levitate the sample in the zero-g environment. The gas jet is no longer free and an aerodynamic trap is created where the sample can be levitated even in the absence of the external forces. To produce the trap, the sample is placed inside an axisymmetrically expanding duct as Figure 2.6 shows (Paradis et al., 1996). Here, the change in the vertical position of the sample always leads to the restoring force. If the sample is displaced downstream, it enters the lower velocity zone. The distance between the diffuser's throat and the sample increases and the vortex generation is promoted. Formation of the vortices leads to a negative restoring force. If the sample is displaced upstream, it is exposed to a higher flow velocity, the distance from the diffuser decreases and the vertex generation is attenuated. The restoring force exerted on the sample shifts it back to the equilibrium position. The stability in the axial direction can be explained similar to the free jet.

Advantages and achievements. This technique is, probably, the simplest one of all the available levitation techniques. It does not require complex feedback positioning as electrostatic levitators and can be used with both conducting and insulating materials

unlike the electromagnetic levitators. Because of a relatively simple fabrication and low cost of the levitator it became a very popular containerless technique. It was used for the measurements of thermophysical properties of various materials in the liquid state, e.g. for measurements of electrical conductivity, density, surface tension, viscosity (Enderby et al., 1997, Glorieux et al., 1999, Glorieux et al., 2001, Saboungi et al., 2002), structural characterization by x-ray and neutron scattering (Landron et al., 1982, Ansell et al., 1997, Landron et al., 2001, Hennet et al., 2002, Landron et al., 2003), and glass fabrication (Paradis et al., 1997, Weber et al., 1998.) Feasibility of heating samples of up to 3 mm diameter to the temperatures around 3000K was shown (Saboungi et al., 2002, Glorieux et al., 2001.). Temperatures higher than 2000K were also reported for some samples heated during aircraft parabolic flights in microgravity experiments (Babin et al., 1995.).

Shortcomings and limitations. In spite of a very wide use of the aerodynamic levitation, it has some disadvantages that limit its applications. For example, due to the geometric configuration of the levitator, the sample is usually heated by a laser placed above the nozzle. The gas flow from the nozzle cools down one side of the sample, while the other side is being heated. It results in a nonuniform sample heating, even though some precautions are usually taken to reduce the temperature gradients inside the sample, such as coating the nozzle surface with a reflecting material or use of the second laser placed under the nozzle. Instabilities of the heated and molten sample are significant and could result in the sample loss. These instabilities require use of a feedback loop to adjust the flow rate and maintain the sample stability. The levitating gas flow affects the shape of the molten sample and induces internal flows and sample nonuniformity. Poor access to the levitated sample restricted by the nozzle geometry makes it difficult to use a

high rate quenching technique, such as splat quenching. Thus the highest quench rates can only be achievable due to conductive and convective cooling. To the best of our knowledge, the only splat quenching device used in the aerodynamic levitation relied on gravity (Arai et al., 2002). The heated sample was let to fall freely and be caught between two copper covered aluminum plates placed under the nozzle. Clearly, this technique cannot be used in the zero-g conditions.

2.2.4 Acoustic Levitation

Principles. The physical principle of the acoustic levitation is that there is a force exerted on an object placed inside the acoustic field. The high-frequency ultrasonic field is routinely used for the acoustic levitation. In this case, very fast periodic changes of the forces acting on the object take place. Due to the inertia of the object in the sound field, its periodic displacements are very small during the oscillation period, and a time-averaged force can be considered. This force is called the acoustic radiation pressure. In the linear, acoustic approximation, this force is equal to zero. But if the acoustic field is strong, the nonlinear effects become significant and the acoustic radiation pressure that is not equal to zero is exerted upon the object (King, 1934, Westerwelt, 1951, Awatani, 1955, 1957, Olsen et al., 1958, Gor'kov, 1962). If a sample is placed inside a standing acoustic wave, the distribution of the forces acting on the sample is such that it can be suspended in some equilibrium position. For example, in the plane standing waves this position is in the pressure node, in the absence of the external fields, and for the samples with density much higher than the medium density.
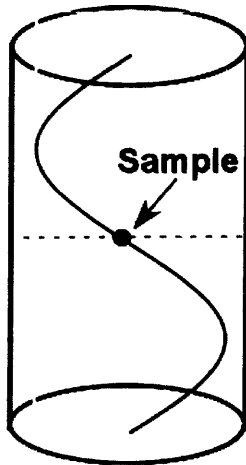
Figure 2.7 Schematic diagram of a cylindrical levitation chamber with a plane wave along the vertical axis.
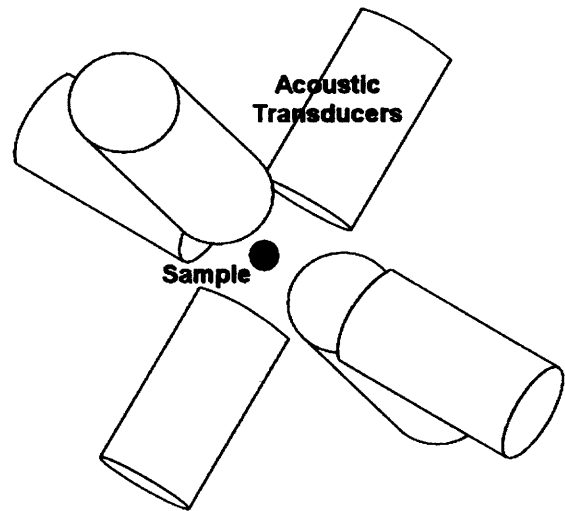
Figure 2.8 Schematic diagram of a triaxial acoustic levitator. Sample is levitated in a pressure node created by the proper tuning of the acoustic transducers.

Several types of levitators that were used for the acoustic levitation are illustrated in Figures. 2.7 – 2.9. Certain acoustic wave modes can be created inside the cavity with the sound generator inserted into the bottom of the chamber at a certain angle. Figure 2.7 represents a cylindrical cavity excited in the normal mode (010) that provides a nodal plane where the sample can be levitated at any location within this plane. This mode is chosen for the illustration purposes; more useful modes can be excited in the cavity to create a nodal point instead of a plane. A triaxial levitator is shown in Figure 2.8, where three orthogonal standing waves are created by three pairs of the acoustic transducers providing a nodal point.

Figure 2.9 shows a uniaxial levitator consisting of an acoustic actuator and a curved reflector. The pressure distributions in the axial and radial direction and forces exerted on the levitated particle are shown (in the absence of external forces). A zero

force is exerted on the particle in the points where the pressure is either at its minimum or maximum. But only in the nodal points (the minimum pressure) the sample equilibrium is stable because there are restoring forces acting on the particle displaced from the equilibrium position. When gravity is present, the sample equilibrium is slightly lower than the nodal point.
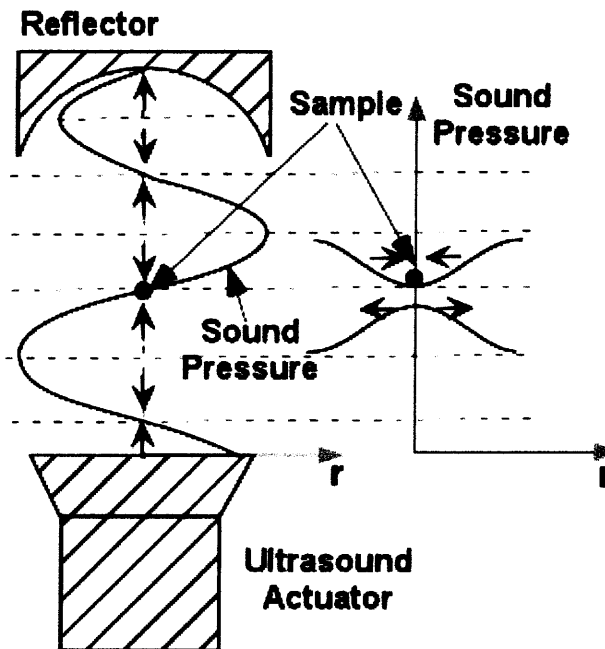
Figure 2.9 Schematic of an acoustic levitator consisting of an ultrasound actuator and a reflector. Pressure distributions are shown between the actuator and reflector and a possible position of a levitated sample. Arrows show directions of the forces acting on the sample in different positions.

Advantages and achievements. Acoustic levitation does not depend on the material type, and in contrast with aerodynamic levitation, allows stable positioning of liquid drops and shells (Trinh, 1985, Trinh and Hsu, 1986). Levitated samples are easily accessible for quenching. The acoustic levitator works with the samples in very wide

ranges of sizes and materials: from small glass beads of 10 μm in diameter (Lee and Feng, 1982) to steel balls of 1cm in diameter (Gammel et al, 1988). Some examples of the acoustic levitation applications are studies of crystal solidification (Trinh, 1985, Gao, 1999), aqueous foam drop dynamics (McDaniel and Holt, 2000), measurements of physical properties of undercooled water (Trinh and Apfel, 1980), the liquid surface tension (Trinh, 1985, Tian et al., 1995).

Shortcomings and limitations. The main problem of the acoustic levitation is that the sample levitation becomes unstable during heating. Samples move out of their equilibrium position and can be easily lost. Although heating of the levitated samples inside a furnace in the 1g condition was achieved (Trinh et al., 1981, Robey and Trinh, 1983, Trinh et al., 1986), some problems remain. First, the maximum temperatures that were achieved in these experiments are rather low, 800 °C. Second, these heating experiments were performed in massive furnaces which require large amounts of energy and a long heating-cooling cycle. The laser spot heating which offers a much faster heating has not been combined with this levitation technique.

2.2.5 Conclusions

The characteristics of the considered containerless techniques are summarized in Table 2.1. The electromagnetic levitation cannot be used with non-conductive oxide materials. Electrostatic levitation is expected to result in unstable sample position at high temperatures, especially taking into account phase transformations expected to occur and change material properties. The feedback system that could alleviate the above mentioned charging of the floated sample and unstable levitation would be extremely complicated. Most importantly, electrostatic levitation was never used at 1 atm pressure.

Therefore, adapting electrostatic levitation was impractical for this research. Whereas aerodynamic levitation is not free from some sample instabilities, especially for molten samples, high temperatures were achieved in many cases. Unfortunately, the high rate, uniform sample heating and rapid splat quenching techniques are hard to implement in this case.

Table 2.1 Comparison of various containerless techniques.

	Electromagnetic	Electrostatic	Aerodynamic	Acoustic
Sample material	Electrically conductive	All	All	All
Feedback Loop	No	Yes	Yes	No
Quencher access	Poor	Good	Poor	Good
Sample Heating Source	Self-heating	External	External	External
Levitation at 1 atm	Yes	No	Yes	Yes
Levitation at high temperature (laser heated)	Possible	Unstable	Unstable	Yes ?

A technique found suitable for our purposes was acoustic levitation. However, one critical issue addressed in this research is whether it is possible to avoid or reduce the levitated sample instabilities while the sample is being heated. Specifically, the stable levitation needs to be established during the laser heating of the sample in microgravity.

The feasibility of acoustic levitation for suspending heated samples is indicated by the previous studies by Lee and Wang (1984), Leung and Wang (1985), Lee and

Wang (1988). According to the earlier results, three main factors may contribute to the sample instabilities in the 1g environment: change of the levitation forces as a result of heating, acoustic streaming, and natural convection. The levitation force can decrease as a result of change in the pressure profile close to the heated sample. At the same time, the acoustic streaming minimizes this destabilizing effect and enhances levitation. Considering these two factors, a conclusion was made that at some optimal rate of heating the stable levitation can be achieved. Natural convection plays the destabilizing role and destroys the optimized acoustic field. Of course, there are some other factors that can cause the sample instabilities such as inhomogeneity of the sample heating or a resonance frequency shift in the acoustic levitator. Our preliminary analysis of different destabilizing factors indicates that the natural convection is the most significant one. Since in zero gravity natural convection does not exist, one can expect that the stable levitation and simultaneous heating of the samples in microgravity could be achieved.

Thus, it is suggested here to combine the acoustic levitation technique with the microgravity conditions for the investigation of phase equilibria in reactive molten materials.

2.3 Selection of a Sample Heating Technique

2.3.1 Furnace

Furnaces allow one to reach high temperatures, uniformly heat and melt different refractory materials, and have been widely used for different kinds of material processing. Unfortunately, furnaces are usually designed for relatively long heating and cooling processes. Therefore, the time necessary for an experiment would exceed by far

the time available in the microgravity experiments, such as onboard the KC135 aircraft.

2.3.2 Xenon Lamp

Xenon lamp is capable of providing sufficient power to heat solid particles to high temperatures and it has been widely used as a heat source. For example, Zr particles of up to 500 μm diameter were formed from the molten foil and ignited by the pulses of light having durations of several milliseconds and energy density of 10 J/cm^2 (Nelson and Richardson, 1964, Nelson, 1965). 1000 W xenon lamps have also been used in the airplane based microgravity experiments with 4×4 mm Mg and Ti (cylindrical) samples heated to the melting during 5-8 s (Branch et al., 1997, Abbud-Madrid. and Branch, 1997). Xenon lamp was also used in the containerless metal melting (Rhim and Ohsaka, 2000). Unfortunately, xenon lamps create problems for optical measurements during the heating. For example, in the work by Nelson (1965) the light scattered from the lamp did not allow photographing the process during the sample heating. Likewise, the temperature measurements by the pyrometer operating at visible light wavelengths could be done only when the lamp was totally blocked (Rhim and Ohsaka, 2000).

2.3.3 Laser

Lasers are unique sources of coherent electromagnetic radiation and offer wide possibilities for material processing and, particularly, for heating. The laser beam can easily be focused and thus, very high energy densities can be achieved and local processing can be accomplished. The lasers also allow one to accomplish processing in a well-controlled time interval. Using an infrared radiation, such as produced by CO_2 lasers, enables imaging of the experiment and optical measurements using visible

wavelengths. These are the reasons that lasers have been widely used in the containerless experiments (e.g., Paradis et al., 1996).

2.3.4 Conclusions

Based on the analysis of the available heating techniques, the laser heating was selected for these experiments. Use of the laser radiation provides experimentalists with a convenient control and delivery of the thermal energy and readily enables synchronization of the heat source and various data acquisition devices.

2.4 Quenching Techniques

Rapid quenching is critical for capturing the phase composition at a high-temperature. As previous combustion experiments showed, the elemental compositions of Zr particles quenched with different methods, and, therefore, different quenching rates, differ significantly (Dreizin, 2000). The radial distributions of oxygen and nitrogen were quite uniform and smooth in the case of 10^6 K/s quenching rate, whereas for the cooling rate of about 10^4 K/s, very large variations in oxygen and nitrogen concentrations inside the particles were observed. Therefore, slow conductive and convective cooling are inappropriate when the information about the high-temperature phases is of interest. Two rapid cooling techniques that potentially could be used in our experiments are briefly considered here. The detailed review can be found elsewhere (Suryanarayana, 1991, Jones, 1999).

2.4.1 Droplet Atomization

In this method a liquid droplet is broken down into fine droplets by means of a high-velocity gas jet. Usually, inert gases are used. The jets form, propel and cool the fine droplets so that their freezing may occur in flight. The method can be combined with the splat quenching technique (see below) so that the droplets impact upon a substrate. The resultant product is in the form of smooth, spherical powder (diameter of particles around 100 μm). The cooling rate depends on the particle size, atomizing gas used, its velocity and pressure. With increasing gas pressure and/or velocity, the finer particles are produced and, as a result, higher quenching rates can be achieved. Typical solidifications rates are of the order of $10^2 - 10^3$ K/s (Suryanarayana, 1991).

The sample could also be atomized in an ultrasonic field. The same acoustic source as used for the levitation can be employed for atomization as well.. The gas pulsations cause the molten sample to break up more efficiently, leading to a higher cooling rate (of the order of 10^5 K/s with 80-100% kHz ultrasound field).

The gas atomization technique is used in production of highly reactive powders. For our applications the quenched samples in the form of powder are less desirable than a bulk sample. In addition, collection of a fine powder in microgravity is difficult.

2.4.2 Splat Quenching

In this technique a liquid droplet freezes by hitting a substrate made of a material with the high thermal conductivity. As a result of collision, a flat flake of quenched material is formed.

Several modifications of this method exist. For example, the sample can freely fall on the substrate by gravity or carried to the substrate by a gas jet. The so-called

'piston-and anvil' technique uses the fixed anvil, and a fast moving piston that is actuated at the proper moment and forces the sample to the anvil. Thus, a sample is thinned between the piston and the anvil. The cooling rate depends on the material of the substrate, anvil thickness, and the velocity of the piston. The quenching rates achievable by this technique are up to 10^6 K/s (Suryanarayana, 1991).

2.4.3 Conclusions

In our research, a technique based on splat quenching is selected, where a molten sample is caught between two colliding copper plates. This is the only quenching technique providing cooling rates that are sufficiently fast to freeze the high-temperature materials without significant phase separation.

CHAPTER 3

EXPERIMENTAL

3.1 Experiment Description

The objective of this experiment is to characterize the high-temperature phase compositions and phase equilibria in molten, ternary systems Zr-O-N at atmospheric pressure. Even though the molten zirconium is very reactive in gaseous oxygen and nitrogen environments, the focus of this research is on the high temperature equilibria rather than the reaction mechanism. Therefore, instead of producing the equilibrium high temperature phases by reacting zirconium with oxygen and nitrogen, as occurs in combustion, the same equilibrium phases will be produced by heating a sample of mixed zirconium oxide and nitride, e.g., materials that are already fully reacted and therefore chemically inert. This approach enables us to conduct experiments in any gaseous environment including air. However, in case of accidental contact of molten sample and interior chamber walls or electrical wiring components or in case of accidental heating of the chamber walls with a reflected focused laser beam (both events are highly unlikely and discussed in detail below), the plastic chamber walls or wire insulation could begin smoldering in air. Therefore, argon was chosen to provide the safest possible environment in the chamber.

A small spherical specimen (1 - 2 mm diameter) of Zr-O-N composition will be positioned inside a processing chamber filled with argon and stabilized in the predetermined position using an acoustic levitation technique. This technique uses ultrasound to produce forces acting on the specimen in both vertical and horizontal

directions. In microgravity, a pulsed CO_2 laser will heat the specimen to about 3000 K, e.g., slightly higher than the melting point of the specimen material. The specimen will be kept at a constant high temperature for about 1-5 s, that is the time necessary to establish the equilibrium. After establishing the high-temperature equilibrium, the specimen will be quenched between two metal plates and recovered for the further phase analysis in a terrestrial laboratory.

The experiments will be controlled using a National Instruments PC-board installed in a laptop computer and a virtual instrument designed in the LabView software environment.

The power of the laser heating the sample will be preset and will not be changed. The sample temperature will be measured by the pyrometer. The laser will be gated by a pulse from the data acquisition board. The maximum gating pulse duration is preset. However, the pulse can be terminated automatically using the feedback loop based on the output of the pyrometer monitoring the heated sample.

All the equipment components, including the diagnostics and control of the experiment, are described in detail below. Because the apparatus was designed for use onboard the aircraft and included a powerful heat source, the CO_2 laser (125 W), a special attention was paid to the experiment safety. Safeguards built in this experimental setup are described below along with the descriptions of the main components of the experimental hardware.

3.2 Equipment Description

The experimental setup includes the following major components:

- a processing chamber;

- an ultrasonic actuator for the sample positioning;

- a laser for the sample heating with a coolant tank;

- quenching mechanism;

- diagnostics and control components;
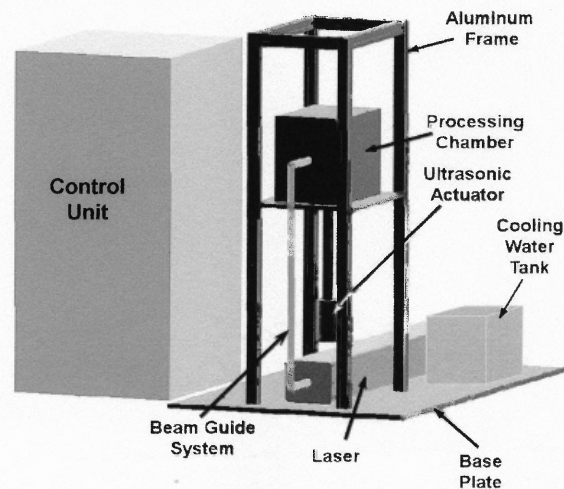
Figure 3.1 Schematic diagram of the experimental setup.

Figure 3.1 shows schematically the major components and their positions relative to one another. An aluminum frame holds the processing chamber. The horn of the ultrasonic actuator is inserted into the chamber through an o-ring sealed feedthrough in the chamber floor. The chamber also houses the reflector used to form a standing acoustic wave and a sample quencher. The heating system consists of a CO_2 laser and a beam guiding system that provides enclosed path for the laser beam from the laser to the specimen positioned inside the chamber. The control unit houses all the necessary power
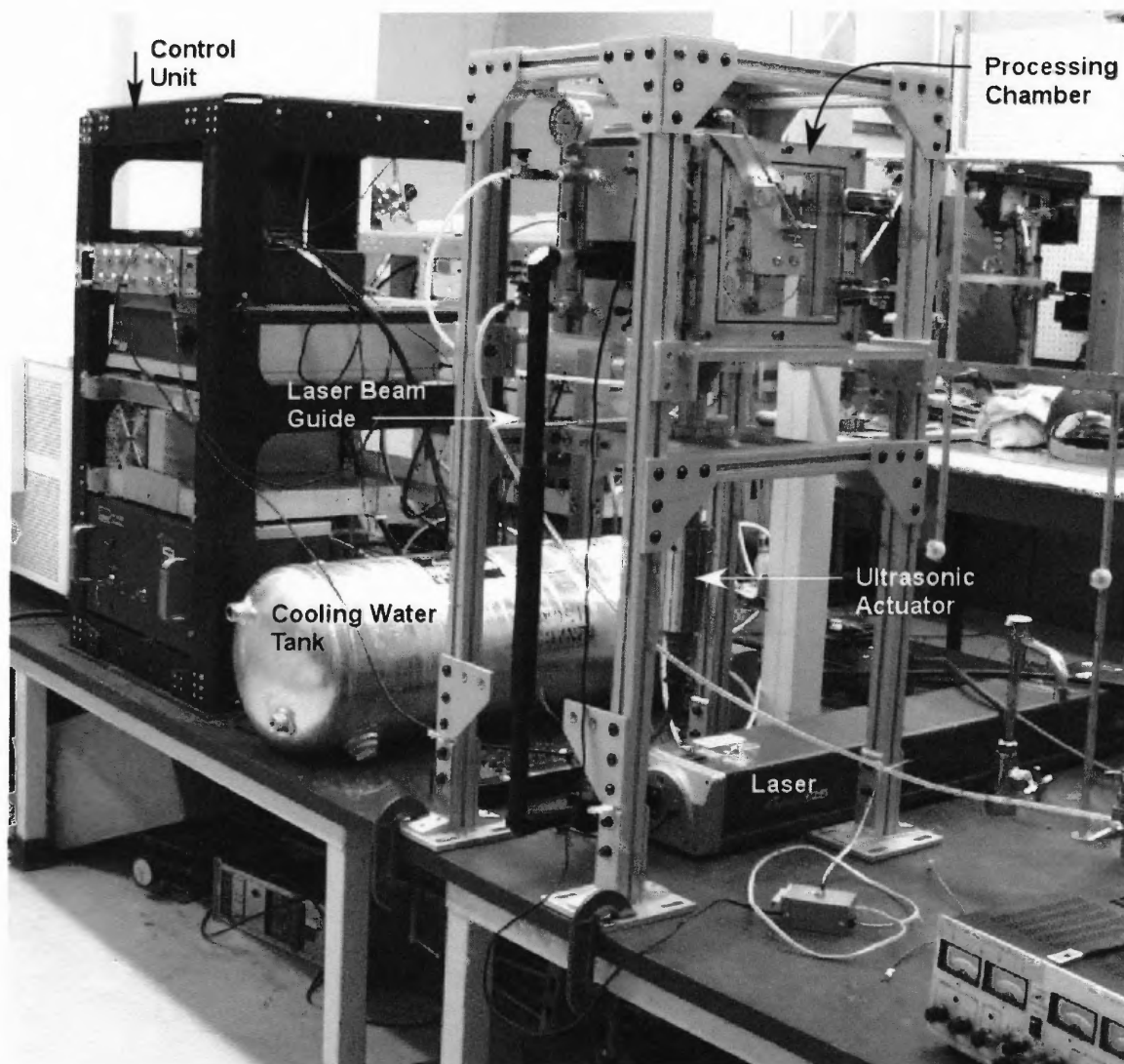
Figure 3.2 Overview of the experimental setup.

supplies, a laser control device, and a computer used to control and monitor the experiment.

Possible component deformations and shifts in the heating setup during the flight could cause the laser beam deflection from the target. As a result, it would be impossible to heat the specimen. To avoid this kind of problem, both the processing chamber setup and the laser system were placed on a single rigid aluminum base plate.

Figure3.2 is a photograph of the setup that was made in the on-ground laboratory.

3.2.1 Processing Chamber

The processing chamber, a cube with 10" sides and with transparent walls, is mounted on a 1/2" thick aluminum plate that serves as the bottom of the chamber. The aluminum plate is attached to four linear bearings mounted in the slots of the main aluminum frame (Figure 3.3). This mounting enables one to adjust the vertical position of the chamber relative to the ultrasonic actuator and laser beam. The chamber has a frame built of 1"×1" solid aluminum bar with the walls attached to the bar sides. One side of the chamber is made of 1/2"-thick aluminum plate and has feedthroughs for the laser beam guiding system, argon, and vacuum lines. This side of the chamber also has electrical feedthroughs. Four other sides of the chamber are made of the transparent, 1/2"-thick Lexan®. The area opposite to the laser beam inlet (behind the mirror mounted in the chamber, see below) is additionally covered with a high-temperature heat absorbing ceramic plate.

Two walls at the opposite sides of the chamber are mounted on hinges and used as doors opening outside. Each door is secured in the locked position with two toggle

clamps. End switches are mounted on each door to prevent laser gating when the doors are open. The chamber is also equipped with pressure relief and vacuum relief valves.
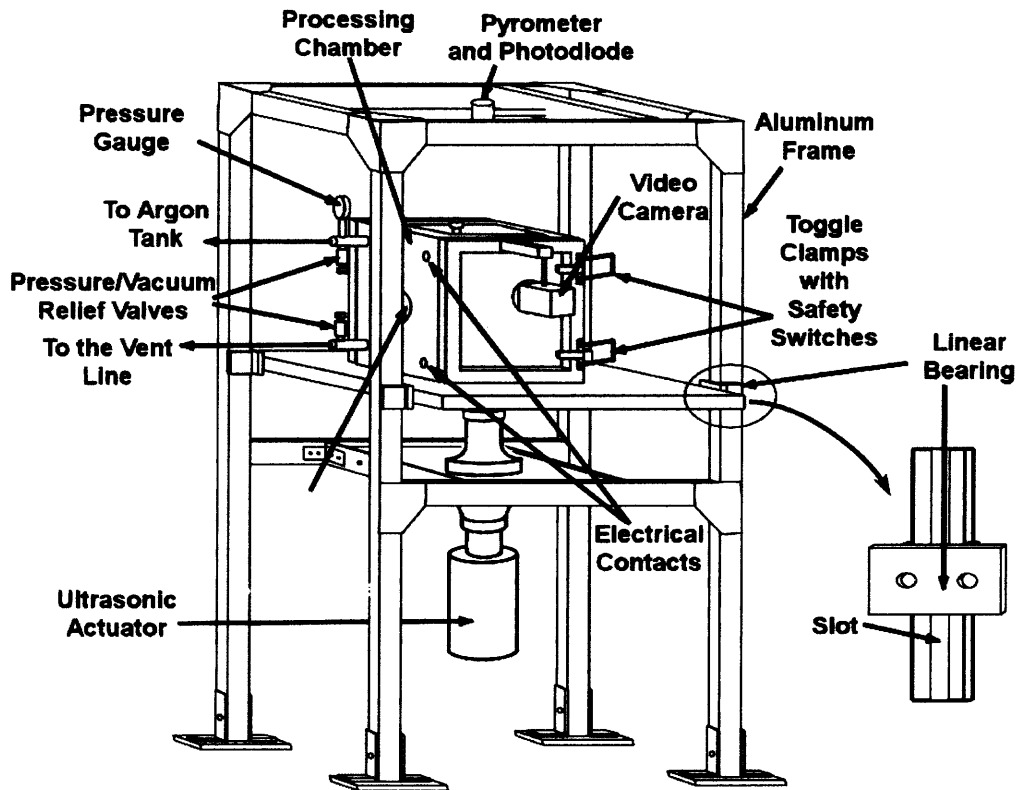
Figure 3.3 Schematic of the processing chamber and its position on the frame.

Special focus was placed on the laser safety. Stray laser light could be produced after the laser beam hit the sample in the chamber. This stray radiation would most likely be diffuse and, since Lexan is opaque to the frequency of the CO_2 laser beam, the radiation would be completely absorbed by the chamber walls. Thus, stray radiation cannot escape and cause any damage or injuries as long as the chamber is closed during the laser operation. In an unlikely case a focused laser beam were reflected by a sample or other component within the chamber, it would still be retained and absorbed by the

chamber walls. To verify this, preliminary tests have been conducted in which a focused laser beam was projected on a block of Lexan. It was observed that the Lexan started melting after an exposure of about 15 s. Note that the Lexan cannot burn while the chamber is filled with an inert gas. The time required to melt a 1/2" thick Lexan wall was estimated (based on experiments) as 1-1.5 min at the maximum laser power setting. As described below, the laser is never gated for a period of time longer than 15 s per experiment, so that the complete melting of a chamber wall could never occur. Thus, even a focused laser beam would not escape its enclosure in the worst imaginable scenario. Because of the small thermal conductivity of Lexan, it is expected that in case of a contact with the molten sample, slow cooling and quenching would occur (the cooling is estimated to last for up to 1 min until the sample is nearly at room temperature). The collision of a molten sample with Lexan is similar to a collision of a droplet of the molten metal produced during welding with the protective welder's screen. The sample does not weld into the Lexan sheet; rather it cools down and can be readily removed after it is cooled. It could bounce off the wall and then hit another chamber wall where similar cooling is expected to occur.

3.2.2 Sample Positioning

Figure 3.4 shows the sample positioning setup with an acoustically levitated sample. The ultrasonic levitator is based on a 20 kHz Branson 910BC welding system. The levitator includes a piezo-electric transducer, a booster amplifying the amplitude of the acoustic oscillations, and an aluminum horn. The horn has a 2" circular vibrating surface and produces a well-focused and directed acoustic wave. A 3" concave circular reflector is placed coaxially to the radiating surface of the horn. A standing acoustic wave is

produced between the radiating surface of the horn and reflector; the sample can be levitated in one of the available pressure nodes. The concave shape of the reflector enhances the levitation producing radial forces directed towards the axis of the horn and reflector. The distance between the radiating plate and reflector is adjustable from 3 to 15 cm.
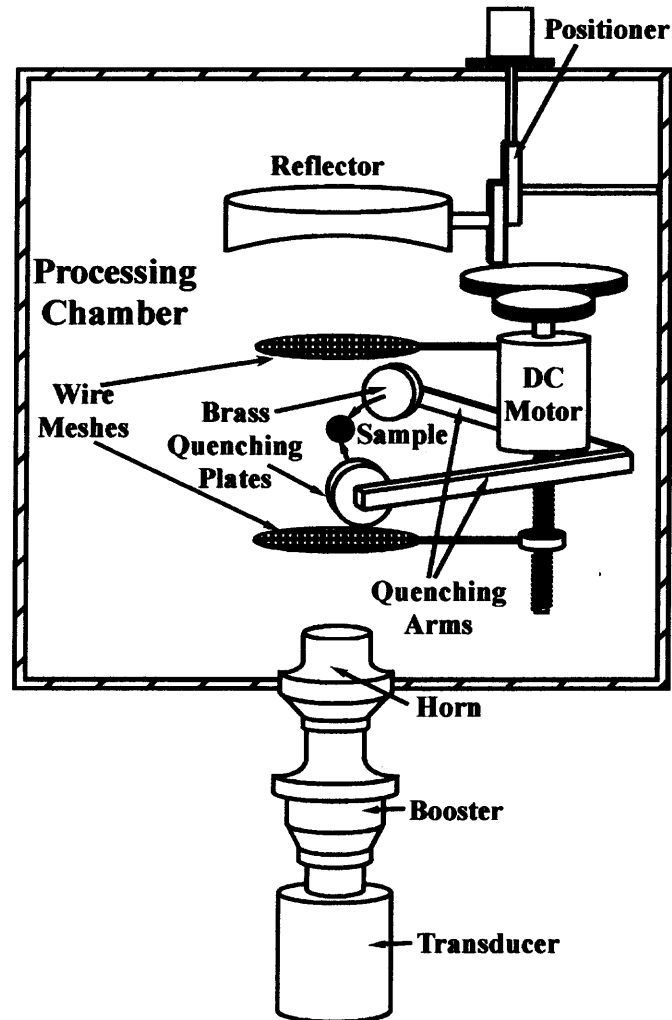
Figure 3.4 Schematic overview of the levitator and quencher.

To insert the sample into the acoustic field, two wire meshes are mounted on linear slides. The meshes are moved up and down by a DC motor controlled from outside of the chamber. Before the experiment, the two wire mesh surfaces are brought together clamping the sample between them. The initial vertical location of the sample is selected to be close to the location of the pressure node targeted for the levitation. While the sample is held by the wire meshes, the acoustic field is turned on. Then, the meshes are slowly moved apart, the sample is released and shifts towards its equilibrium position, where it remains suspended. The meshes also prevent the reflector and radiating plate from potential damage by an accidental contact with the molten sample.

3.2.3 Heating

The sample is heated by a Synrad Evolution–125 CO_2 laser with a maximum power of 125 W. A schematic diagram of the sample heating system is presented in Figure 3.5. The beam guiding system by Laser Mechanisms Inc. encloses the entire beam on its way from the laser output to the chamber input. It consists of extendable tubes that allow one to adjust the height of the chamber relative to the laser, and two beam benders that change the direction of the beam inside the enclosure. The beam guiding system is attached with one flange to the laser diode pointer that is, in its turn, mounted in front of the laser head beam output. The other flange of the beam guiding system is attached to the chamber input. The tube with the ZnSe lens (0.75" diameter, 4″ focal length, by Laser Mechanisms Inc.) is inserted through this flange into the chamber input. This tube has a built-in lens positioner which allows one to move the lens in the horizontal direction and focus the laser beam at a selected location inside the chamber, e.g., before or at the surface of the levitated sample. Both the lens positioner and the lens are

mounted using additional gaskets so that the lens also serves as a sealed window to the processing chamber. The beam is focused just in front of the sample. Part of the beam bypasses the sample and is projected on a gold mirror (1" diameter, 1'' focal length, by Laser Components Inc.) mounted within the chamber on the wall behind the sample. The reflected beam is refocused by the mirror and heats the sample from the opposite side to achieve a more uniform sample heating. The laser beam is aligned with the help of a Diode Laser Pointer by Synrad, which is mounted so that its visible beam path coincides with that of the CO_2 laser beam.
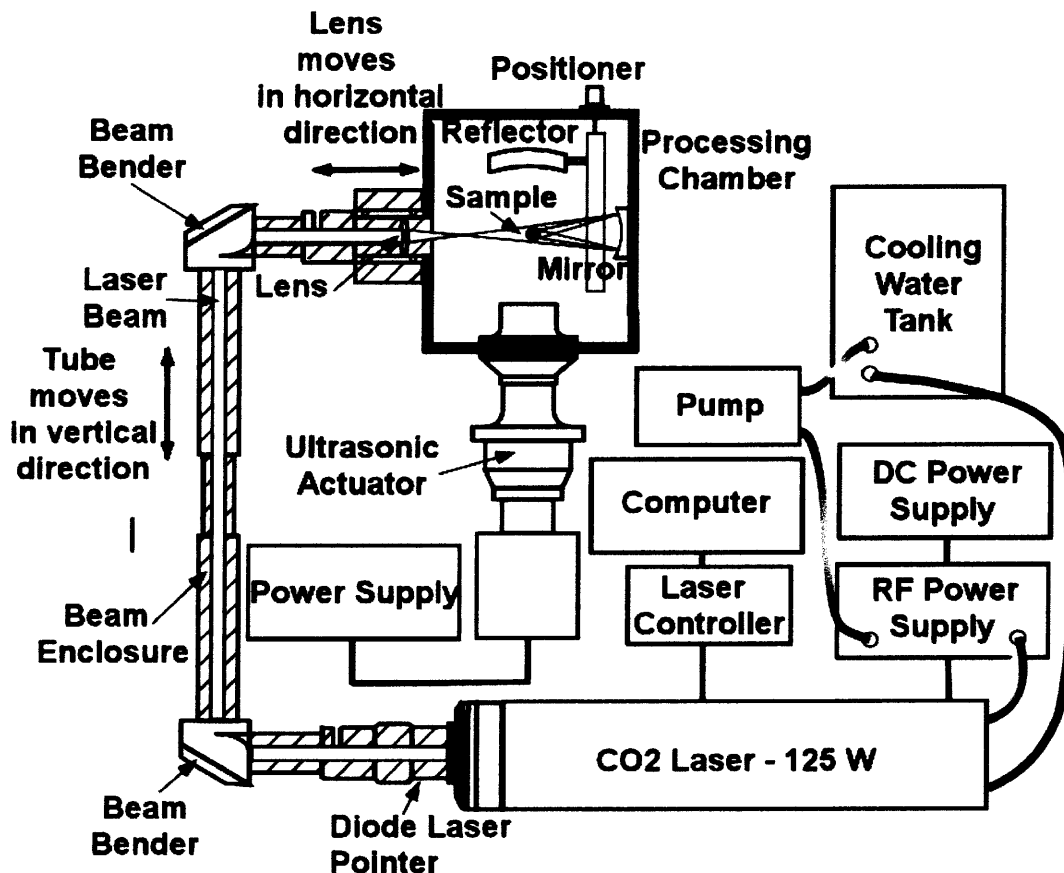
Figure 3.5 Schematic overview of the laser heating setup.

The laser employed to melt the experiment sample requires a source of cooling water. During ground-based operations in the laboratory, cooling water is provided by a self-contained water chiller unit. It is not practical to use this device aboard the aircraft, however, due to operational considerations, and an alternate source of cooling water is provided in the form of a relatively large (15 gal.) reservoir tank. The volume of water contained in the tank is sufficient to provide cooling for the laser when operated using the duty cycle planned for KC-135 operations. The heat removed from the laser during a typical cycle, and the time available between cycles to passively transfer a portion of this heat load from the reservoir to the aircraft cabin ensure that sufficient cooling capacity will be available for the expected period of reduced-gravity operations.
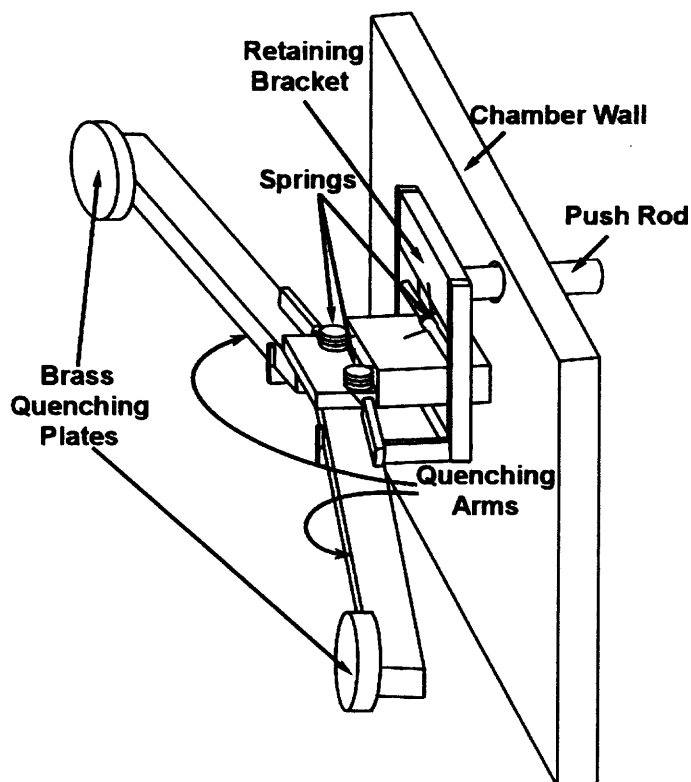
Figure 3.6 A diagram of the sample quencher.

3.2.4 Quenching Mechanism

A schematic diagram of the sample quencher is shown in Figure 3.6. The sample is caught between two colliding brass plates attached to spring-loaded arms. At the beginning of the experiment, the arms are placed apart from each other and held in that position by retaining brackets. The arms' motion towards each other is triggered by releasing the brackets. The brackets are lifted by a linear actuator mounted outside the chamber. A push rod connected to the actuator enters the chamber via a sealed feedthrough. When the plates collide, the sample is splat-quenched between them. The plates' internal surfaces are slightly concave, centering the sample during the quenching. The quenched sample is deformed and solidified as a thin platelet. During the microgravity tests, the samples sandwiched between the quenched plates will be removed from the chamber together with the quenching plates and a new set of plates will be mounted for each experiment. The mounting of the quenching plates to the quenching arms will be made using Velcro for quick plate replacement. The triggering of the quencher is timed using a LabView virtual instrument (VI) simultaneously with switching off the laser.

The quench rate that can be achieved by the splat technique was estimated for a platelet thickness of about 100 µm. The result of an estimate for Zr gives a rate of about 10^6 K/s.

3.2.5 Diagnostics

Diagnostics includes:

- a three-color optical pyrometer to monitor the sample temperature;

- pressure gauges, both absolute and relative to monitor and control the chamber

pressure. Due to the small sample size, the chamber pressure is not expected to change significantly during the sample heating;

- a video camera for monitoring the sample levitation and melting process.

3.3 Control of the Experiment

The duration of a laser pulse and its power are controlled by LabView™ software and a Virtual Instrument (VI) custom designed for this project. The VI uses a National Instrument board DAQ 6062. Figure 3.7 schematically shows the concept of the VI. The gating pulse for the laser is produced by the DAQ board output and sent to the laser controller. A time delay circuit programmed to maintain the sample temperature at a desired level for a pre-set period of 1-5 s establishes the duration of the experiment. The
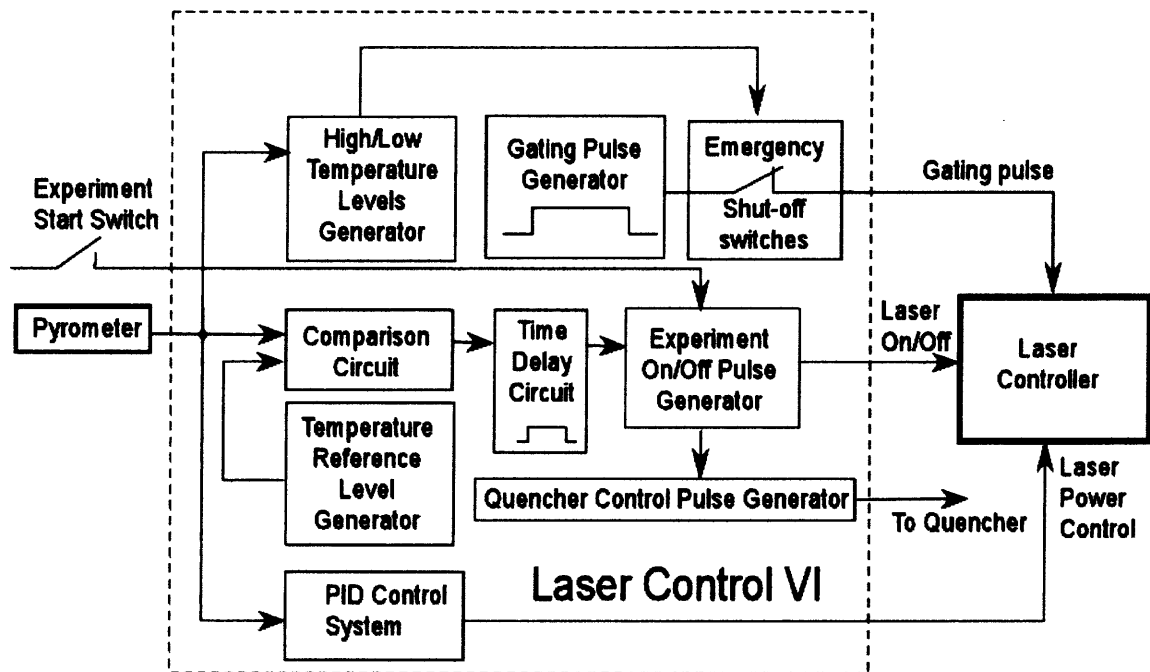
Figure 3.7 Schematic diagram of the VI controlling the laser heating.

time delay circuit is activated when the sample temperature measured by the optical pyrometer reaches a desired reference level. A separate voltage signal produced by the VI controls the laser power. This output (Laser power control) enables a real time change in the laser power during the sample heating. A PID (Proportional-Integral-Derivative) system has been enabled to control laser power based on the feedback from the output of the pyrometer. This system is only effective when the time constant of the sample's temperature response is known. In addition, the feedback signal is sensitive to possible small shifts of the sample position relative to the laser beam. In a situation where the sample position fluctuates, its temperature would therefore also fluctuate, irrespective of changes in the laser power, so that the PID loop could cause oscillations with even large amplitudes. As an alternative to the complicated tuning of the feedback control, a constant laser power can be set. The approximate values of the temperatures achieved at different laser power settings were determined on the ground, prior to the microgravity experiments.

The quencher actuator is also controlled by the Labview VI. Immediately after the laser control pulse is terminated, another pulse is produced that activates the quencher.

3.4 Experiment Safeguards

The apparatus has many safety features which were dictated by the use of the powerful laser and specific requirements for flying onboard the NASA aircraft.

To prevent an accident as a result of the chamber over-pressurization or over-evacuation because of possible experimentalists error or failure of the pressure gages, the

chamber has both pressure and vacuum relief valves. To avoid possible injuries in case the chamber doors are opened when the chamber is under pressure, safety venting valves are installed on both chamber doors so that the doors are blocked when the valves are closed. The experimentalist can open the chamber doors only when the venting valves are open and the chamber is vented to the ambient air.

Whereas the chamber Lexan walls, as was discussed above, protect the experimentalists from exposure to the laser beam, several emergency shutoff switches are built in to prevent possible hazards with the laser beam. These switches are enabled when any chamber door is open or when the output from the pyrometer does not follow the expected temperature history during the experiments. For each experiment, a high and low temperature limits are preset. The pyrometer signal is compared with these limits and the laser shuts down if the low temperature limit is not reached during a predetermined time (e.g., 5 s) after the heating begins, or alternatively, if the sample is overheated. The first event could be indicative of a major beam misalignment, while the second would indicate an unexpected exothermic process (e.g., combustion). In addition to these precautions the laser has many other safety features that are listed in Table 3.1.

The experiment is designed to be powered by an auxiliary power supply provided by NASA. This power supply has the main "kill" switch shutting down the entire apparatus.

Table 3.1 Laser Safety Features.

Feature	Location	Description
UC-2000 Lase On/Off Pushbutton	Laser Controller UC-2000	Toggle the laser On/Off
RF-3000 Switch	Power Supply RF-3000 front panel control	On/Off switch controls power to RF driver electronics.
Keyswitch	Power Supply RF-3000 front panel control	On/Off keyswitch controls power to RF driver electronics. Key can not be removed from switch in the 'On' position
Shutter switch	Laser Head	Activates a shutter that closes the laser aperture. The CLOSED position closes the aperture and the OPEN/REMOTE position opens the shutter or allows the shutter to be remotely operated. Closing the shutter also interrupts power to the laser.
Gate signal On/Off	Computer software	Gate signal is sent to the laser controller and is synchronized with the command signal that the controller sends to the RF power supply. This signal is programmed at 15 sec maximum duration and can be terminated any moment by software.
Coolant Flow Switch	Power Supply RF-3000 circuit element	Interrupts laser operation if the flow rate is less than minimum allowable value.
Temperature Switch	Power Supply RF-3000 circuit element	Interrupts laser operation if the laser operating temperature is out of the allowable range.
RF Cable disconnectio n	Power Supply RF-3000 circuit element	Interrupts laser operation if the RF cable is not connected to the laser head.
Emergency Kill Switch	Control Unit	Terminates the power to the laser controller and, therefore, the command signal to the RF power supply.
DC Input Indicator	Power Supply RF-3000 front panel indicator	Indicates that DC power is available for the RF driver. LED illuminates when DC voltage is applied.
Laser Ready Indicator	Power Supply RF-3000 and Laser Head indicators	Indicates that laser has power applied and is capable of lasing. LED illuminates when the Keyswitch is turned 'On' and Remote terminals are closed..
Lase Indicator	Power Supply RF-3000 and Laser Head indicators	Indicates that laser is actively lasing. Lase LED illuminates when laser beam is active. Higher power output produces brighter illumination

Table 3.1 (Continued)

Lase Indicator	Laser Controller UC-2000	Illuminates Red to indicate the laser is being commanded to lase or the laser is ready to lase in remote control mode.
Five second delay	Power Supply RF-3000 circuit element	Disables RF driver/laser output for five seconds after Keyswitch is turned 'On' with Remote terminals closed. Output remains disabled if remote terminals are open.
Power Fail Lockout	Power Supply RF-3000 circuit element	Disables RF driver/laser output if input power is removed and then reapplied (AC power failure or remote interlock actuation) while the Keyswitch and Remote terminals are still closed. Operator must reset the Keyswitch to restore operation.
Remote Interlock	Power Supply RF-3000 rear panel connection	Disables RF driver/laser output when remote interlock on a chamber door is opened. Operator must close the remote interlock and reset the Keyswitch to restore operation.
Overvoltage protection	Power Supply RF-3000 circuit element	Fault shutdown will occur if the internal supply voltage rises above +36VDC +-1V. Operator must reset the Keyswitch to restore operation.
Reverse voltage protection	Power Supply RF-3000 circuit element	Three power diodes in parallel with DC supply line prevent current from flowing if supply is connected backward (-45 V max.)
Cooling Indicator	Power Supply RF-3000 front panel indicator	Illuminates red when either the coolant temperature or flow rate violates limits.
Warning Labels	Power Supply RF-3000, Laser Head exteriors	Labels attached to various external housing locations to warn personnel of potential hazards.

CHAPTER 4

NORMAL GRAVITY TESTS

4.1 Pressure Profile Mapping

The acoustic field in the levitator must be characterized to adjust the distance between the acoustic radiator and reflector and to select the pressure node that is best suited for sample positioning (i.e., for which the levitation is most stable and resistant to perturbations.) Following earlier work (Whymark, 1975) the acoustic pressure distribution between the radiator and reflector was mapped with a condenser microphone probe. By moving the reflector and changing the distance between the radiator and reflector, pressure and velocity fields were changed as well as the forces acting on the levitated sample. The equilibrium positions of the sample in the absence of gravity would be at the nodal pressure points where the levitation force equals to zero.

Figure 4.1 shows a typical microphone output for one of the resonance conditions attained by adjusting the distance between the radiator and reflector. The deepest pressure minimum occurs at the nodal point closest to the reflector. The pressure gradient in the axial direction is also the strongest in comparison to other nodal points. Therefore, it was expected that the levitation would be most reliable and that the stabilizing axial forces would be greatest at this point. However, the pressure profiles are sensitive to minor adjustment of the reflector position. Every such adjustment affects all the nodes, requiring detailed and labor intensive re-mapping of the pressure distribution. Moreover, the pressure distribution provides only a two-dimensional projection of the three dimensional acoustic field and does not allow one to predict whether a sample
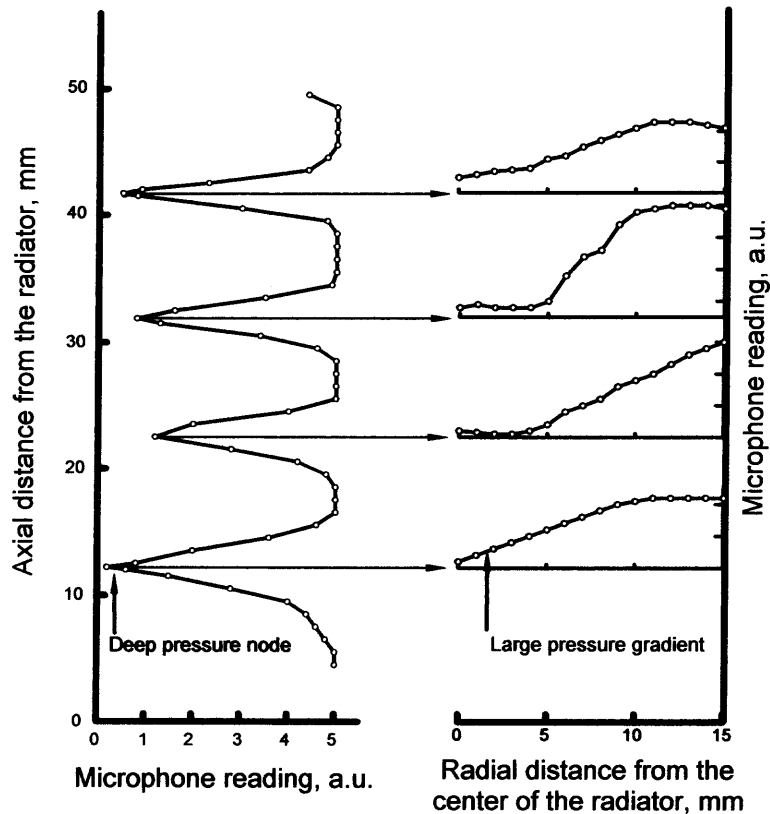
Figure 4.1 Axial and radial pressure distribution of the acoustic field for a fixed radiator-reflector distance.

would oscillate or remain stable in a given node. It also is not a useful guide for the reflector adjustment needed to fine-tune the position of the levitated sample. Therefore, a more comprehensive and efficient approach to characterization of the levitator performance has been developed.

4.2 Characterization of the Levitator Performance

Direct visual observations of the levitation of a sample placed in each of the available nodal points were conducted using a high-speed camera. For each node, the distance between the radiating plate and reflector was adjusted in a wide range and the stability of

the sample position was assessed by measuring the amplitudes of the observed sample oscillations. This way, one series of experiments produced a complete characterization of the levitation quality for one node. The objectives of these observations were to compare the stability of the sample levitation in different nodes for different reflector positions and to choose the node with the most stable particle levitation and an acceptable range in which the sample position could be adjusted by moving the reflector.
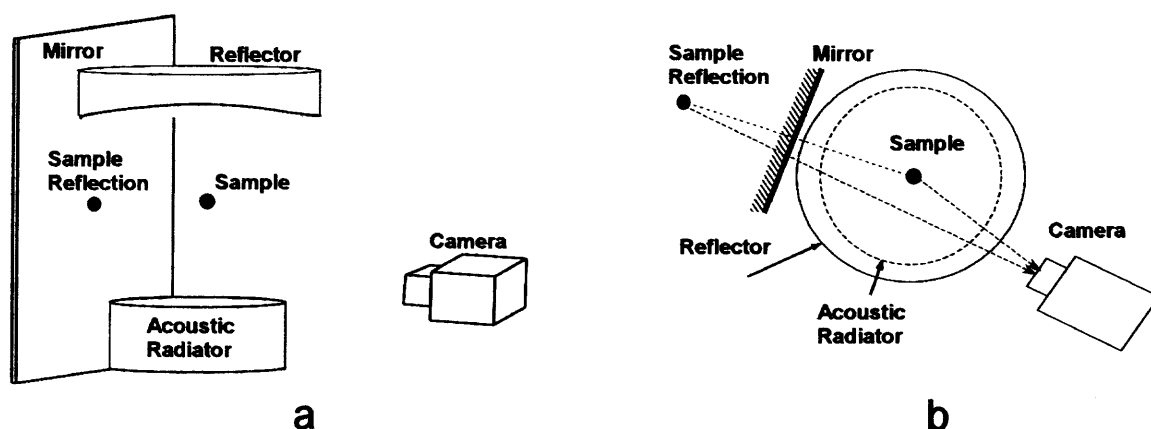
Figure 4.2 A side (a) and a top (b) view of the setup used for filming the sample levitation.

To imitate a sample in microgravity conditions, 3-mm diameter light Styrofoam samples were used. The three spatial coordinates of the center of the spherical sample were reconstructed from a pair of 2D video images. Two synchronized sample images were recorded simultaneously using a high-speed video camera (MotionPro 500) and a mirror placed adjacent to the levitated sample. The geometry of this setup is illustrated in Figure 4.2. At a given radiator-reflector distance, a video sequence of the levitated sample for each pressure node was recorded. This procedure was repeated for different

radiator-reflector distances. The acquired images were processed using Tracker software, the three- dimensional coordinates of the center of the spherical sample were reconstructed and the amplitude of the sample oscillations determined.

Description of different techniques designed to render the 3D coordinates of an object based on images obtained with two cameras can be found elsewhere (Shapiro and Stockman, 2001.). Below we describe briefly the technique used here.

4.2.1 Rendering the 3D Coordinates of the Sample

To reconstruct 3D position of an object, relations linking the 3D coordinates with the 2D coordinates of the corresponding image points must be known. The perspective 'pin-hole' camera model provides such relations. The mapping of three dimensions onto a two-dimensional image plane in this model is done by perspective projection as illustrated in Figure 4.3. The point P is projected to the point p on the image point. The center of projection is at the origin O of the camera frame $X_cY_cZ_c$. The image plane is displaced with a focal distance from O along the Z_c axis, which is also called the optical axis. The intersection of this axis and the image plane is called the principal point. There is a following relation between the image pixel coordinates $x_p y_p$ and coordinates of a point in the camera reference frame:

$$\mathbf{x_p} = \mathbf{M} \mathbf{x_n} \tag{4.1}$$

$$\mathbf{x_p} = \begin{pmatrix} x_p \\ y_p \\ 1 \end{pmatrix} \quad \mathbf{x_n} = \begin{pmatrix} \dfrac{X_c}{Z_c} \\ \dfrac{Y_c}{Z_c} \\ 1 \end{pmatrix} \quad \mathbf{M} = \begin{pmatrix} f_x & 0 & x_o \\ 0 & f_y & y_0 \\ 0 & 0 & 1 \end{pmatrix} \tag{4.2}$$

where f_x, f_y – components of the focal length in pixels (this is different from the focal length shown in Figure 4.3), x_0, y_0 - coordinates of the principal points in $x_p y_p$ frame, and $\mathbf{x_n}$ - the normalized coordinates.

The parameters contained in the matrix $\mathbf{M}$ do not depend on the position and orientation of the camera in space. They are called intrinsic parameters of the camera. It follows from Eq (4.1) that if the intrinsic parameters of the camera are known, the normalized coordinates of a point in the camera reference frame, i.e. the straight line to which this point belongs, can be determined.

It is of practical interest, however, to determine coordinates with respect to some other reference frame. Therefore, the relation between the camera reference frame and the reference frame of interest, world reference frame, must be known. This relation is determined by rotation and translation transformations as shown in Figure 4.4:

$$\mathbf{X_c} = \mathbf{R X_w} + \mathbf{T} \tag{4.3}$$

where $\mathbf{X_c}$ and $\mathbf{X_w}$ are vector-coordinates in camera and world reference frame respectively, $\mathbf{R}$ is rotation matrix, and $\mathbf{T}$ is translation matrix. These matrices are called extrinsic camera parameters. In case of the mirror image the expression (4.3) changes slightly:

$$\mathbf{X_c} = \mathbf{R R' X_w} + \mathbf{T} \tag{4.4}$$

where $\mathbf{R'}$ is the reflection matrix.
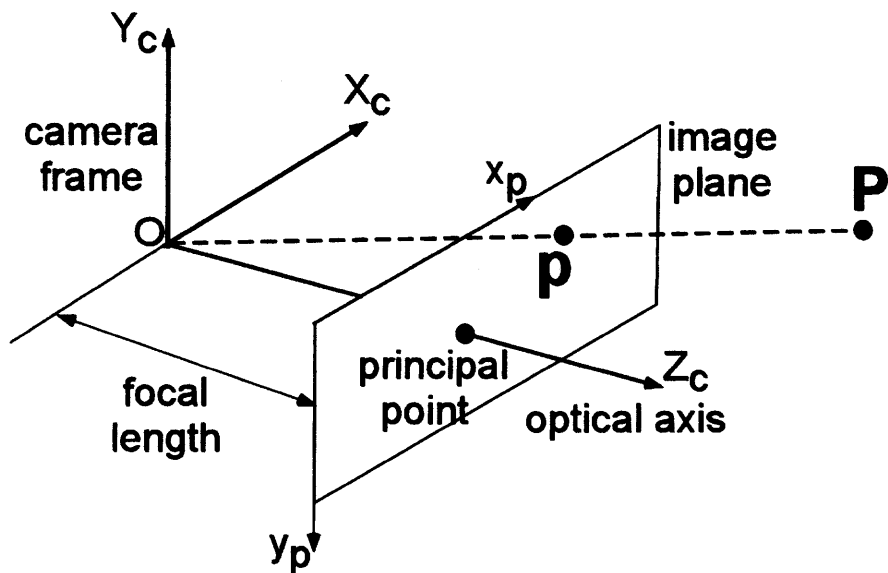
Figure 4.3 The perspective camera model.
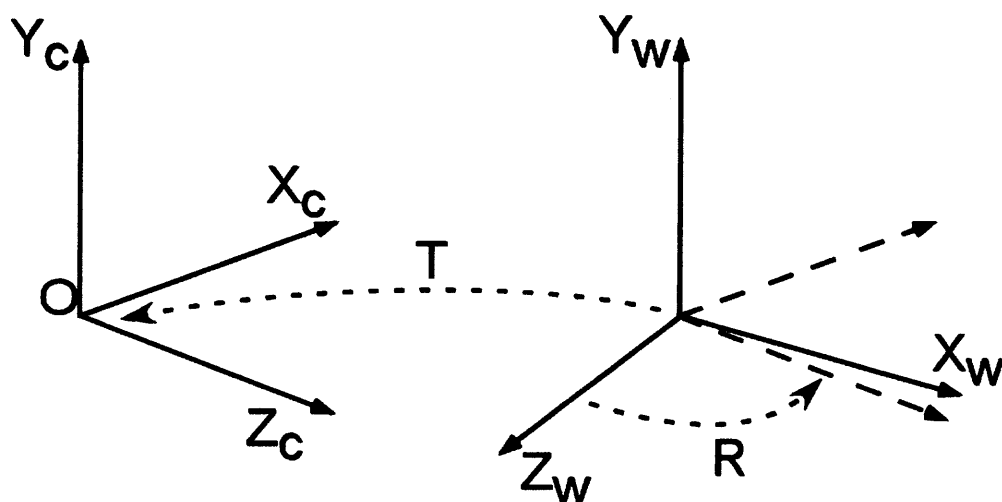
Figure 4.4 Relation between camera and world reference frames.

Therefore, if the intrinsic and extrinsic parameters of the camera are known, the line in 3D to which the point belongs, can be easily found. The second camera (or the mirror image) allows to determine another line in 3D space with this point. The intersection of these two lines gives its coordinates. Therefore, to render three-dimensional coordinates of a point based on stereo images, both the intrinsic and extrinsic parameters of the cameras should be found, i.e., the cameras must be calibrated.

For the simple model described above, the camera can be calibrated using a sufficient number of control points with known coordinates in 3D space. By finding their corresponding image coordinates and using Eq (4.1), the unknown parameters can be determined. When the intrinsic parameters are known, the coordinates of points in the camera reference frame can be found, and hence the position of the camera in the world reference frame can also be found using Eq (4.3).

A more accurate camera model takes into account radial and tangential distortions (Brown, 1966). In this case, instead of Eq (4.2), the following expression is used:

$$\mathbf{x_p} = \mathbf{M}\mathbf{x_d} \qquad (4.5)$$

Here $\mathbf{x_d}$ are distorted coordinates that are expressed, in general, by polynomial expressions using normalized coordinates and intrinsic parameters of the camera. In this case the problem of camera calibration, i.e., finding the camera parameters, as well as the problem of rendering the 3D coordinates become nonlinear. Iterative procedures have been developed and can be used in this case (Heikkilä and Silven, 1997, Heikkilä, 2000).
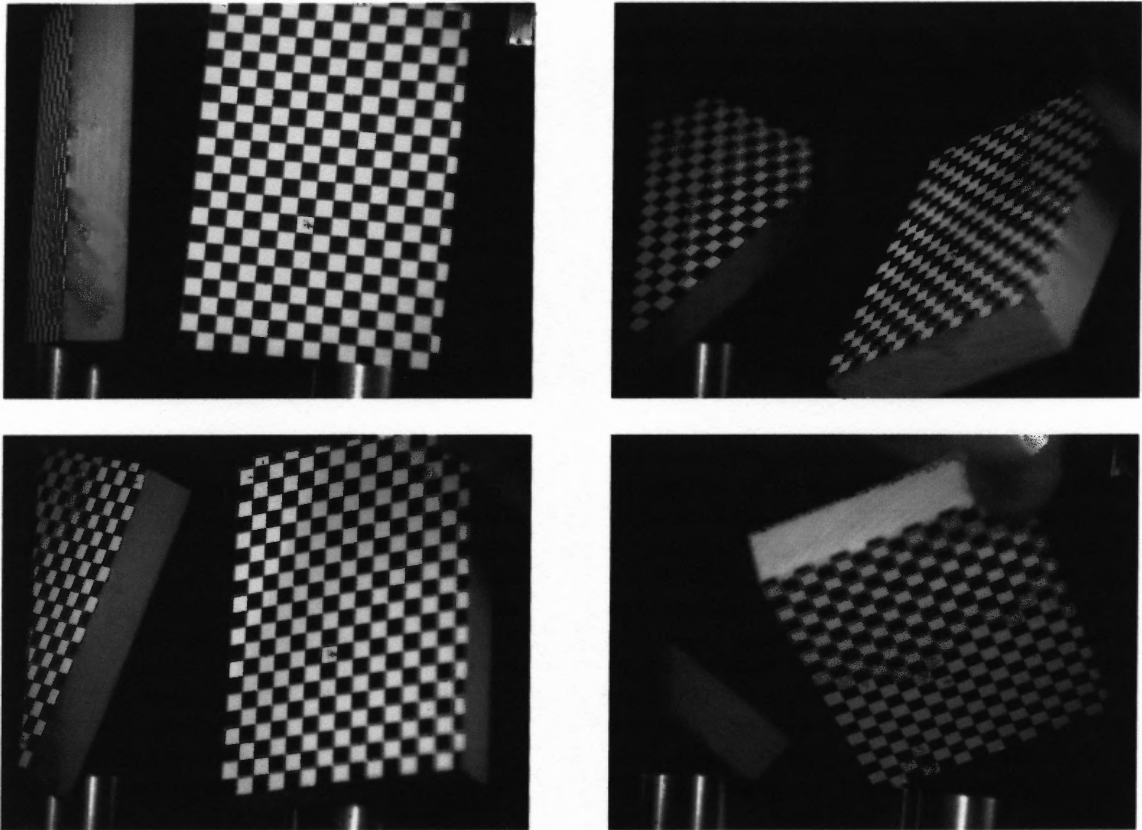
Figure 4.5 Chessboard pattern used for the camera calibration.

The camera calibration Matlab® toolbox by J.-V. Bouguet, 2000, was used in this work for the camera calibration. Chessboard patterns with 5x5 mm squares were prepared and used. 30 images of these patterns were taken under different angles and orientations relative to the camera. Figure 4.5 shows some of the examples for such images. The images were processed by the toolbox software and the intrinsic parameters of the camera presented in Figure 4.6 were obtained. Usually, when two cameras are used, both cameras must be calibrated. Since only one camera was used in this work (and a mirror was used instead of the second camera), the camera calibration procedure described above was performed just once. The world coordinates were attached to the

location of the chessboard pattern that was used for the camera calibration and placed at the center of the levitator. The same software used for the camera calibration allows us to find the extrinsic parameters of the camera.
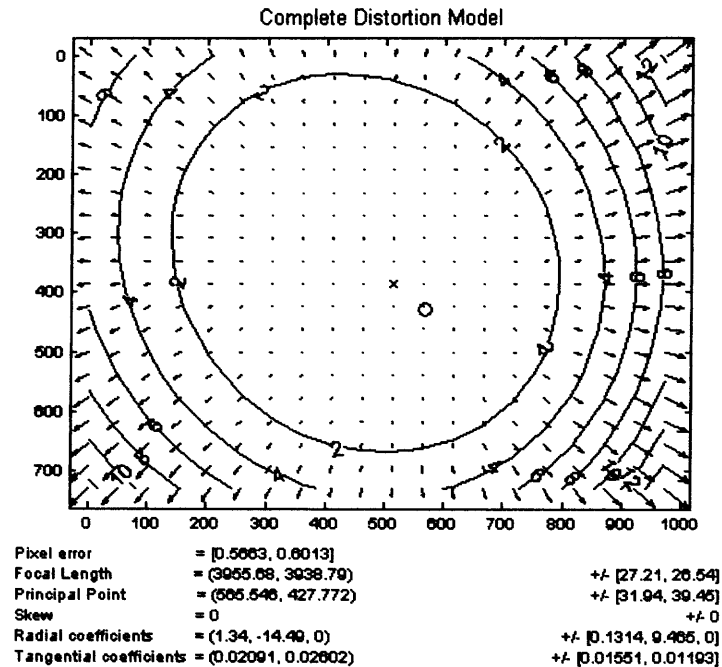
Figure 4.6 Distortion model of the camera.

After the camera was calibrated and the sample levitation was filmed, the obtained images were processed with the Tracker software. Positions of the center of the spherical sample were found on two images for each frame. The normal (undistorted) coordinates of the sample for each camera were found by the method described by Heikkilä, 2000. These coordinates define the straight lines in the 3D world reference frame to which the sample coordinates belong. The intersection of these two lines found

from the real and mirror reflected images, respectively, determines the 3D sample position.

4.2.2 Results

The analysis focused only on the useful range of the radiator-reflector distances (about 4.7 cm) and on the nodes removed sufficiently far from both the radiating plate and reflector to enable heating and quenching of the levitated sample without interference with the levitator components. Figure 4.7 shows the reflector positions and the locations and ranges of axial oscillations for samples levitated in different nodes. The levitation forces are the strongest when the distance between the radiating plate and reflector corresponds to a resonance condition (i.e., an integer number of half-wavelengths). When the reflector is moved away from the radiator, as illustrated in Figure 4-7, the nodes weaken, disappear, and then become reconstructed again when the next resonance position is approached. As expected, large oscillations occur far from the resonance conditions, in the area marked as "node reconstruction" in Figure 4.7. At the radiator-reflector distances approaching the resonance conditions (cf. "resonance" areas in Figure 4.7), noticeable instabilities in the sample oscillations developed even when minor adjustments in the sample position were attempted. In addition, the Styrofoam samples were deformed and sometimes destroyed by strong acoustic forces while levitating in a resonance node. A similar effect was expected for molten samples. The combination of the stable levitation, reasonable range of position adjustment, and no deformation were observed for the samples suspended using a slightly detuned levitator. This condition was selected for the microgravity experiments. Figure 4.8 shows how the sample positions and oscillation amplitudes in both vertical and radial directions evolved when

the reflector position was changed. Results for four different reflector positions are presented. The plot on the left-hand side of Figure 4.8 corresponds to a resonance condition. The sample oscillates around the radiator-reflector axis, except in the nodes close to the radiator and the reflector. When the reflector is slightly lifted, effectively detuning the levitator, the sample's position shifts away from the axis and oscillations increase. For the specific setup developed in this project, it was found that an adjustment of the sample position and a relatively stable levitation were possible for the pressure node located approximately 38 mm above the radiator (as shown in Figure 4.7.) This node was selected to be used in the microgravity experiments discussed below.
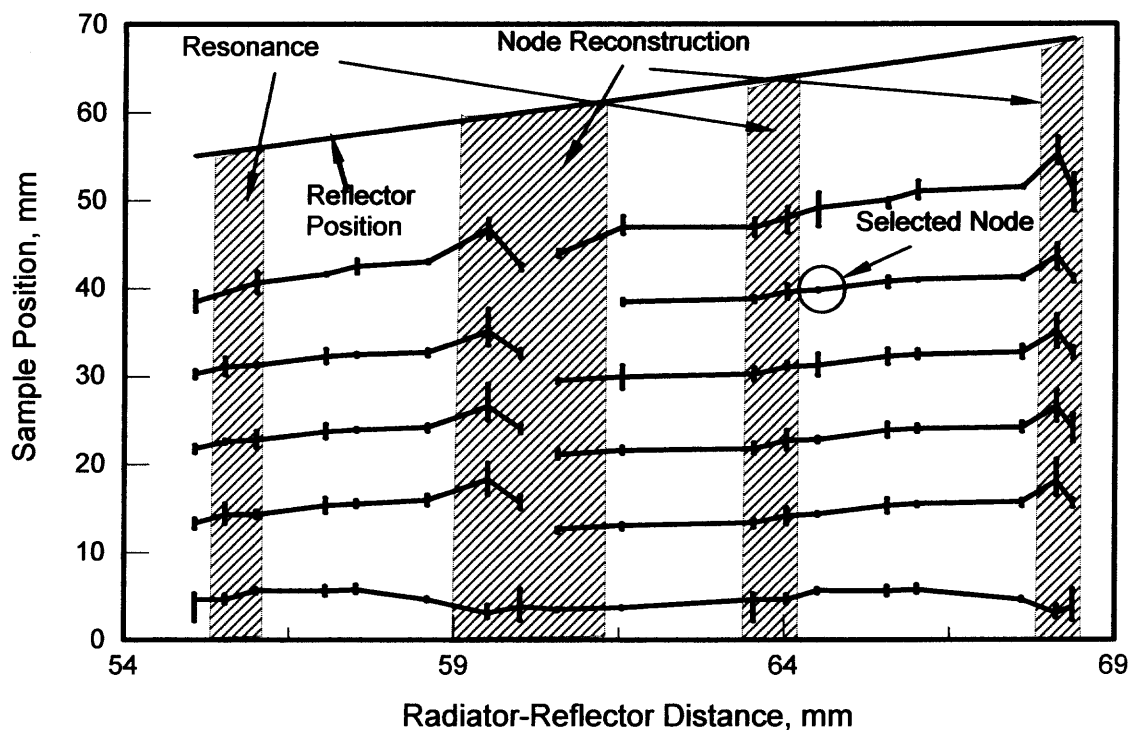
Figure 4.7 Axial node positions and oscillations as a function of radiator-reflector distance
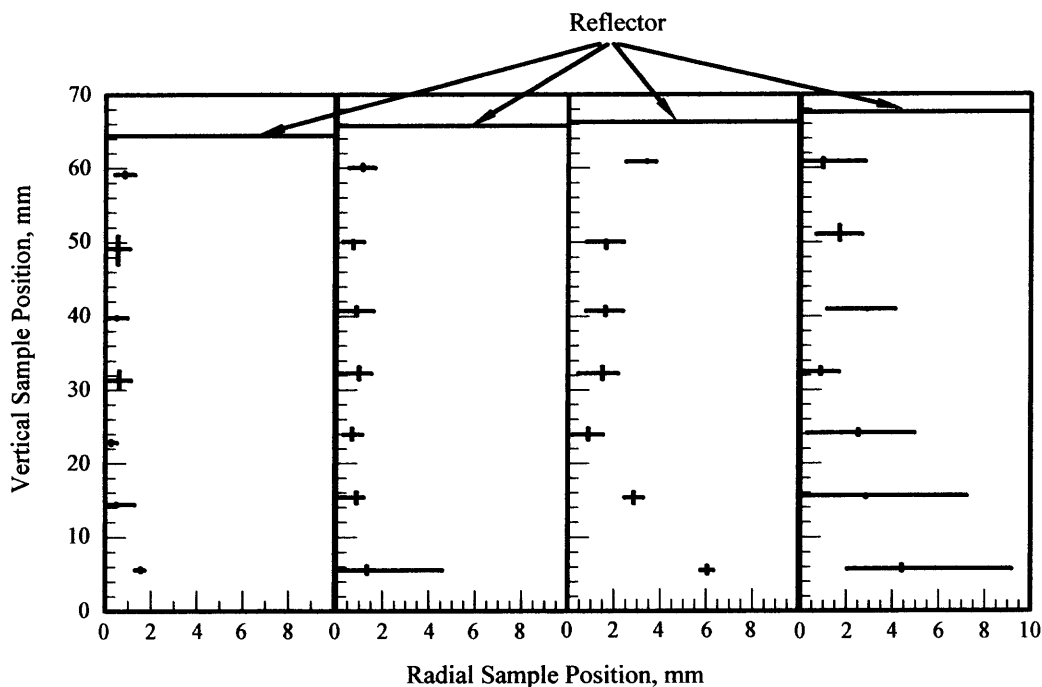
Figure 4.8 Axial sample positions and axial and radial sample oscillations as a function of radiator-reflector distance. The levitator is increasingly detuned in the plots from left to right

4.3 Sample Heating

The time required for the sample heating was estimated for spherical zirconium oxide samples assuming uniform temperature distribution in the sample, radiative and conductive heat transfer, and constant thermophysical parameters for solid and molten samples. The estimate uses a heat balance equation:

$$c\rho V \, dT/dt = Q - \varepsilon\sigma S\left(T^4 - T_0^4\right) - hS\left(T - T_0\right), \qquad T \neq T_m, \qquad (4.6)$$

where c is the sample specific heat, ρ is its density, V is the volume, t is time, T the sample temperature, Q is the laser power, T_0 the temperature of the environment and the initial temperature of the sample (room temperature, 298 K), T_m – the melting temperature, σ is the Stephan-Boltzmann constant, h is the heat transfer coefficient, ε is

the emissivity and S is the surface area of the sample. The heat transfer coefficient h is expressed through the Nusselt number Nu, the thermal conductivity of the atmosphere λ_g, and the sample diameter d:

$$h = Nu\lambda_g / d .\qquad(4.7)$$

The Nusselt number was set equal to 2, corresponding to a spherical particle in a stagnant medium. The sample was considered to be a black body with emissivity $\varepsilon=1$, i.e., maximum possible radiation heat losses to the environment were assumed.

Table 4.1 Parameters used to estimate the temperature of a spherical ZrO_2 sample vs.heating time. References are given where appropriate.

Melting temperature	$T_m = 2950$ K	(Chase Jr., 1988)
Enthalpy of melting	$\Delta H_{melt} = 706257$ J/kg	(Chase Jr., 1988)
Solid heat capacity	$c = 581$ J/(kg·K)	(Chase Jr., 1988)
Melt heat capacity	$c = 713$ J/(kg·K)	(Chase Jr., 1988)
Sample density	$\rho = 5600$ kg/m^3	(CRC Handbook)
Thermal conductivity of argon	$\lambda_g = 0.06$ W/(m·K)	(K.C. Touloukyan et al., 1970)
Laser power (100%)	$Q = 125$ W	
Emissivity	$\varepsilon = 1$	

Other parameters used in the estimates are shown in Table 4.1. Results of the estimates are shown in Figure 4.9; plateaus in the heating curves indicate the melting of the sample. According to these calculations, the largest sample that can be heated and melted within the available time of ~ 5 s is close to 3 mm in diameter. This sample size is completely adequate for subsequent analyses by SEM, TEM, and XRD.

Experiments with zirconia sample heating were also conducted. Because of difficulties of simultaneous levitation and heating a sample at normal gravity, in these
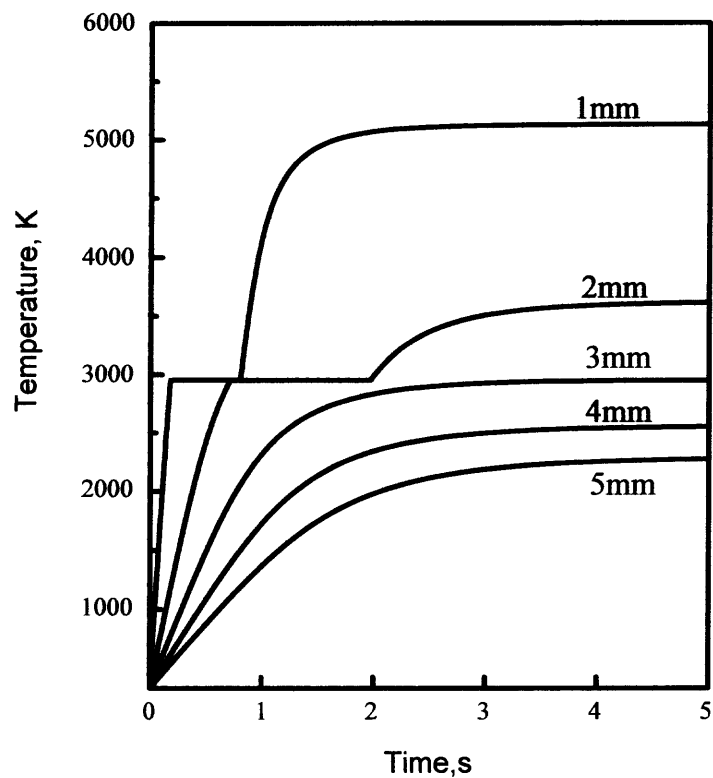
Figure 4.9 Calculated sample temperature for samples of ZrO_2 with varying diameters heated with a 125 W CO_2 laser.
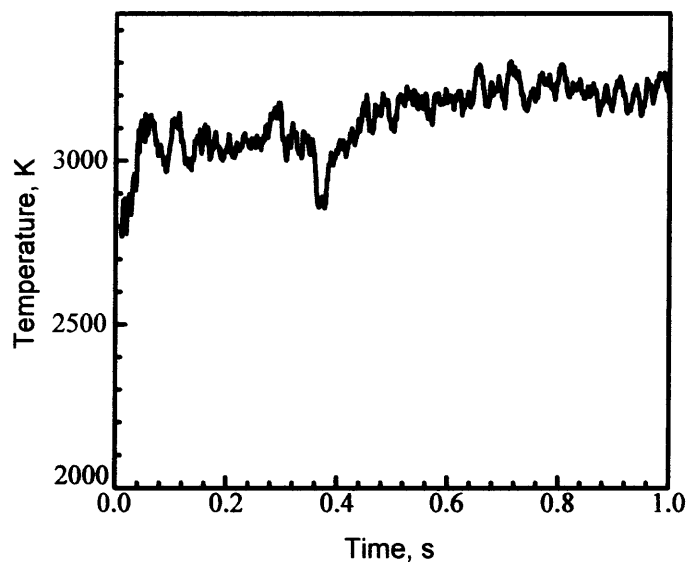
Figure 4.10 Experimental sample temperature recorded for a 2 mm spherical ZrO_2 sample heated with a CO_2 laser with 50 W power.

experiments a spherical particle about 2 mm diameter was attached to the end of a tungsten wire rigidly mounted in the chamber. The sample was laser heated with a constant power and the temperature was monitored using a three-color pyrometer. A typical curve obtained in these experiments and shown in Figure 4.10 represents heating with 40% of the maximum laser power. The sample was heated to a steady temperature of about 3200 K in less than 1 second. This time is shorter than the theoretically estimated time shown in Figure 4.9. One reason for this discrepancy can be that the emissivity was assumed to be equal to 1 in our estimations, thus, the highest radiative losses were considered in the estimate. Because radiative heat losses at high temperatures are very significant, the theoretical results depend strongly on the value of emissivity.

The time while the sample was kept at a high temperature should be sufficiently long to reach thermal equilibrium throughout its volume. This time can be roughly estimated from the species diffusion rates and assuming that the equilibrium is established after the components diffuse over a distance equal to the sample diameter. Using the diffusivity coefficient of oxygen in zirconium, $D = 2.63\exp(-118/RT)$ cm^2/s (with R as the universal gas constant) (P. Kofstad, 1988), the estimated equilibration time t_{eq}

$$t_{eq} \approx \frac{d^2}{D} \tag{4.8}$$

is of the order of one second for a particle of 1 mm diameter at 2500 K. This diffusion coefficient is lower than that in a molten metal. Therefore, this estimate can be considered as the upper limit for the equilibration time.

These estimates and experiments on the sample heating confirmed the feasibility of the microgravity experiment in which a sample would melt and be heated to about 3000 K within the short time available during a single parabolic trajectory of the aircraft.

CHAPTER 5

MICROGRAVITY EXPERIMENTS

5.1 Experimental

Experiments in microgravity were conducted onboard a NASA KC-135 airplane flown off the NASA Johnson Space Center in Houston, TX. Spherical samples of 2 mm diameter were prepared as a mixture of Zr, ZrO_2, and ZrN. To prepare samples, the component powders were mixed for 10 minutes using a SPEX 8000 shaker mill with zirconia milling vials and balls. Sample pellets were pressed in a 2 mm die. The pellets were ground inside a small cylindrical bottle with walls lined with sand paper and a tangentially entering air flow (Figure 5.1). The grinding produced samples with nearly spherical shapes suitable for levitation (Figure 5.2). Samples with the following compositions (at-%) were prepared: $(ZrO_2)_{80}(ZrN)_{10}Zr_{10}$, $(ZrO_2)_{45}(ZrN)_{45}Zr_{10}$, and $(ZrO_2)_{10}(ZrN)_{80}Zr_{10}$.
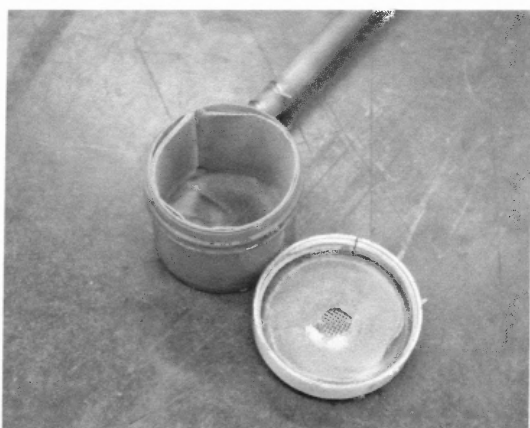
Figure 5.1 A bottle with walls lined with sand paper used to grind the samples to spherical shape.
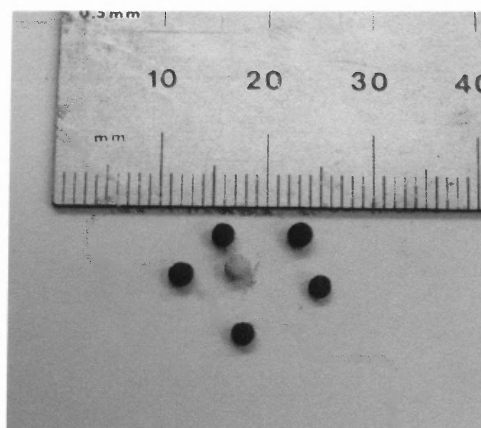
Figure 5.2 Spherical samples with different initial compositions used in the microgravity experiments.

The same setup that was tested in gravity tests was used in microgravity experiments. The possible deformations in the setup during the flight could cause the laser beam deflection from the target. As a result, it would be impossible to heat the specimen. To avoid this kind of problem, both the processing chamber setup and the laser system were mounted on a single rigid aluminum base plate which was attached to the aircraft floor. Before each parabolic trajectory of the KC-135 aircraft, a sample was clamped between the wire meshes brought together at the position close to the pressure node pre-selected to levitate the sample. As described above, this position was determined from the on-ground experiments with Styrofoam samples, and the CO_2 laser beam was adjusted to heat the sample at this specific location. It was expected that in microgravity, the actual sample position would be slightly shifted up compared to that observed in normal gravity. Thus, minor adjustments of the sample levitation position were expected to be necessary in microgravity to place the sample exactly in the path of the laser beam. As described above, the adjustments of the reflector position allowed one to move the levitating sample up and down within the sealed chamber. The wire mesh screens that were moved apart to release the sample also slightly affected the sample positioning. Therefore, in addition to the variable distance between the radiator and reflector, the distance to which the screens were moved apart was used to adjust the levitation location and stability. During each parabolic trajectory of the aircraft, the screens were first moved apart so that the sample was released and levitated in the vicinity of its intended position. Then, fine adjustments of the positions of the reflector and wire mesh screens were used to stabilize the sample at the location where it was illuminated by the visible diode laser beam aligned with the CO_2 laser. After the sample

was positioned, laser heating and quenching sequence controlled by the LabView VI was initiated.

The sample position before and during the laser heating was recorded using a video camera. The temperature of the sample was measured by the pyrometer and recorded using a computer-based data acquisition system.

5.2 Results and Discussion

From each video frame, both vertical and horizontal positions of the sample and the intensity of emission produced by the heated sample surface were determined. Whereas the sample surface heated to 800 – 1000 K produced sufficient radiation to be registered from the video signal, only samples heated to temperatures exceeding 1500 K produced radiation intensity sufficient to be measured by the three-wavelength pyrometer. At the same time, when samples were heated above 1500 K, the video image became saturated and the sample position could not be well tracked. Figures. 5.3 and 5.4 illustrate typical results obtained from the processed video images and pyrometer traces.

Figure 5.3 presents the sample coordinates and radiation intensity obtained from the processing of a video sequence captured during the levitation and heating. Vertical lines show the moments when the CO_2 laser beam was turned on and off. Before the laser is turned on, sample oscillations are observed in both horizontal and vertical directions. The amplitude of the vertical oscillations is negligible, however. The sample is observed to shift in the vertical direction before the laser pulse was triggered. This shift was caused by and correlated with the motion of the wire mesh screens moving

apart into their final position. As described above, this motion of the screens was used to better align the sample position with the laser beam path.
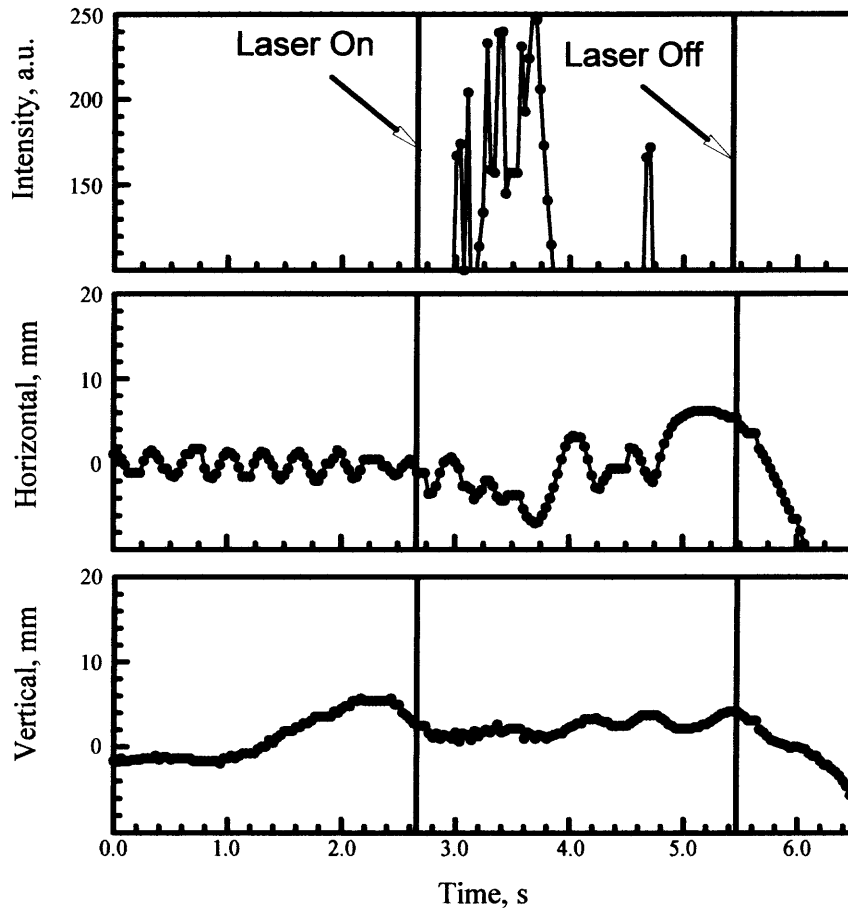
Figure 5.3 Intensity of the video images and sample position during levitation and heating in microgravity.

When the laser is turned on, amplitudes of both horizontal and vertical oscillations increase. However, the sample's vertical location is held rather well indicating the effectiveness of the acoustic levitation combined with the laser sample heating. At the same time, the amplitude of horizontal oscillations becomes very large.

This causes ineffective heating of the sample as it moves in and out of the laser beam. Eventually, the horizontal oscillations remove the sample from its stable position and it escapes before being caught by the quencher plates.

The amplitude of the observed horizontal oscillations of the levitated sample even before the sample was heated was much greater than that observed in preliminary normal gravity experiments. There were no differences in the setup design and mounting in microgravity and normal gravity experiments. To understand the possible effect of the aircraft vibration and residual accelerations that take place during the parabolic trajectories, some experiments were conducted where the sample was levitated before the microgravity, and then during microgravity conditions the levitator was turned off. The sample slowly drifted out of the laser beam area without any oscillations or sudden change of direction. These experiments indicate that aircraft vibration or residual accelerations are not the cause of the horizontal oscillations of the sample. It is understood that the stronger horizontal oscillations are produced because in microgravity the sample levitates exactly in the pressure node while in normal gravity, the sample levitates below the pressure node. Therefore, the asymmetry of the acoustic field produced by the reflector's concave shape is more effective in stabilizing the sample horizontally in normal gravity than it is in microgravity. This effect was generally anticipated, however, its significance was not documented in the literature and was therefore unclear. These experiments showed that while being significant, the horizontal sample oscillations do not remove the sample from its stable position until the laser heating is turned on. However, when the sample is heated, the increased amplitude of horizontal oscillations becomes detrimental for its consistent positioning.
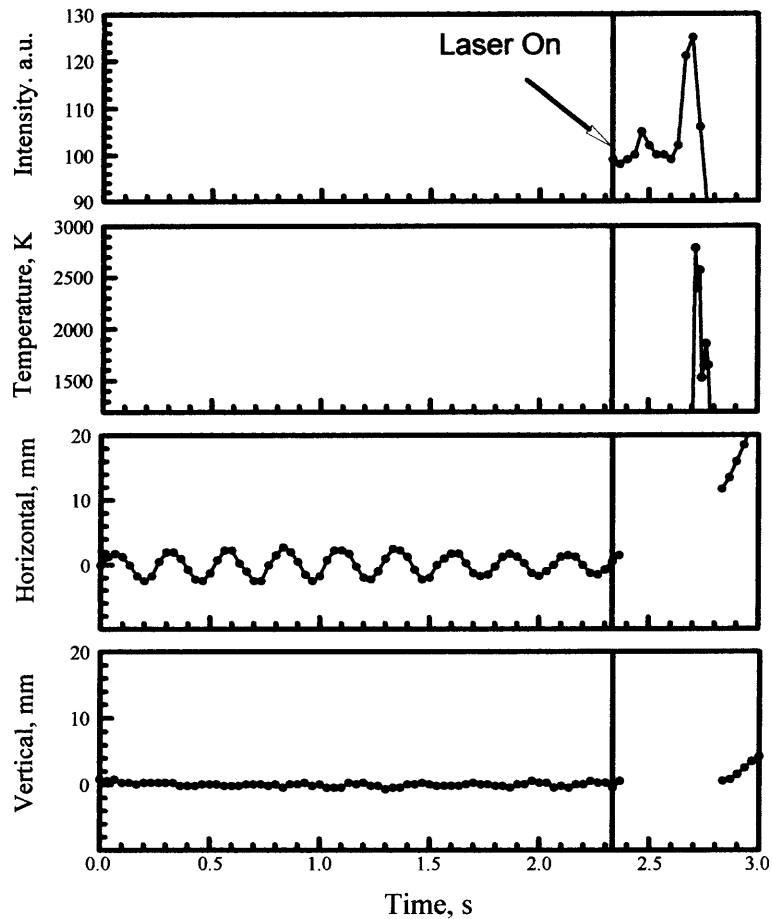
Figure 5.4 Temperature, intensity of the video images and sample position during levitation and heating in microgravity.

For the experiment illustrated in Figure 5.3, the pyrometric temperature measurements are not available because the temperature did not exceed 1500 K. Figure 5.4 illustrates another microgravity experiment in which the sample was heated to a higher temperature. Similar to example shown in Figure 5.3, before heating the sample moves in the horizontal direction with the oscillation amplitude of about 2 mm. The vertical position of the sample is very stable. After the laser was turned on, the sample is rapidly heated to a very high temperature, and the video image becomes saturated. The

sample position could not be tracked for about 0.5 s, and the pyrometer signal indicates the sample heating to about 2800 K. However, similar to the experiment illustrated in Figure 5.3, the sample eventually escapes the levitation region before being caught by the quencher plates. The cooling of the sample that moved out of the laser beam is rapid as implied by both the pyrometer and the video signal intensity. When the sample position can be tracked again, one observes that the vertical coordinate of the sample essentially did not change during the heating. Therefore, the efficiency of the acoustic levitator in microgravity is very high even when the sample it heated in excess of 2000 K. At the same time, the horizontal sample position indicates an increased oscillation amplitude that was the most likely reason of the sample's escape.
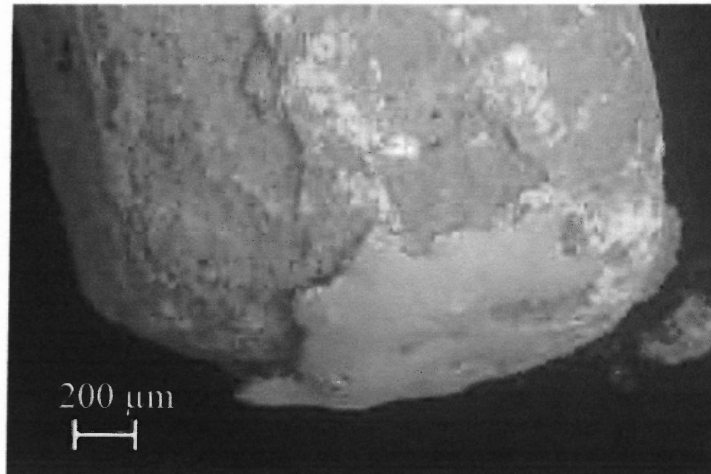
Figure 5.5 SEM image of a sample levitated and heated in microgravity

Figure 5.5 presents a scanning electron microscope (SEM) image of the sample heated in microgravity and recovered from the processing chamber. A number of similar samples have been collected, however, no samples were successfully splat-quenched because of the horizontal sample instabilities described above. The image in Figure 5.5

shows that the sample was heated nonuniformly and only local melting was achieved. A spot of about 0.8 mm diameter and 30 μm thickness was melted. Based on the observed stable vertical position of the laser-heated samples, it is suggested that minor refocusing of the acoustic field could be adequate for better stabilization of the sample's horizontal position. Such refocusing could be achieved by carefully selected curvature of the acoustic reflector.

5.3 Conclusions

Experiments in microgravity were conducted with samples prepared of pressed ZrO_2, ZrN and Zr powders. It was observed that the vertical position of the levitating sample was well maintained by the uniaxial acoustic field during the laser heating of the sample to about 3000 K. In the conducted experiments, levitating samples could be continuously laser heated for about 1 sec that resulted in a local sample melting. Oscillations of the levitating samples in horizontal direction were significantly greater in microgravity than in normal gravity. These oscillations further increased during sample heating and eventually resulted in moving the sample out of the stable levitation position and away from the laser beam. An effort aimed for the stabilization of the sample's horizontal position that could be achieved with a refocused acoustic field is suggested to be necessary for successful containerless processing of high temperature molten samples in microgravity.

CHAPTER 6

PHASE EQUILIBRIA IN THE SYSTEM ZR-O-N

6.1 Introduction

Although ternary Zr-O-N phases are of interest for a number of applications, relatively little is known about phases and melting relations in the ternary Zr-O-N system. Melting relations are known only for the boundary systems Zr-O and Zr-N. No ternary melting relations have been reported.

Figure 6.1 shows the binary system Zr-O. Solid phases in this system are the α, β, and γ modifications of ZrO_2 and the α and β phases of Zr. The monoclinic α phase of ZrO_2, stable at ambient conditions, transforms to the tetragonal β phase at 1205 °C. Both phases exhibit very limited compositional variation. At 1525 °C, the cubic γ phase of ZrO_2 forms with an oxygen concentration of 63.6 at-%. The stability field of this oxygen-deficient phase widens with increasing temperature, and the γ phase coexists with the β phase until β disappears at 2377 °C. The γ phase melts homogeneously at 2710 °C. Zirconium exists at high temperatures in two modifications. The hexagonal α phase forms a solid solution with up to 29 – 35 at-% oxygen. At 863 °C, the oxygen-free α phase transforms into the tetragonal β phase. Both phases continue to form solid solutions, and coexist until the β phase melts incongruently at 1970 °C. At the peritectic melting point, the β phase has a maximum oxygen solubility of 10.5 at-%. The α phase reaches its highest oxygen solubility of 35 at-% at the eutectic with γ ZrO_2 at 2065 °C. It melts homogeneously at 2130 °C. Several ordered oxygen-rich modifications of the α phase exist at temperatures below 970 °C.
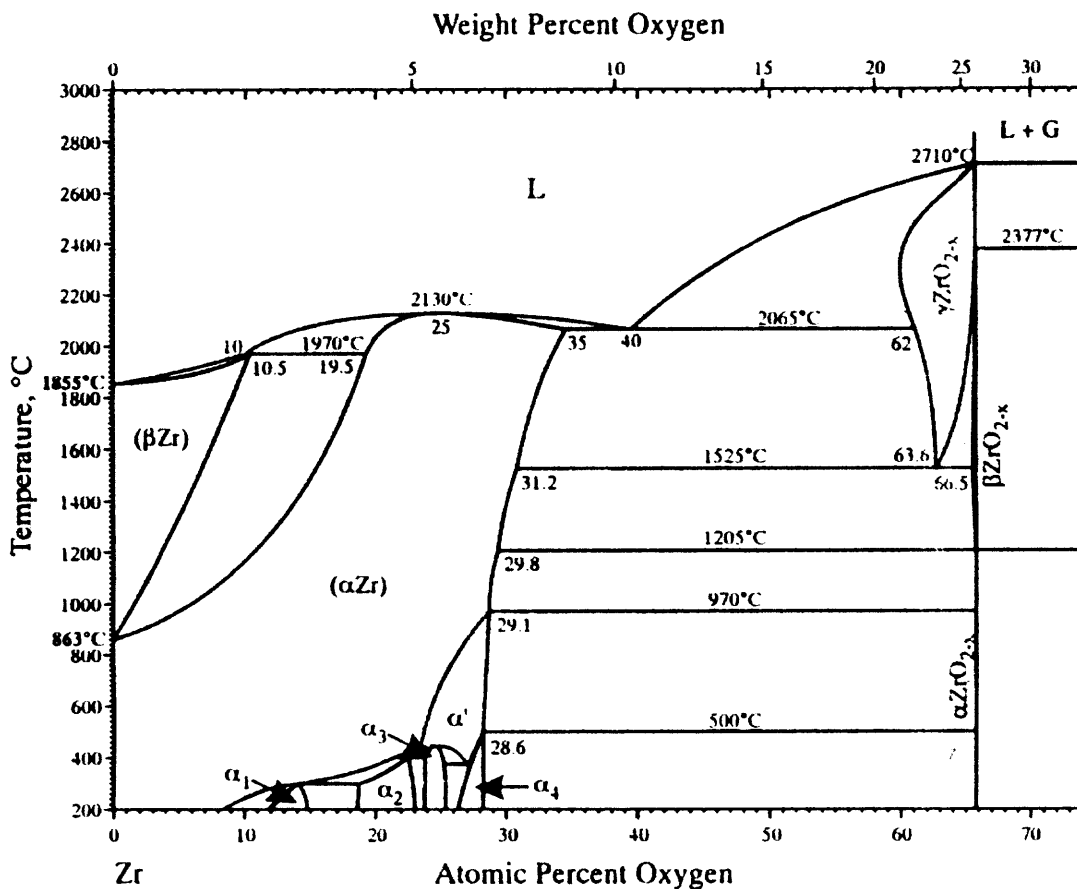
Figure 6.1 The system Zr-O (Abriata et al., 1986).

Figure 6.2 shows the binary system Zr-N. Zirconium shows a similar behavior as in the Zr-O binary system: the α solid solution exists over a wide compositional range, at its maximum it contains 24.7 at-% nitrogen. The N-rich a phase melts incongruently at 1988 °C to form melt and the cubic ZrN phase. The β phase melts incongruently with a maximum N concentration of 5 at-%. The stability field of ZrN expands towards lower than stoichiometric N concentrations up to the peritectic melting of α-Zr. The lowest N concentration is 40 at-%. ZrN itself decomposes incongruently to form a Zr-rich melt and a gas phase at 3410 °C.
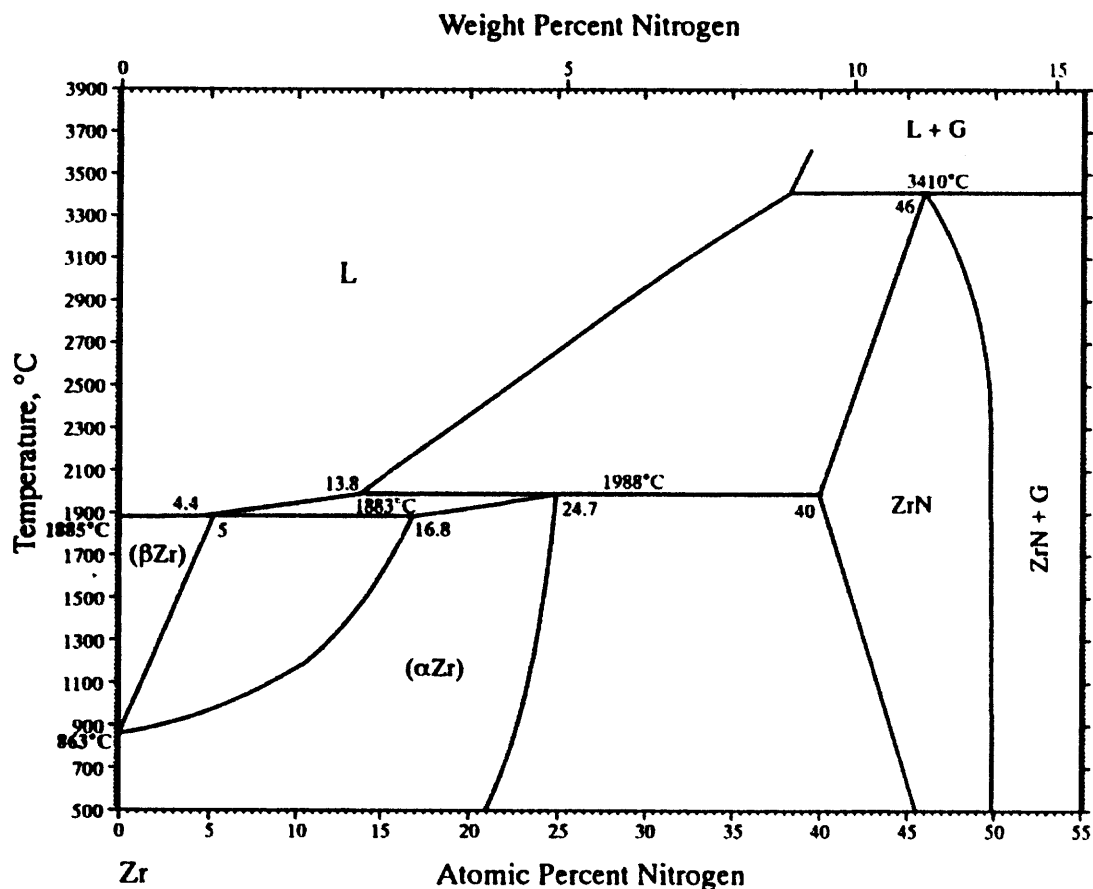
Figure 6.2 The system Zr-N (Gribaudo et al., 1994).

Ternary Zr-O-N phases exist along the substitution series $ZrO_{2-2x}N_{4x/3}$. Figure 6.3 shows the ZrO_2-$ZrN_{4/3}$ pseudobinary system. All oxynitride phases, including the end member $ZrN_{4/3}$ decompose into ZrN and nitrogen gas above 800 °C (Lerch, 1998, Lerch et al., 1996). The individual phases are $ZrN_{4/3}$, Zr_2ON_2 (γ), $Zr_7O_8N_4$ (β), $Zr_7O_{9.5}N_3$ (β''), and $Zr_7O_{11}N_2$ (β').
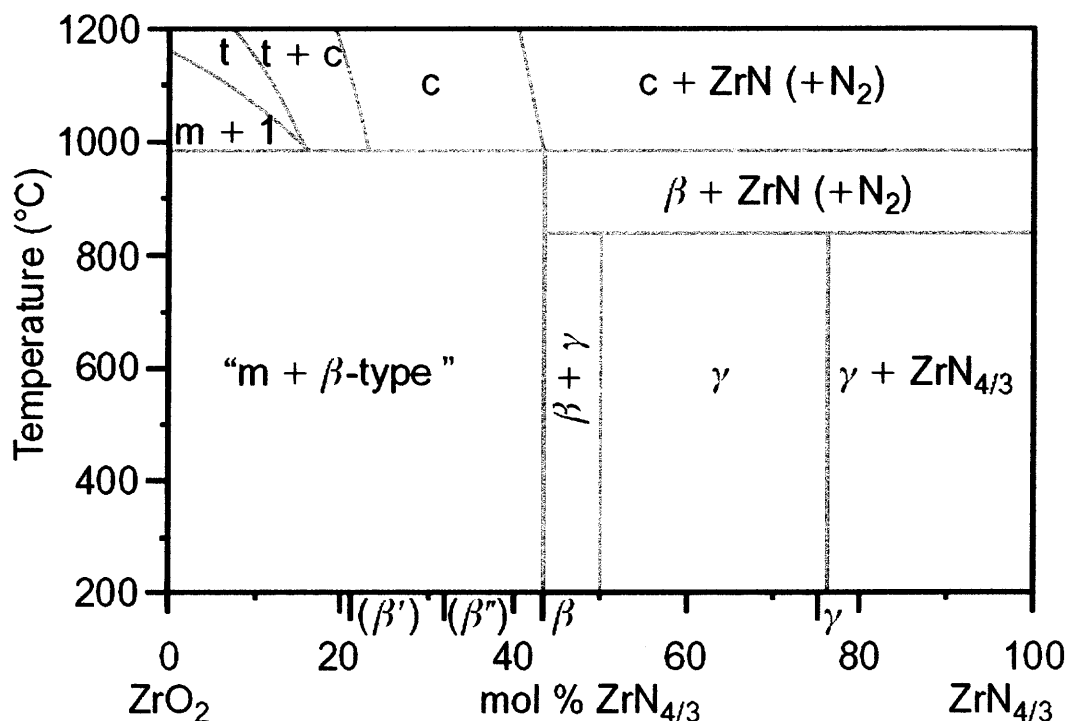
Figure 6.3 The ZrO_2-$ZrN_{4/3}$ pseudobinary system. (Lerch, 1998).

The ternary system itself has not yet been comprehensively investigated. Dreizinand Hoffmann (1999) determined phase compositions in quenched Zr samples that were partially combusted in air. The results of this investigation are shown in Figure 6.4. The Zr metal samples reacted partially with air at the combustion temperature of zirconium metal, ~2400 °C (Molodetsky et al., 1997). Besides the ZrO_2-$ZrN_{4/3}$ oxynitride phases, Zr-rich inclusions were reported with compositions that scattered between the ZrN and $ZrO_{0.25}$. The nature of these inclusions was not further specified.
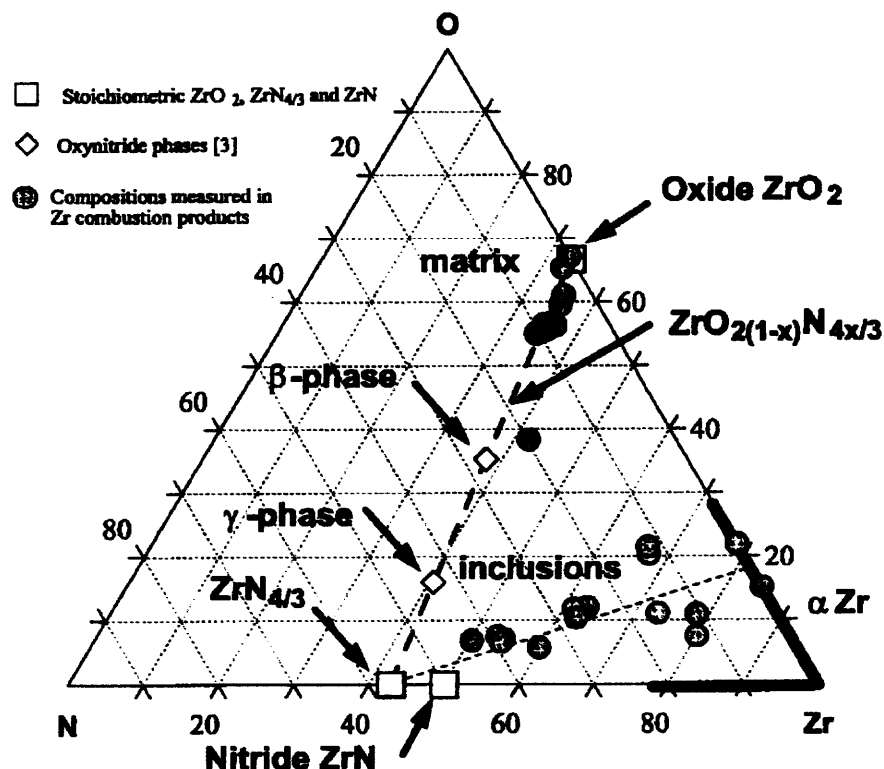
Figure 6.4 Phase compositions in quenched samples from Zr combustion in air. (Dreizin and Hoffmann., 1999).

The goal of the present study is to further investigate existing phases and melting relations in the Zr-O-N ternary system. Samples with specific compositions are being laser-heated above the melt formation. Recovered samples will be characterized by SEM and EDX.

6.2 Experimental

A set of samples in the ternary system $Zr-ZrO_2-ZrN$ has been heated with a CO_2 laser in argon. Spherical samples of 2 mm diameter were prepared as a mixture of Zr, ZrO_2, and ZrN. Component powders were mixed in a shaker mill, pressed into pellets and ground to spherical shape as described above in Chapter 5.1. Sample starting compositions are

the same as used for microgravity experiments, as shown in Figure 2.1 and also in Table 6.1 below.

Table 6.1 Sample starting compositions. Compositions are given in at-%.

Sample	Zr	ZrO_2	ZrN
A	10	80	10
B	10	45	45
C	10	10	80
D	0	90	10
E	0	50	50
F	0	10	90
G	10	90	0

The setup used in microgravity and described above in details, was modified and used in this experiments. Figure 6.5 shows the schematic diagram of the setup. The CO_2 laser beam is enclosed by the beam enclosure which enters the chamber. The ZnSe lens is placed inside the flange attached to the beam enclosure right before the chamber inlet. To heat the sample more uniformly, the golden mirror is attached to the opposite wall of the chamber.

A cylinder of about 2 mm base radius and 5 mm height, placed into the chamber on a 3D positioner stage serves as a pedestal for the spherical sample. To avoid contamination of the sample during heating, the pedestal is made of the same material as the sample. Using the diode pointer, which is aligned with the CO_2 laser, the beam is adjusted so that it uniformly illuminates the sample from both sides. Necessary adjustments can be made by moving the lens in horizontal directions, by changing the reflection angle of the mirror, and by moving the positioner in any direction. When the

desired position of the lens and the sample is achieved, the chamber is locked, evacuated, and filled with argon.
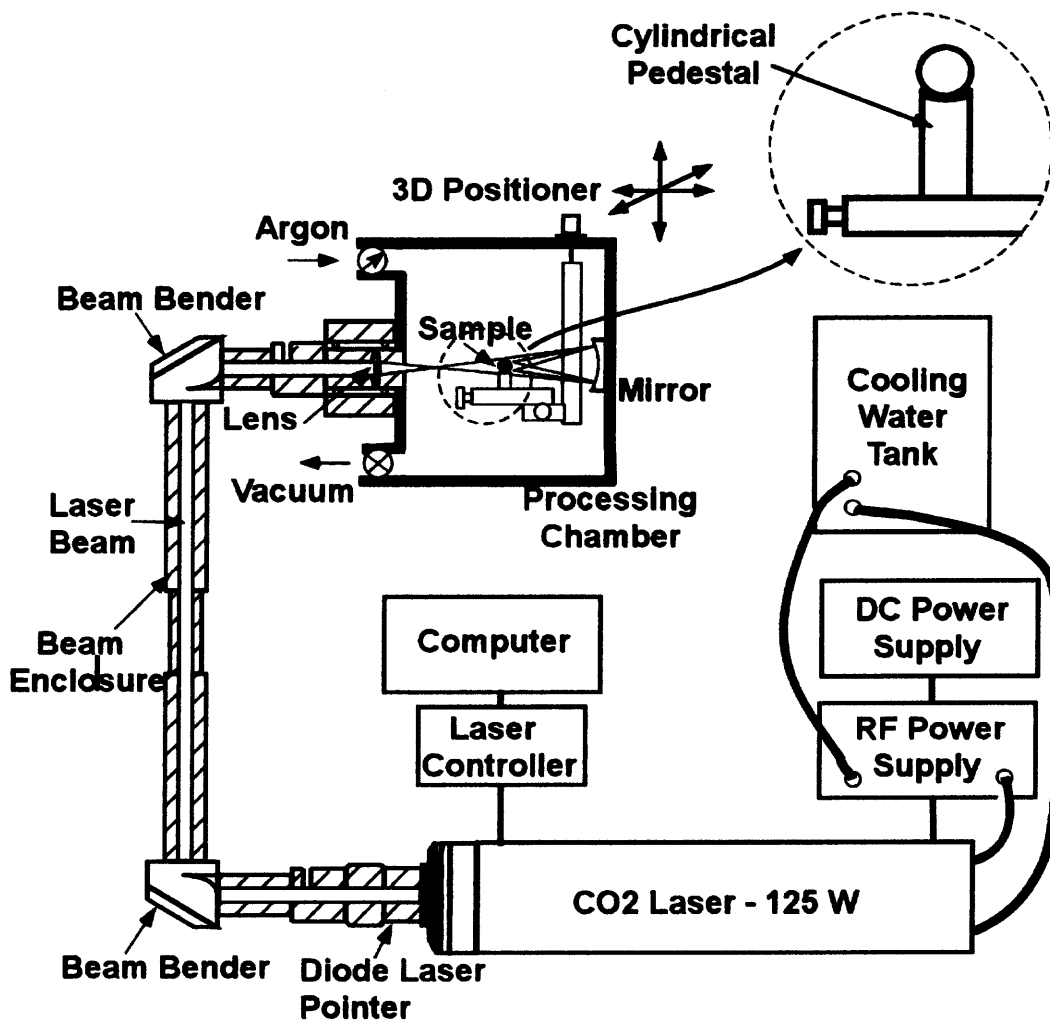
Figure 6.5 Schematic diagram of the experimental setup.

The CO_2 laser operation is controlled by the by LabView™ software and a custom designed Virtual Instrument (VI). The gating signal of preset duration is sent from the DAQ board to the laser controller thus enabling the laser. The duration of the

gate signal was chosen to be long enough to be able to melt the sample and keep it at constant temperature at thermal equilibrium. An 8 s laser pulse of 100 kW was used in these experiments.

After a period of melting and equilibration, the samples were quenched by natural cooling. Quench rates are estimated to 10^3 K/s..

The samples thus obtained were cross-sectioned and polished for SEM imaging and phase analysis by EDX.

6.3 Results

The samples can be divided into three distinct groups.

The ZrO_2-rich samples A, D, and G all were completely molten, and showed large interior voids. This is illustrated in Figure 6.6, showing a backscattered electron image of sample G. Figure 6.7 shows a magnified representative view of the texture of sample A. The bulk of these samples consists mainly of large grains (> 10 µm) with ZrO_2 composition. A more Zr-rich phase was present along grain boundaries. The composition of this phase showed an approximate Zr/O ratio of 2. The large ZrO_2 grains showed distinct exsolution lamellae with essentially the same composition as the grain boundary phase, indicative of the existence of an extended solid solution at high temperatures. The N concentration in any of these samples was below the detection limit.

The ZrN-rich compositions C and F did not melt completely, and showed multiple smaller interior voids. Figure 6.8 shows an image of sample F. The samples consisted of rounded bright grains of ~ 10 µm diameter embedded in a darker matrix. The matrix phase was confirmed to be ZrO_2 by EDX.
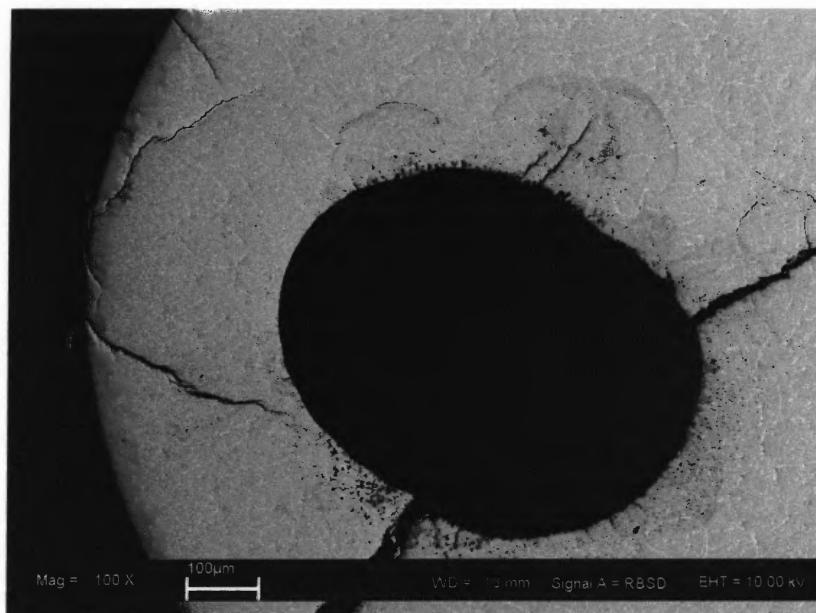
Figure 6.6 Backscattered electron image of sample G. The sample was completely molten, and shows a large central void. This texture is typical for the ZrO_2-rich compositions A, D, and G.
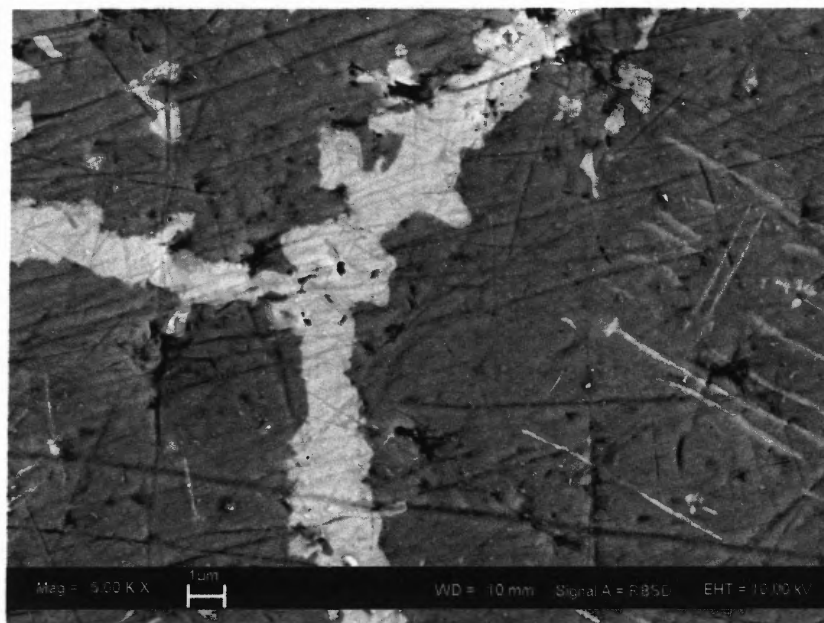
Figure 6.7 Texture of sample A. A bright, Zr-rich phase is located along the boundaries of large ZrO_2 grains. Exsolution features are visible within the ZrO_2 phase.
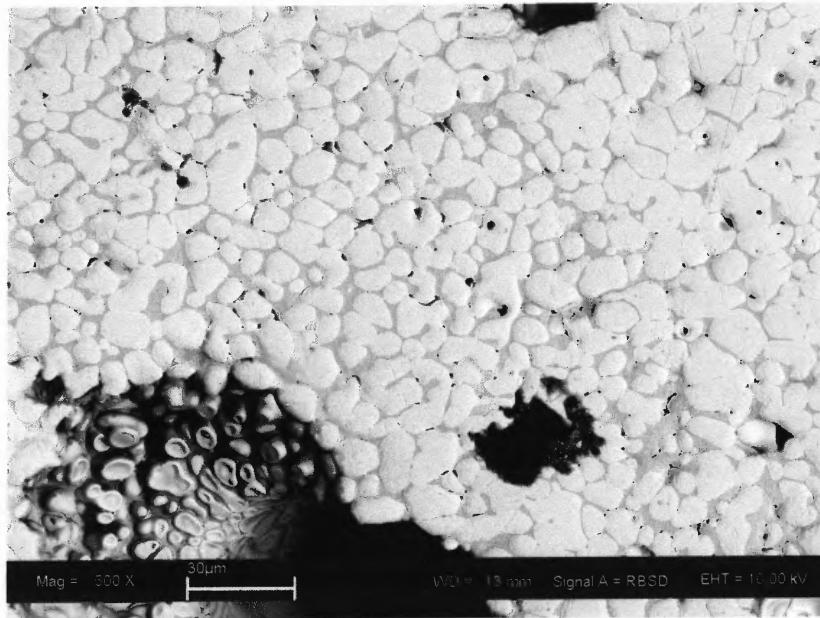
Figure 6.8 Sample F consists of bright round oxygen-deficient grains in a darker (ZrO_2) matrix. This texture is typical for samples C and F.
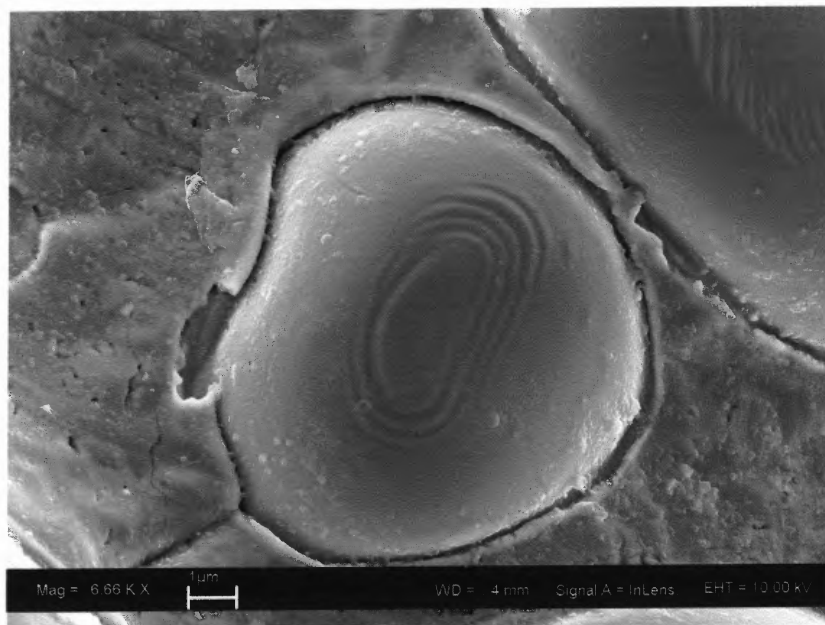
Figure 6.9 Secondary electron image of a spheroidal grain protruding into a void of sample C. The surface morphology is possibly indicates dissolution or decomposition of the phase.

The bright grains exhibit a surface morphology typical for dissolution of a solid phase in a melt. Figure 6.9 shows one spheroidal bright grain protruding into a cavity in sample C. Elemental analysis of the brighter phase showed Zr/O ratios above 2, and intermediate, widely scattering N concentrations. No unaltered ZrN was detected, therefore the sample must have at least partially equilibrated. Bulk EDX analysis of the whole image did not coincide with the starting composition. Significant amounts of nitrogen were lost during heating, and the sample oxidized partially from impurities in the atmosphere.

The resulting texture of the intermediate compositions B and E were not uniform. Figure 6.10 shows an overview of sample E. The center of the sample shows a texture identical to the whole of the ZrN-rich samples C and F. The dark and bright phases also show the same compositions as in samples C and F. The outer portion of sample E consists of regions of intimate intergrowth of dark and bright phases (shown in Figure 6.11), surrounding dendritic grains of a darker phase. A dendrite growing freely in the largest void of sample E is shown in Figure 6.12. The dark phase is again identified as ZrO_2 by EDX. The bright phase in the fine-grained regions has the same scattered composition as seen in samples C, F, and the center of E. As the fine-grained texture could indicate eutectic solidification, the local bulk composition of these regions was determined.
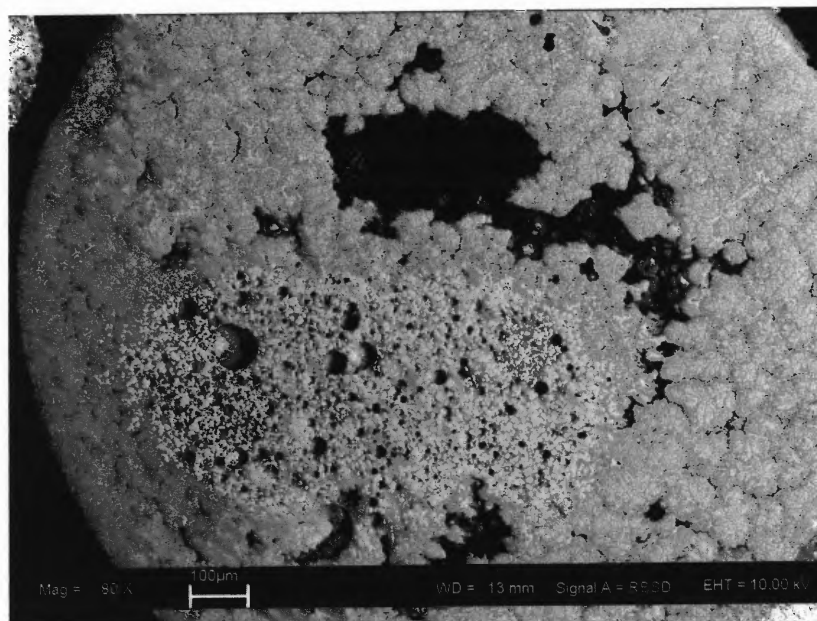
Figure 6.10 Overview of sample E. The sample consists of a central region with a texture similar to that of C and F (above), and a largely molten outer region.
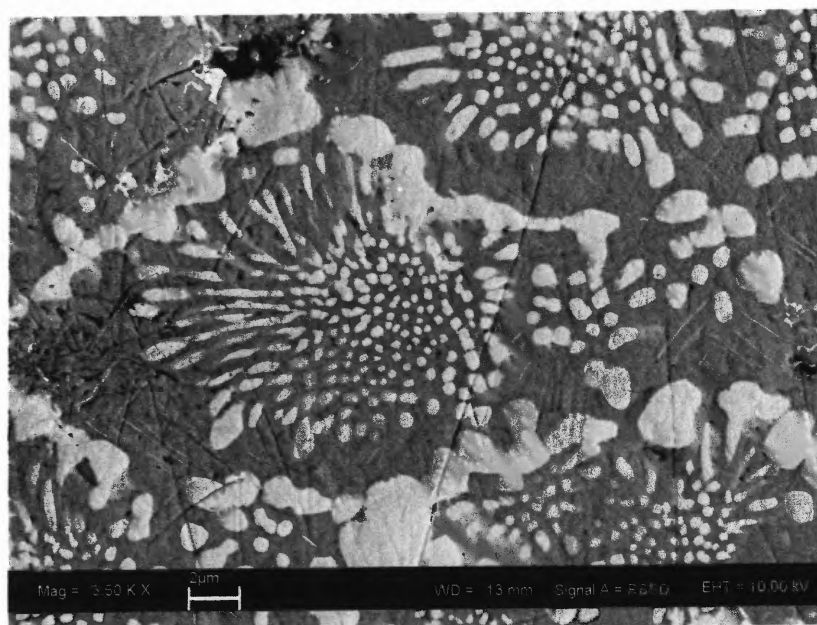
Figure 6.11 Magnified view of outer region of sample E showing intimate intergrowth of dark and bright phases. Note that the dark phase (ZrO_2) shows exsolution features as in samples A, D, and G (above).
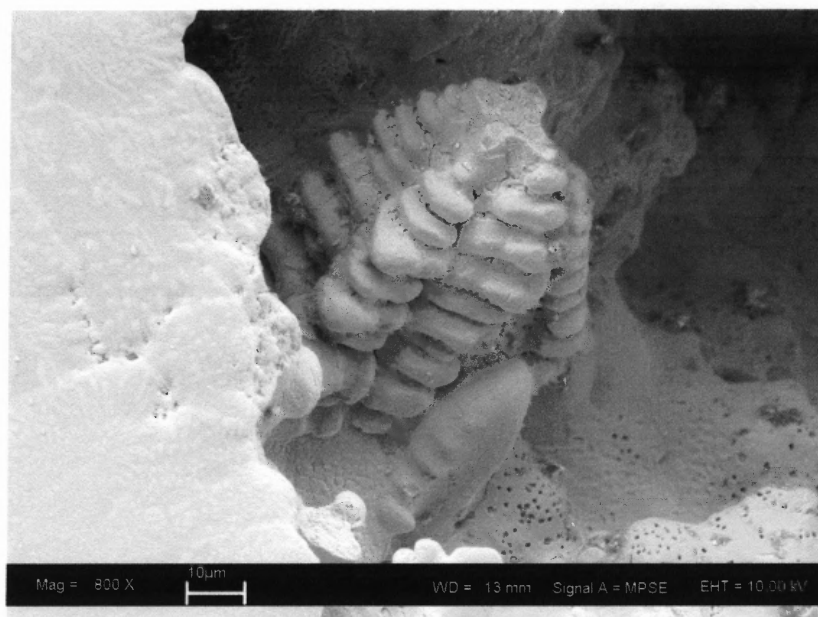
Figure 6.12 A free-standing dendrite in the large cavity of sample E.

The analyses of the individual bright phases scatter widely between ZrN and the N-free α-Zr phase. A similar result has been found in a Zr combustion study by Dreizin et al. (1999). The authors report bright inclusions in a dark melt within quenched partially burned Zr particles. The composition of these bright inclusions scatters along the line shown in gray in Figure 6.13. From the elemental analysis, it can not be decided unambiguously whether the bright phase represents the α-Zr or the ZrN solid solution. The dashed arrow on Figure 6.13 indicates the development of the bulk composition of sample C before and after heating. Clearly, significant amounts of nitrogen were lost, and some oxygen was absorbed from impurities in the experimental environment. The local bulk analyses of regions with eutectic textures (samples B and E) are marked with a dashed outline.

To identify the nature of the Zr-rich phase present in all ZrN-rich samples, a separate sample with composition B (see Figure 2.1, Table 7.1) was heated and quenched both in argon, and in air. X-ray diffraction patterns were collected. Figure 6.14 shows the XRD pattern of the sample heated in Ar. Only monoclinic ZrO_2, cubic ZrN, and hexagonal α-Zr were detected. The sample heated in air contained besides monoclinic ZrO_2 only cubic ZrO_2. The cubic ZrO_2 phase is likely stabilized by low N concentration – however, no other N-containing phase was detected. The results of the phase analysis are shown in Table 6.3.

Table 6.2 Results of EDX phase analysis. Compositions are given in mol-%. Composition normalized to oxide and nitride ($ZrN_{4/3}$ as opposed to ZrN) components are shown as reference to Figure 6.13.

Sample and Phase description	Zr	O	N	Zr	ZrO_2	$ZrN_{4/3}$
A (starting composition)	**41.67**	**53.33**	**5.00**	**11.3**	**80.0**	**8.8**
bright phase - grain boundary	61.08	39.86	0.00	40.8	59.2	0.0
bright phase - inclusion	80.22	34.73	0.00	54.7	45.3	0.0
bright phase - grain boundary	62.76	35.86	1.38	43.8	53.8	2.4
dark phase	31.13	67.45	1.42	0.0	97.6	2.4
bulk analysis	35.63	67.54	0.00	1.8	98.2	0.0
B (starting composition)	**47.50**	**30.00**	**22.50**	**15.6**	**45.0**	**39.4**
dark phase	30.33	71.92	0.00	0.0	100.0	0.0
bright phase	64.34	23.04	12.62	43.4	34.6	22.1
bright phase	64.57	29.75	5.69	45.4	44.6	10.0
bright phase	72.40	14.79	12.81	55.4	22.2	22.4
bright phase	63.51	15.56	20.93	40.0	23.3	36.6
bright phase	61.89	11.05	27.06	36.1	16.6	47.4
bright phase	64.47	10.30	25.23	40.4	15.5	44.2
bright phase	62.50	19.18	18.32	39.2	28.8	32.1
brgt. ph. in fine-grained region	66.81	18.06	15.12	46.4	27.1	26.5
local bulk of fine-grained region	42.07	48.59	9.34	10.8	72.9	16.3
local bulk of fine-grained region	44.16	49.37	6.47	14.6	74.1	11.3
local bulk of fine-grained region	46.55	44.42	9.03	17.6	66.6	15.8
local bulk of fine-grained region	43.67	47.22	9.12	13.2	70.8	16.0
C (starting composition)	**53.33**	**6.67**	**40.00**	**20.0**	**10.0**	**70.0**
bright phase	75.37	19.51	5.12	61.8	29.3	9.0
bright phase	73.11	30.10	0.00	56.3	43.7	0.0

Table 6.2 (Continued)

|						
bright phase	59.48	29.88	10.64	36.6	44.8	18.6
dark phase	31.95	68.77	0.00	0.0	100.0	0.0
C (repeat)						
bright phase	61.55	10.60	27.84	35.4	15.9	48.7
bright phase	55.85	13.58	30.56	26.1	20.4	53.5
dark phase (melt texture)	32.42	68.37	0.00	0.0	100.0	0.0
bright phase, near void	51.14	11.83	37.03	17.5	17.7	64.8
bright phase, 50 µm from void	57.04	12.55	30.41	28.0	18.8	53.2
bulk analysis	58.41	24.86	16.73	33.4	37.3	29.3
D (starting composition)	**35.19**	**59.26**	**5.56**	**1.4**	**88.9**	**9.7**
bulk analysis	35.76	65.38	0.00	3.0	97.0	0.0
E (starting composition)	**41.67**	**33.33**	**25.00**	**6.3**	**50.0**	**43.8**
central region						
bright phase	68.82	3.27	27.92	46.2	4.9	48.9
bright phase	78.30	8.81	12.89	64.2	13.2	22.6
bright phase	66.84	12.26	20.91	45.0	18.4	36.6
bright phase	55.11	1.86	43.03	21.9	2.8	75.3
bright phase	53.88	8.89	37.22	21.5	13.3	65.1
dark phase (melt texture)	30.27	71.69	0.00	0.0	100.0	0.0
outer region						
bright phase	57.71	13.87	28.41	29.5	20.8	49.7
local bulk of fine-grained region	36.52	48.96	14.52	1.2	73.4	25.4
local bulk of fine-grained region	41.91	51.51	6.59	11.2	77.3	11.5
local bulk of fine-grained region	38.14	53.23	8.62	5.1	79.9	15.1
local bulk of fine-grained region	36.52	54.12	9.36	2.4	81.2	16.4
local bulk of fine-grained region	41.18	51.11	7.71	9.8	76.7	13.5
local bulk of fine-grained region	40.92	48.89	10.20	8.8	73.3	17.8
F (starting composition)	**48.15**	**7.41**	**44.44**	**11.1**	**11.1**	**77.8**
bright phase	58.64	9.31	32.05	29.9	14.0	56.1
bright phase	57.97	6.40	35.63	28.0	9.6	62.4
bright phase	58.63	9.44	31.93	30.0	14.2	55.9
bright phase	65.98	7.30	26.72	42.3	11.0	46.8
bright phase	60.23	6.48	33.29	32.0	9.7	58.3
dark phase (melt texture)	32.59	63.82	3.59	0.0	93.8	6.2
G (starting composition)	**40.00**	**60.00**	**0.00**	**10.0**	**90.0**	**0.0**
bulk analysis	38.02	71.48	0.00	2.1	97.9	0.0
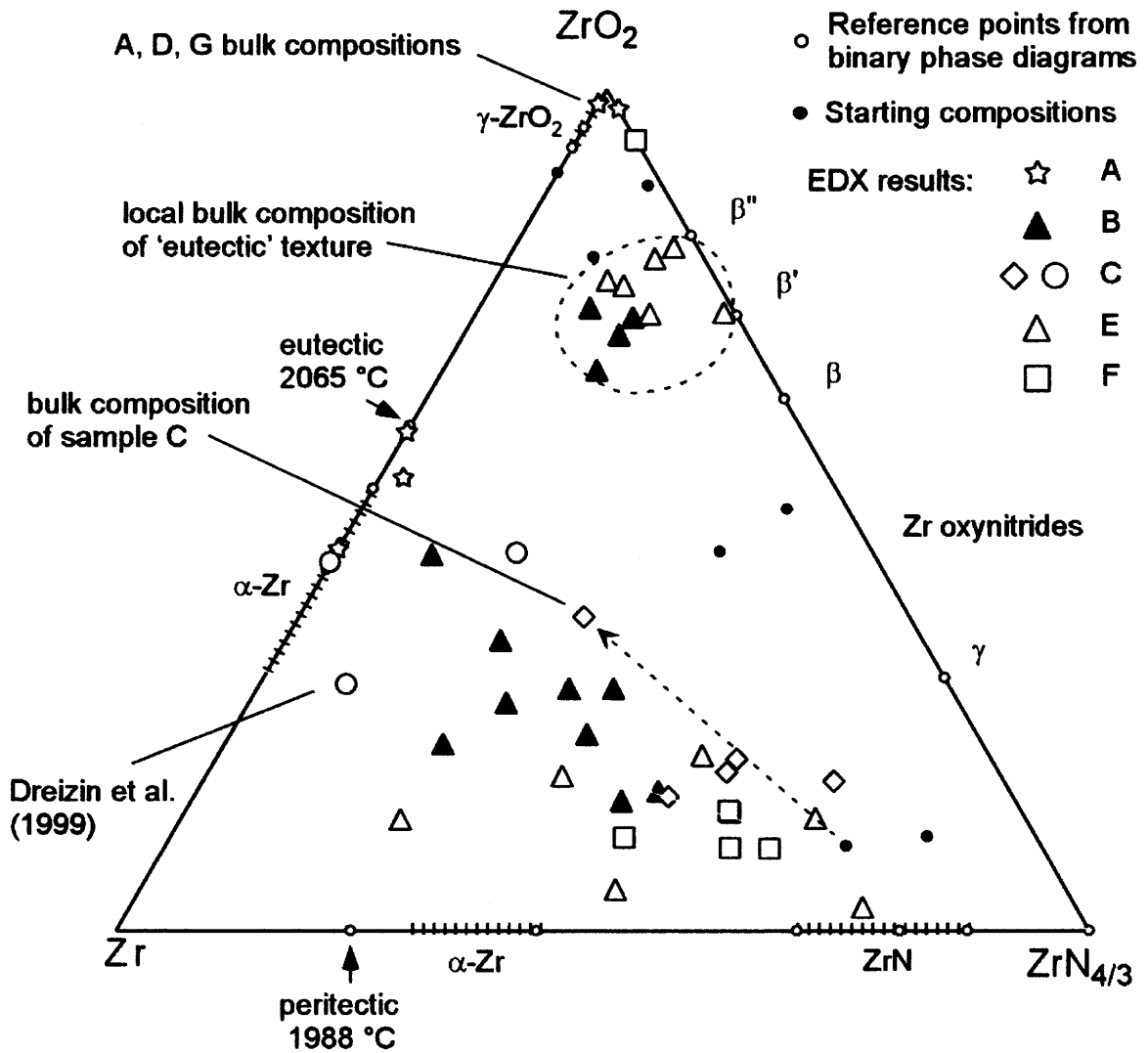
Figure 6.13 Results of EDX analysis of quenched Zr-O-N samples.
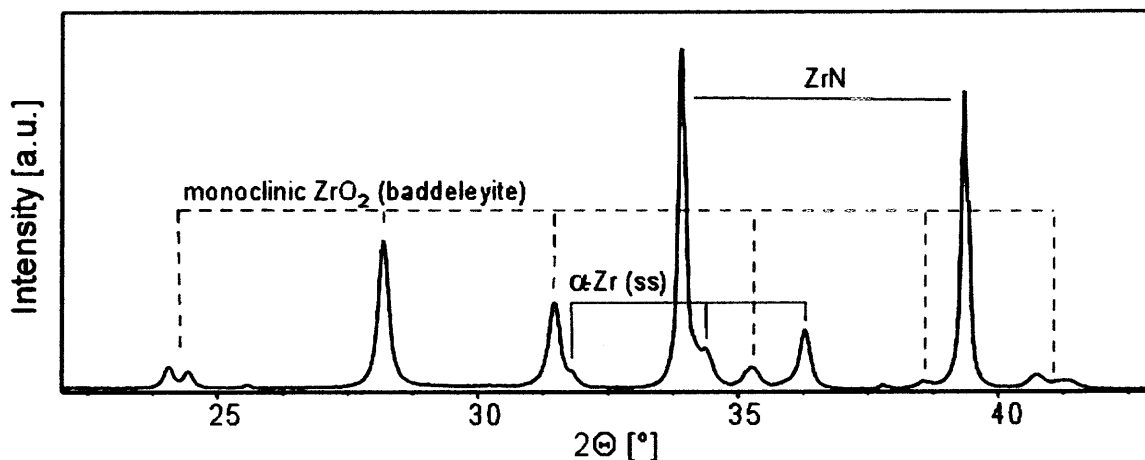
Figure 6.14 XRD pattern of a sample with composition B heated in Ar.

Table 6.3 Results of phase analysis of a sample with composition B. Standard deviations of the least significant digit are shown in parentheses.

|		heated in argon	heated in air
α-Zr	a_0 [Å]	3.2459(3)	
	c_0 [Å]	5.209(1)	
	V [Å^3]	47.530(9)	
	[wt-%]	6.4(1)	
ZrN	a_0 [Å]	4.5749(1)	
	V [Å^3]	95.753(7)	
	[wt-%]	47.3(1)	
ZrO$_2$, mon.	a_0 [Å]	5.3122(5)	5.309(1)
	b_0 [Å]	5.2076(5)	5.200(1)
	c_0 [Å]	5.1472(4)	5.149(1)
	γ [°]	99.173(7)	98.98(1)
	V [Å^3]	140.57(2)	140.41(6)
	[wt-%]	46.3(2)	67.0(2)
ZrO$_2$, cub.	a_0 [Å]		5.1094(7)
	V [Å^3]		133.38(5)
	[wt-%]		33.0(2)

The quantitative analysis shows that the sample heated in Ar consists to about equal proportions (by weight) of cubic ZrN and monoclinic ZrO$_2$. The composition of the cubic ZrN phase is not readily determined, however. The unit cell volume

determined here of 95.753(7) Å^3 compares well with values reported in the PDF reference database for stoichiometric ZrN (Powder Diffraction File PDF-2). However, no structural information about an oxygen-poor cubic ZrO_xN_y solid solution could be located. It can therefore not be distinguished between unreacted ZrN, or a cubic ZrO_xN_y solid solution, and decision whether the Zr-rich phase detected by SEM/EDX in most of the samples is a cubic (ZrN) or a hexagonal solid solution (α-Zr) must therefore be deferred to further investigations.

6.4 Discussion

The ternary phase diagram can be constructed from reference points in the binary system diagrams, shown in Figures 6.1 and 6.2. On the ternary liquidus, the binary eutectic L + α-Zr + ZrO_2, (2065 °C, Figure 6.1) and the binary peritectic L + α-Zr + ZrN (1988 °C, Figure 6.2) lead to the same ternary invariant point: L + α-Zr + ZrO_2 + ZrN (T1 for reference). Further, the decompositions of both, ZrO_2 and ZrN into melt and a gas phase (occurring at 2710 °C and 3410 °C for the respective binary systems, cf. Figures. 6.1, 6.2) necessarily lead to a second ternary invariant point, characterized by the equilibrium L + G + ZrO_2 + ZrN (T2 for reference). If no additional phases are present, these invariant points are connected by the univariant equilibrium L + ZrO_2 + ZrN. These relations are summarized in Figure 6.15.

The locations of these invariant points are unknown a priori. Several constraints can, however, be obtained from experimental evidence and from the melt compositions of the relevant binary invariant points.
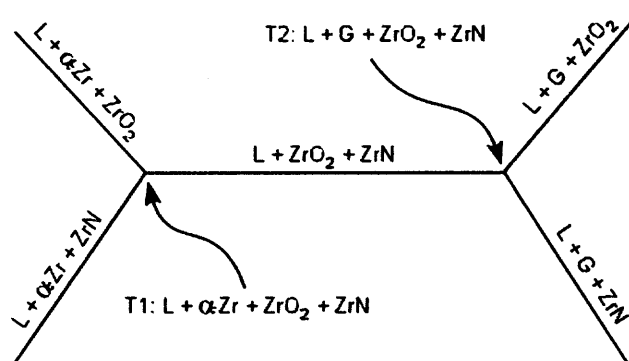
Figure 6.15 Schematic phase relations of melting equilibria in the Zr-O-N system.

It was observed that in the recovered samples B and E, regions exist with a texture typical for eutectic solidification (see Figure 6.11 above). The darker phase was identified as nitrogen-free ZrO_2, but EDX analysis of the brighter phase was not possible because of the small size of the respective inclusions. The bulk composition of these regions suggests, as shown in Figure 6.13, that at least locally, ZrO_2 was in equilibrium with a ZrN solid solution, indicative of the high-temperature equilibrium $L + ZrO_2 +$ ZrN. The abundance of voids in the sample (see esp. Figure 6.10) additionally indicates the presence of a gas phase, suggesting that the samples were near the invariant point T2.

Additional information can be recovered from previously reported research on Zr combustion in air. Figure 1-4 above shows the development of the bulk concentration of oxygen and nitrogen in a burning Zr particle. During combustion, both nitrogen and oxygen concentrations initially increase, until nitrogen concentration reaches a maximum. The oxygen concentration continues to increase, but nitrogen decreases – suggesting that as the temperature decreases, the system approaches the univariant equilibrium L + G + ZrN. The bulk composition of the burning Zr particle continues to

evolve until at a maximum oxygen concentration, large amounts of gas are released, and the particle explodes. This phenomenon occurs at approximately 2100 °C, and results in the formation of solid ZrO_2. Therefore, it likely represents the ternary invariant point T2: $L + G + ZrO_2 + ZrN$. Figure 6.15 summarizes these constraints on the ternary liquidus.

Figure 6.16 shows that, allowing for some uncertainty in the elemental analysis, the local composition in the present sample coincide with the composition of Zr particles burning in air at the moment of their explosion. This supports the notion that this composition represents the invariant point T2. With this consideration, and given the experimental constraints, the ternary liquidus is proposed as shown in Figure 6.17

Subsolidus relations can equally be derived from the binary systems and from the experimental evidence. The α-Zr and β-Zr solid solutions exist in both, Zr-O and Zr-N binary systems, as shown in Figures 6.1, 6.2. The existence of equivalent ternary solid solutions with similar temperature dependence is therefore a straightforward assumption. It is not known how much oxygen the ZrN phase can contain, and how this equilibrium concentration depends on temperature. Analysis of the bright phases in samples recovered in this study shows a wide, apparently homogeneous region of a phase which could either be the α-Zr solid solution, a hypothetical extended ZrO_xN_y solid solution, or a mixture of both. The XRD analysis discussed above suggests that a ZrN-derived solid solution is prominent in the present samples. It is therefore likely that an extended ZrN-derived solid solution exists. Based on these arguments, the suggested subsolidus phase relations in the Zr-O-N system are outlined in Figure 6.18. This discussion does not account for the oxynitride phases along the ZrO_2-$ZrN_{4/3}$ pseudobinary join, and is therefore strictly relevant only above the oxynitride decomposition.
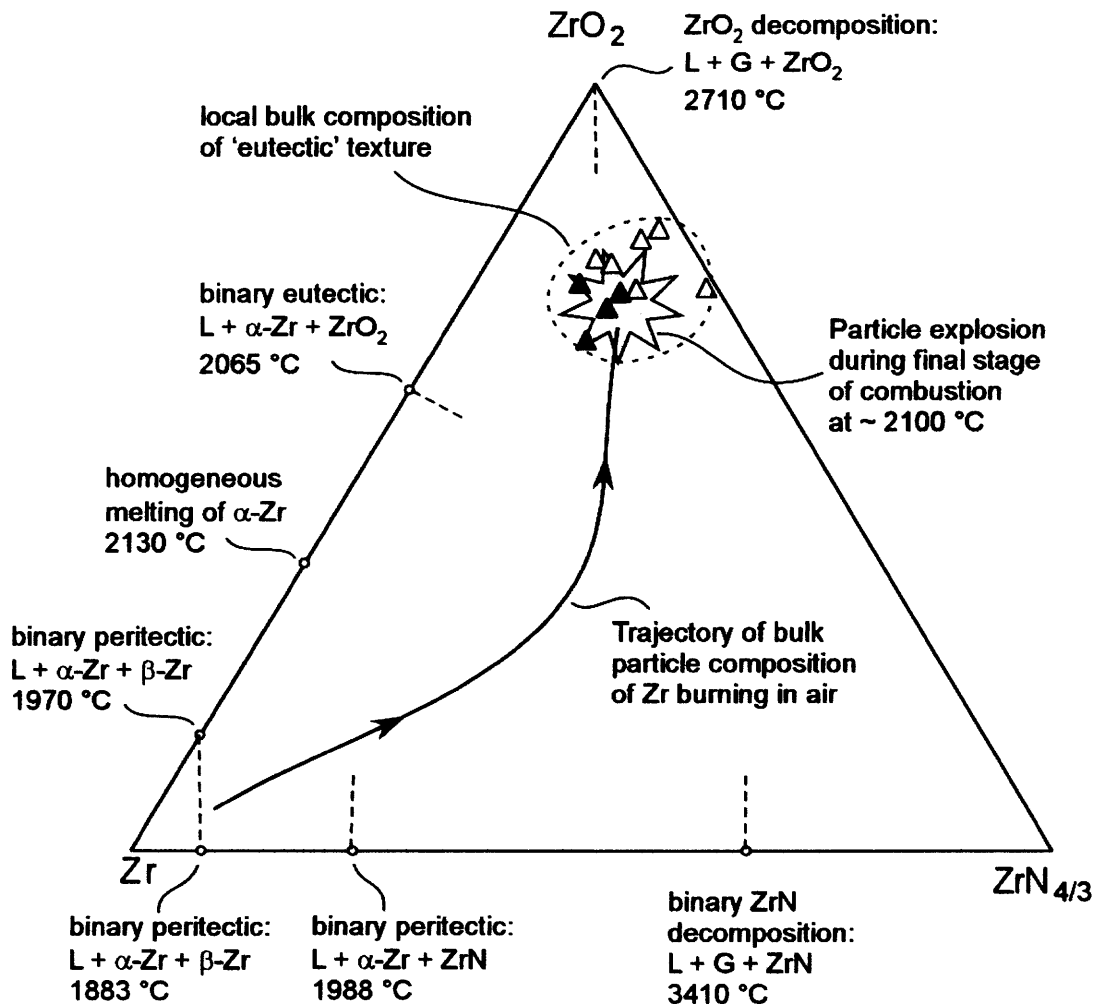
Figure 6.16: Experimental constraints on the ternary liquidus in the Zr-O-N system. The binary invariant points were derived from the diagrams shown in Figures 6.1 and 6.2. Local bulk sample compositions correspond to the analyses shown in Figure 6.13. The trajectory of Zr particle combustion in air was derived from Figure 1.4 (Molodetsky et al., 1997).
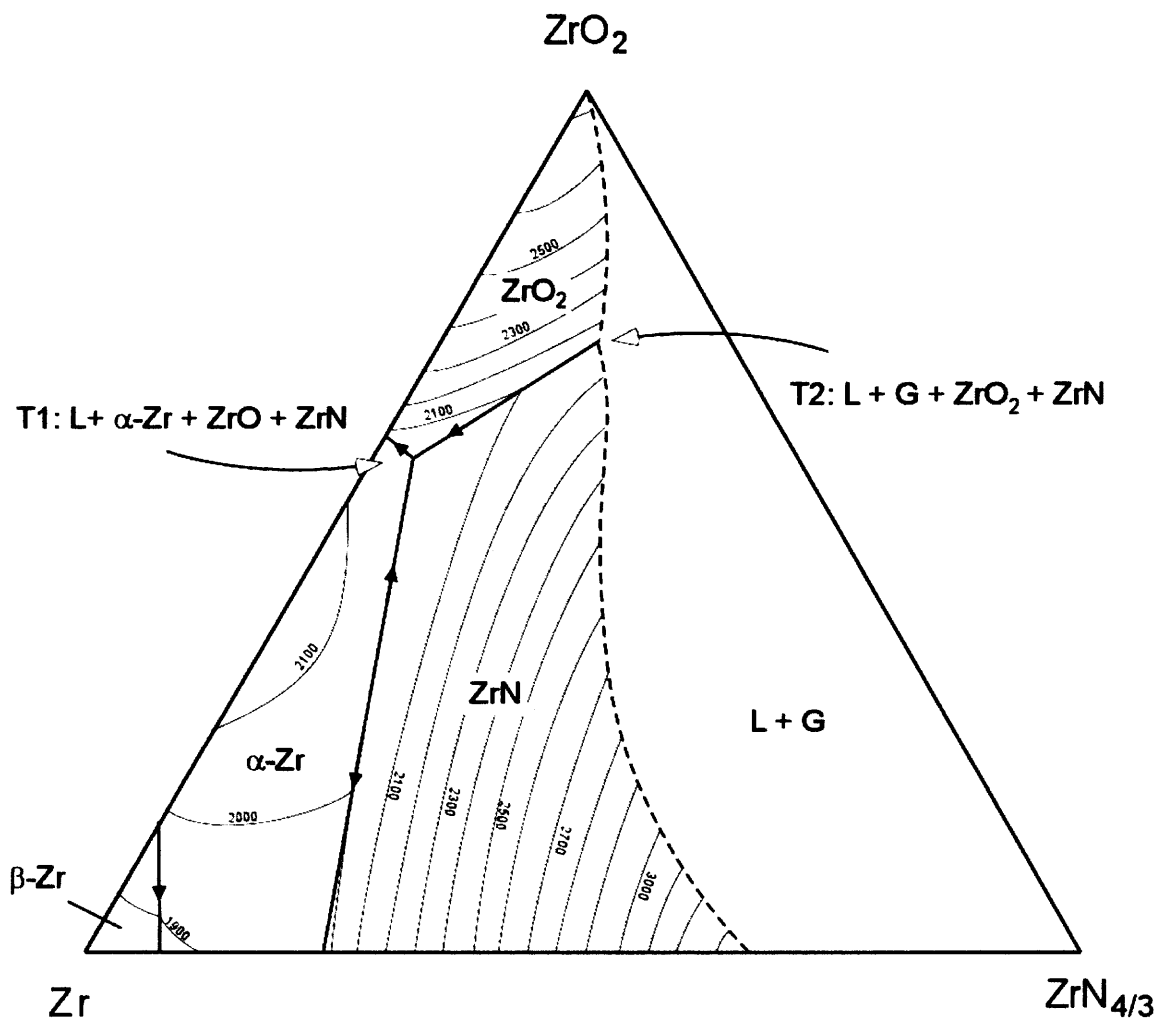
Figure 6.17 Proposed liquidus of the Zr-ZrO₂-ZrN₄/₃ ternary system.
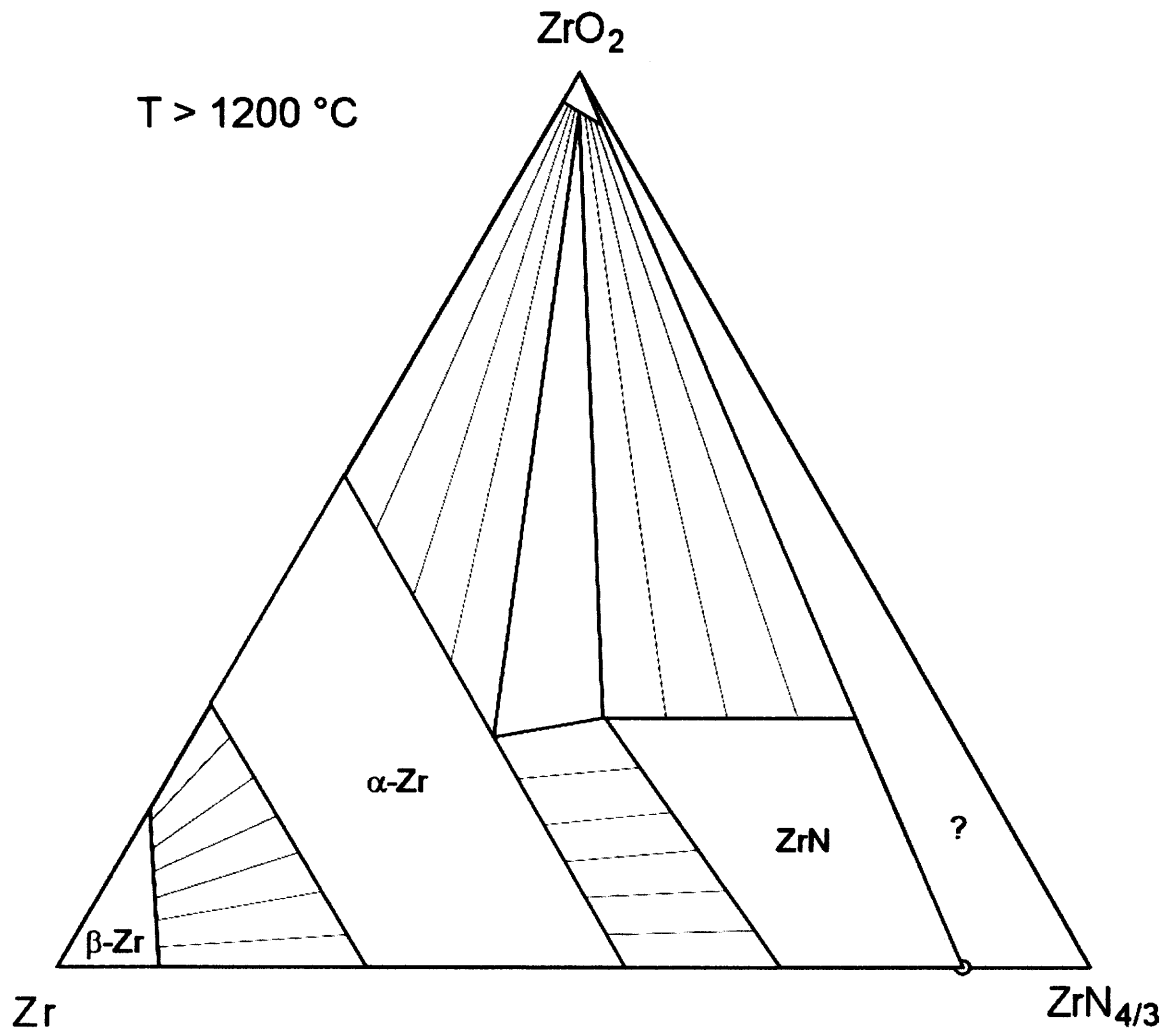
Figure 6.18 Proposed subsolidus phase relations in the Zr-ZrO_2-$ZrN_{4/3}$ ternary system.

6.5 Conclusions

Investigations of laser-heated samples representing different Zr-O-N compositions and produced by pressed Zr, ZrO_2, and ZrN powders pointed to the location of the ternary invariant point $L + G + ZrO_2 + ZrN$ on the high-temperature portion of the $Zr-ZrO_2-ZrN$ phase diagram. Comparisons of the results obtained in this work and composition histories of the zirconium particles burning in air reported earlier (Molodetsky...) enabled us to further constrain the ternary liquidus in the Zr-O-N system. Elemental analyses of the nitrogen-rich inclusions found in the samples showed existence of an extended compositional range for the ternary solid Zr-O-N solutions. X-ray diffraction analysis of the quenched samples indicated that these solutions are likely to be derived from the ZrN phase. A preliminary outline of the subsolidus ternary $Zr-ZrO_2-ZrN$ phase diagram is constructed based on these findings and the interpretations of the well-known binary Zr-O and Zr-N phase diagrams.

CHAPTER 7

CONCLUSIONS

A technique for studying phases in highly reactive, molten, metal based systems was developed and tested. A containerless experimental configuration combined with the microgravity environment was used.

Different containerless techniques were reviewed and the acoustic levitation was selected for the microgravity experiments. The selection criteria included a capability to levitate both conductive and non-conductive (e.g., ceramics) materials, simplicity of control and operation, an access for the sample quenching, the ability to decouple the sample heating and levitation controls, and the capability to levitate samples at 1 atm and high-temperature. While none of the known techniques was shown to satisfy all of the criteria, the acoustic levitation was found to meet most requirements. The main challenge was identified as the capability to maintain the sample levitation during its heating to very high temperatures that were of interest in this study.

The experimental setup that included a chamber with controlled environment, an acoustic levitator, a 125 W CO_2 laser, and a quenching mechanism, was designed and built. The experimental apparatus was prepared for the microgravity tests onboard the NASA KC-135 airplane flying parabolic trajectories. Control of the experiment was completely computerized which was critical for the success of the microgravity experiments considering the time restrictions of the parabolic trajectory flight tests.

The apparatus was extensively tested under normal gravity. The acoustic field was characterized and the specific pressure node was selected for the acoustic levitation of

samples in microgravity. Theoretical estimates and experiments in normal gravity showed that the sample of about 1-3 mm diameter could be heated to desired temperatures of about 3000 K during the time available during one parabolic trajectory.

The experimental apparatus was built in accordance with the NASA safety requirements. Because of use of a 125 W CO_2 laser, many safeguards were developed and installed to prevent possible hazards for the experimentalists and the personnel of the aircraft. The analysis of the structural integrity of the setup was conducted and the apparatus was designed to satisfy the NASA 9-g load requirements.

The microgravity experiments were conducted onboard the NASA KC-135 aircraft flown from Houston, TX in February 2004. It was observed that the vertical position of the levitated sample was well maintained by the uniaxial acoustic field during its laser heating to about 3000 K. The levitated samples could be continuously laser heated for about 1 sec that resulted in a local sample melting. However, oscillations of the levitated samples in the horizontal direction were significantly greater in microgravity than they were in normal gravity. These oscillations further increased during sample heating and eventually resulted in moving the sample away from the stable levitation position and the laser beam. The vertical stability of the sample in microgravity showed for the first time that the acoustic field combined with microgravity environment can stabilize the sample position in a wide range of sample temperatures. At the same time, it was suggested that an effort aimed at the stabilization of the sample's horizontal position is necessary for successful containerless processing of high temperature molten samples in microgravity.

Follow-up on-ground experiments addressing the phase relations in the ternary Zr-O-N system were conducted. Samples of selected compositions prepared from Zr-ZrO_2-ZrN powders mixture were supported on a ceramic holder, laser-heated above the melting point, and cooled in the argon. The SEM and EDX analyses of the obtained samples were conducted. This study pointed to the location of the ternary invariant point L + G + ZrO_2 + ZrN on the high-temperature portion of the phase diagram. Comparisons of the results obtained in this work and composition histories of the zirconium particles burning in air reported earlier enabled us to further constrain the ternary liquidus in the Zr-O-N system. Elemental analyses of the nitrogen-rich inclusions found in the samples showed existence of an extended compositional range for the ternary solid Zr-O-N solutions. X-ray diffraction analysis of the quenched samples indicated that these solutions are likely to be derived from the ZrN phase. A preliminary outline of the subsolidus ternary Zr-ZrO_2-ZrN phase diagram is constructed based on these findings and the interpretations of the well-known binary Zr-O and Zr-N phase diagrams.

As a result of investigation conducted and described in this dissertation, the following future studies could be proposed. To study the effect of gravity on position and stability of a sample, experiments on levitation at various gravity levels in the range from normal gravity to zero-g could be conducted. Since the sample oscillations and stability depend also on the sample mass, samples of different sizes and densities should be used in these experiment. The sample levitation needs be enhanced by optimizing the reflector curvature. Therefore, reflectors with various curvature radii should be used in these studies. As a result of these studies, the effects of gravity, sample size (at a fixed density)

and sample density (at a fixed size) on the oscillation amplitudes and sample stability would be obtained and the optimized curvature would be selected and recommended for the future experiments with containerless heating. The proposed above modifications do not address the potential positioning errors in each experiment that could be caused by small residual accelerations, or small pressure differences. Therefore, another useful modification of the setup would be the possibility to adjust the laser beam (and the mirror position) to the current sample position in which the stable sample levitation during the flight is achieved.

In future normal gravity studies of Zr-O-N phases, the experiments with sample heating and rapid quenching should be developed. For example, splat-quenching using the same mechanism or similar to that developed for these microgravity experiments can be used. Experiments in inert atmosphere with some amount of nitrogen gas would decrease the amount of nitrogen release, observed in our experiments, and allow extending the range of Zr-O-N composition that can be studied.

APPENDIX A

STRUCTURAL ANALYSIS

A.1 Introduction

The equipment designed for the flight onboard KC-135 must comply with the NASA structural design requirements. In particular, it must withstand the g-loads during takeoff and landing as shown in Table A.1.

Table A.1 G-load specifications of the equipment.

Direction	Load Factor
Forward	9g
Aft	3g
Lateral	2g
Up	2g
Down	6g

The structural analysis for the proposed experiment was performed separately for three main units used in the experiment: the sample positioning system, the control unit and the coolant tank support frame. The laser is mounted directly to the base plate and the aircraft floor and needs no stress analysis. The control unit is built within a metal frame supplied by NASA and used previously for the microgravity tests onboard a DC-9 aircraft. Therefore, in the structural analysis reported here, only the effect of the specific configuration of the equipment mounted in this frame for our experiments is considered.

The contents of this appendix is a part of the Test Equipment Data Package, submitted to NASA prior to flight that addresses the structural integrity of in-flight equipment. The structural analysis was conducted in accordance with the requirements of the KC-135 User's Guide and the Glenn Research Center Safety Manual. Acceptable performance is indicated by positive margins of safety. The calculation of the margin of safety with respect to the material ultimate strength includes an additional safety factor of 1.5.
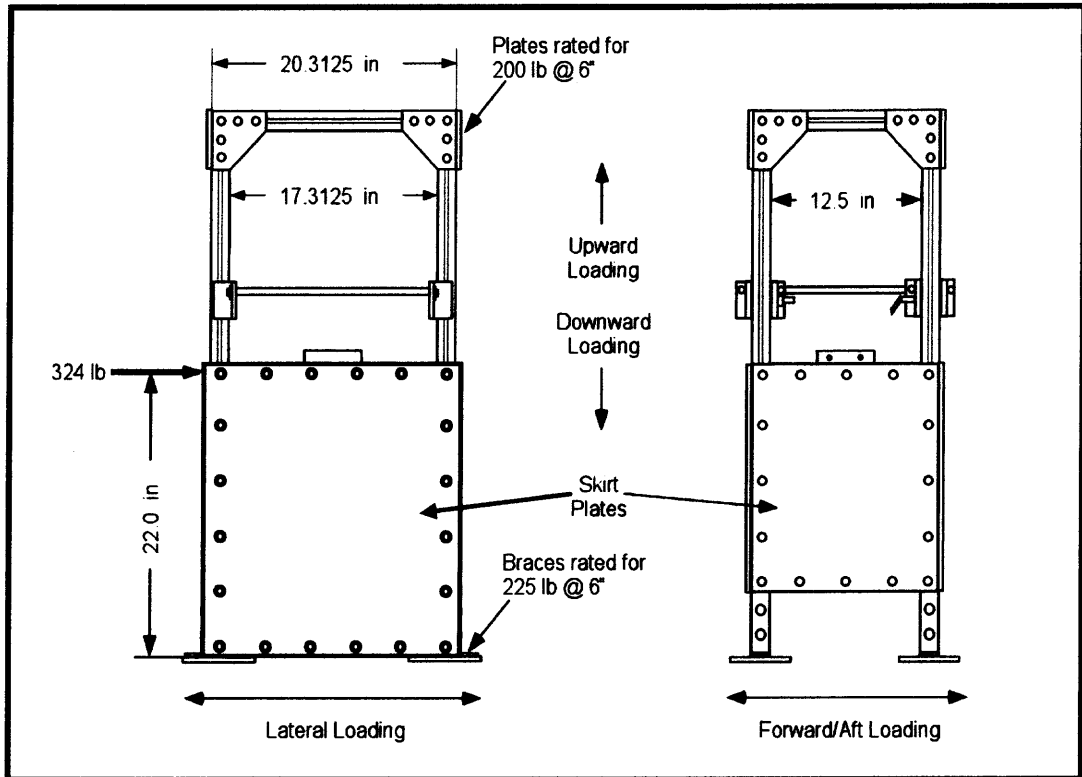
A.2 Sample Positioning System

The sample positioning system is constructed of the commercially available (80/20 Inc.) 6105-T5 aluminum T-slotted structural 1.5" square frame. A schematic diagram of the system is shown in Figure A.1 along with the directions of the loads analyzed as described below.

A.2.1 9g Forward and Aft Loading

A sketch of the preferred position of the Sample Positioning System in the airplane is shown in Figure A.2. The unit readily fits within the experimental lab space on the airplane and room is available in front of the apparatus for the experimentalists running the tests. A photograph of the Sample Positioning System together with a simplified model used in this analysis (see below) are shown in Figure A.3.

The maximum allowable loads per bolt are 600 Lb across the T-slot and 125 Lb in the direction of the T-slot. These loads are based on the supplier (80/20 Inc.) specified T-slot limitations and not the bolt limitations. Each bolt is a grade 8 and has $^5/_{16}$" diameter.

The allowable loads for the T-slots represent a small fraction of the allowable bolt tensile and shear stresses.

Figure A.1 Schematic diagram of the sample positioning system designed and constructed at NJIT. The skirt plates on the right are added to withstand the forward/aft loading of the setup. The skirt plates on the left are added to enable the rotation of the apparatus so that 9g "lateral loading" could be withstood as well.

The ability of the main aluminum frame to withstand a horizontal acceleration of 9g (the most challenging load for this construction) was evaluated using the material properties provided by the manufacturer and a simplified model described below. The model simulates the structural integrity of the aluminum frame construction shown in Figure A.1.

WING STATIONS (IN)
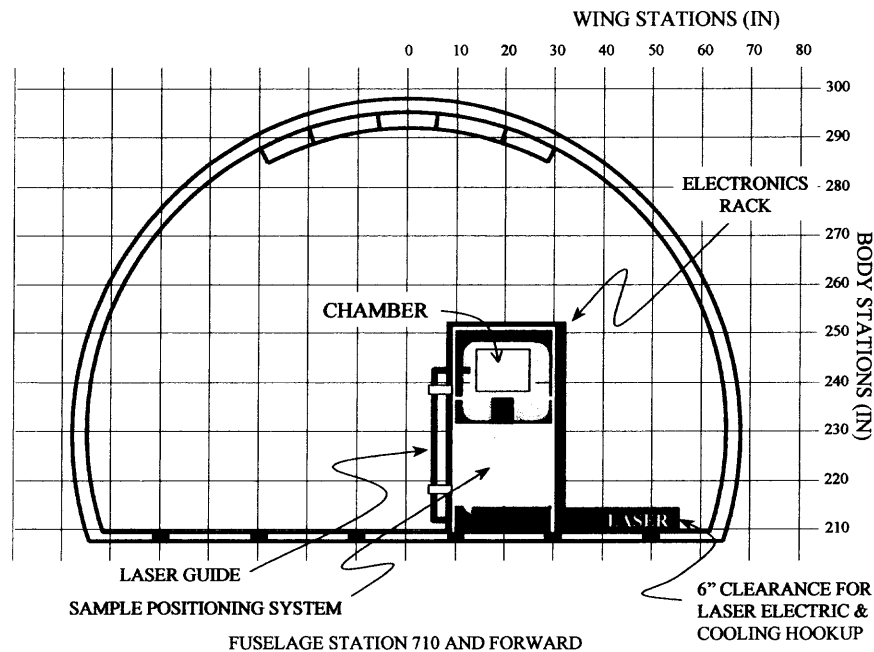
Figure A.2 Sketch of the sample positioning system in the airplane.

The ¼'' thick aluminum skirt plates around the perimeter of the frame are added to withstand the forward/aft loads and to enable the rotation of the apparatus so that the 9g "lateral loading" could be withstood as well.

The schematic diagram of the model used in calculations is shown in the inset of Figure A.3. The structural integrity of the components built of the T-slotted aluminum frame was initially evaluated using a 3-point force diagram shown in Figure A.3. The dimensions of the frame used in the computations are:

Total height: 42"

The height of the acoustic actuator mount: 22"

The height of the processing chamber mount: 27.5"

Respective inertia forces, including those caused by the mounts of the processing chamber, acoustic actuator, and the frame itself are shown. The inertia force caused by

the frame is distributed over the length of the frame, but for a conservative estimate it is applied as a single point force, as shown in the diagram. Because the frame is built of four equivalent posts, the bending moment per single post is estimated as 1/4 of the moment produced by the total mass load. This estimate neglects the reinforcing effect of the horizontal members used in the frame construction:

$$M = 1/4 \cdot (35lb \cdot 21in + 15.5lb \cdot 22in + 47.3lb \cdot 27.5in) = 2376.8 \ lb\text{-}in \qquad (A.1)$$

The model was further simplified (which led to an even more conservative estimate) whereas the three-point load was replaced with the one-point load with the same total mass. It was estimated that a total mass of 97.8 lb plus a 10% fudge factor, a total of 108 lb spread over the four posts, was to be applied to a 24.3 in arm in order to produce the same total bending moment. At 9 g, each post therefore would be loaded with 108 lb/4·9 = 243 lb. The area moment of inertia of a post was estimated as $I = 0.249$ in^4. The distance from the neutral axis, $c = 0.75$ in, so that the maximum stress developed in the T-slot extrusion is estimated as:

$$\sigma = (243 \ lb \cdot 24.3 \ in \cdot 0.75 \ in)/0.249 \ in^4 = 17786 \ psi \qquad (A.2)$$

The margins of safety are:

$$MS_{UT} = \frac{42000psi}{1.5(17786psi)} - 1 = .57 \qquad MS_{TY} = \frac{35000psi}{17786psi} - 1 = 0.96 \qquad (A.3)$$

Therefore, the vertical 42" long T-slot posts are not subject to significant deflection under load.

There are 3 types of joints in question:

1). Skirt plates (shown in Figure A.1 but not shown in photo Figure A.3; treated as bolted joints)

2). Post feet (braces in Figure A.1)
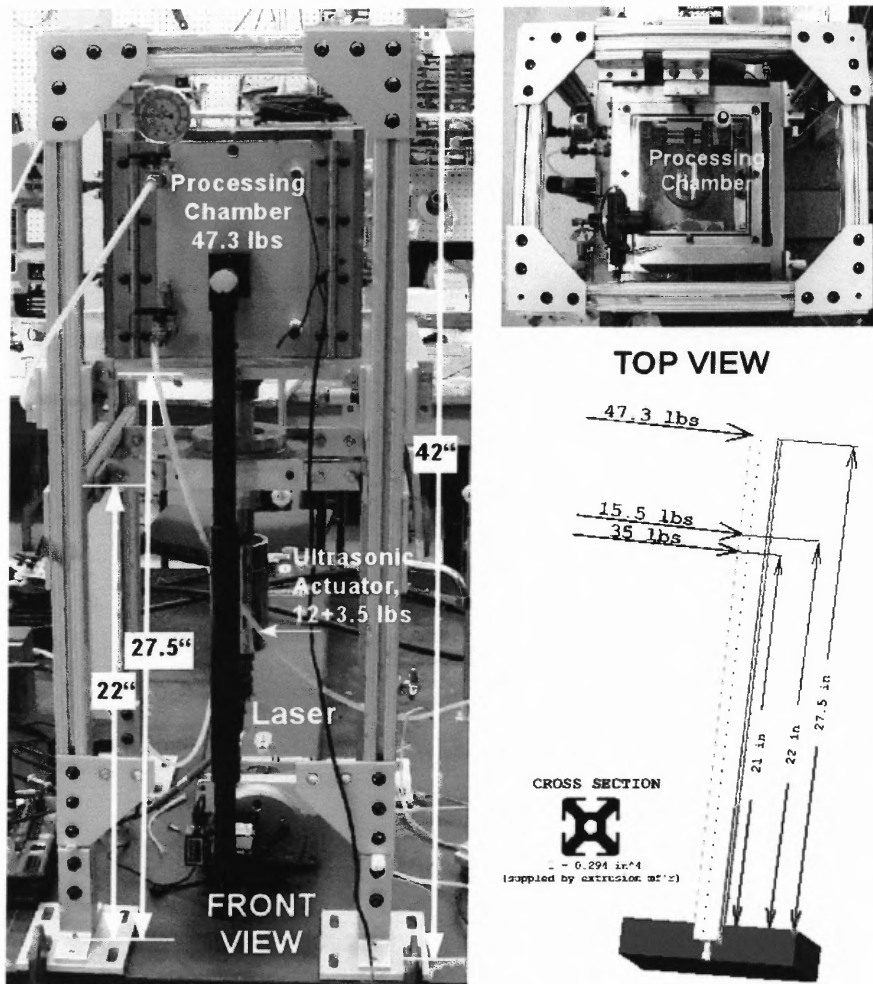
Figure A.3 Front and top views of the sample positioning system (skirt plates removed) and a simplified model used for estimates.

3). Cantilever plate joints (on top of the frame)

It was determined that the greatest rotational moment is concentrated in the ¼" thick aluminum skirt plates, the main reinforcing component of the rack. The following diagram (Figure A.4) shows the skirt plate details used in the estimates below. From the symmetry considerations, the center of gravity (C.G.) is located at the center of the plate.

The load R on any bolt is found from

$$R = \frac{M \cdot l}{J} \qquad \text{(A.4)}$$

where M is the moment of the mass load under the given acceleration, r is the distance

from the bolt to the C.G., and J is respective moment of inertia. The moment of the load

under 9g acceleration is spread over 2 skirt plates, so that the moment on each skirt is:

$$M = \frac{9gPl_{sp}}{2} \qquad (A.5)$$

where $P = 108$ lb, is the normal gravity mass load, $l_{sp} = 10.8$", is the distance between the

C.G. of the plate and the C.G. of the rig.

$$M = \frac{108lb \cdot 10.8in \cdot 9g}{2} = 5250lb - in \qquad (A.6)$$

The moment of inertia is:

$$J = \left(7.00^2 + 2 \times 8.06^2 in^2 + 2 \times 10.63^2 in^2 + 2 \times 8.73^2 in^2 + 8.00^2 in^2\right) \times 2 = 1240in^2 \qquad (A.7)$$

The respective maximum horizontal and vertical component loads are:

$$R_x = \frac{5250lb - in \cdot 8in}{1240in^2} = 33.8lb \qquad (A.8)$$

$$R_y = \frac{5250lb - in \cdot 7in}{1240in} = 29.6lb \qquad (A.9)$$

The T-slot runs in the y direction (cf. Figure 10). The allowable load in the y

direction is 125lb, and the margin of safety in the y direction is:

$$MS = \frac{125lb}{29.6lb} - 1 = 3.2 \qquad (A.10)$$

The allowable load in the x direction is 600lb, and the margin of safety in the x

direction is:.

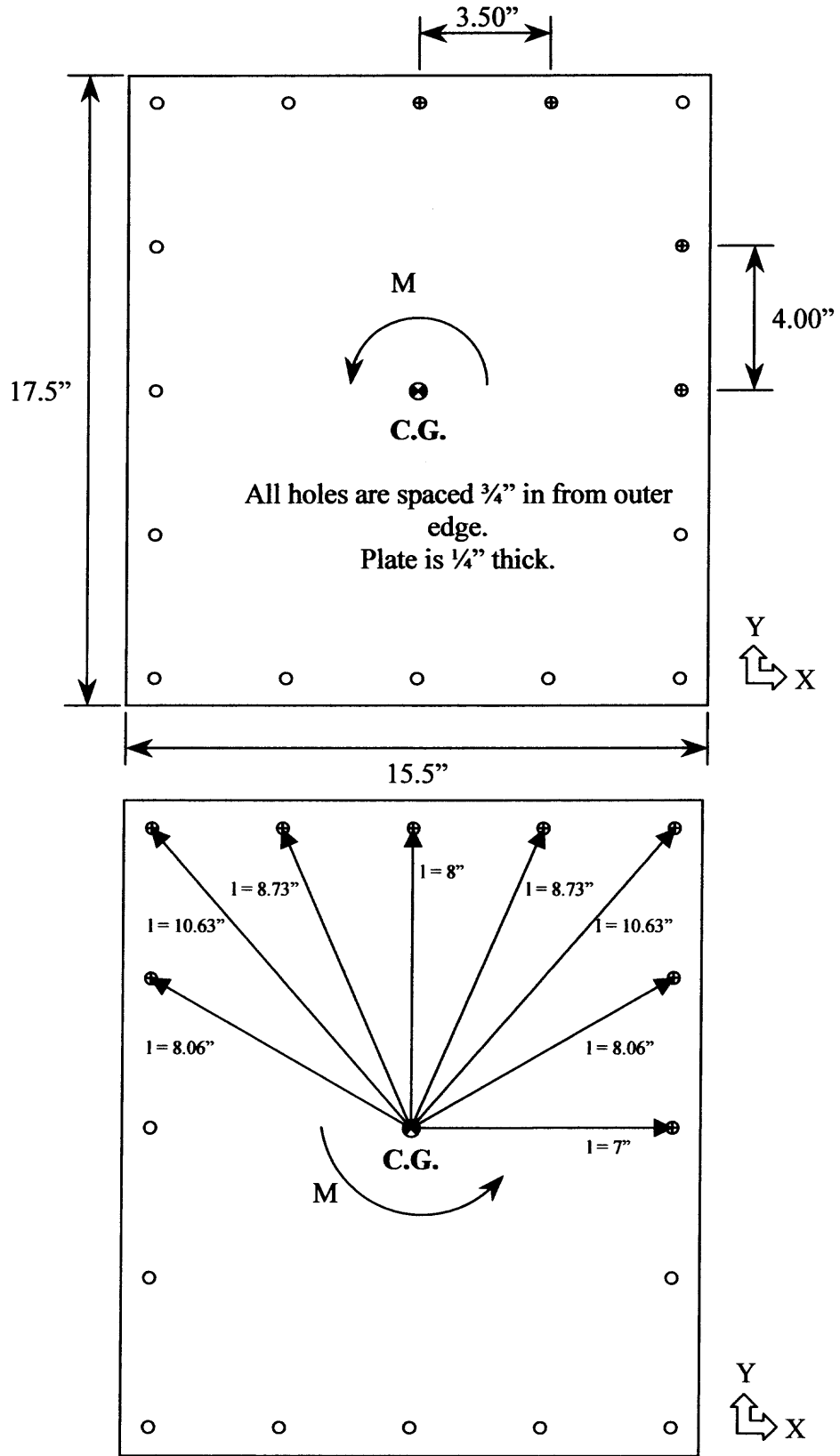$$MS = \frac{600lb}{33.8lb} - 1 = 16.8 \qquad (A.11)$$

Figure A.4 Diagram of small skirt plates used to reinforce the rig at aft/forward loadings

A.2.2 9g Lateral Loading

This computation is made to replace the required analysis for the 2g lateral loading to enable experimentalists to reorient the apparatus within the airplane should it be desired.

It was noted earlier that the greatest rotational moment is concentrated in the ¼" thick aluminum skirt plates. The diagram in Figure A.5 shows the lateral skirt plate details (similar to the discussed above, but with slightly different dimensions). By symmetry the C.G. is located in the center of the plate. The load on any bolt is found again from (A.4), (A.5),using the distance between the C.G. of the plate and the C.G. of the rig $l_{sp} = 13.2$":

$$M = \frac{108lb \cdot 13.2in \cdot 9g}{2} = 6420lb - in \tag{A.12}$$

The moment of inertia:

$$J = \left(10.6^2 in^2 + 11.8^2 in^2 + 14.1^2 in^2 + 11.3^2 in^2 + 9.70^2 in^2\right) \cdot 4 = 2690in^2 \tag{A.13}$$

The respective maximum horizontal and vertical component loads are:

$$R_x = \frac{6420lb - in \cdot 10.5in}{2690in^2} = 25.1lb \tag{A.14}$$

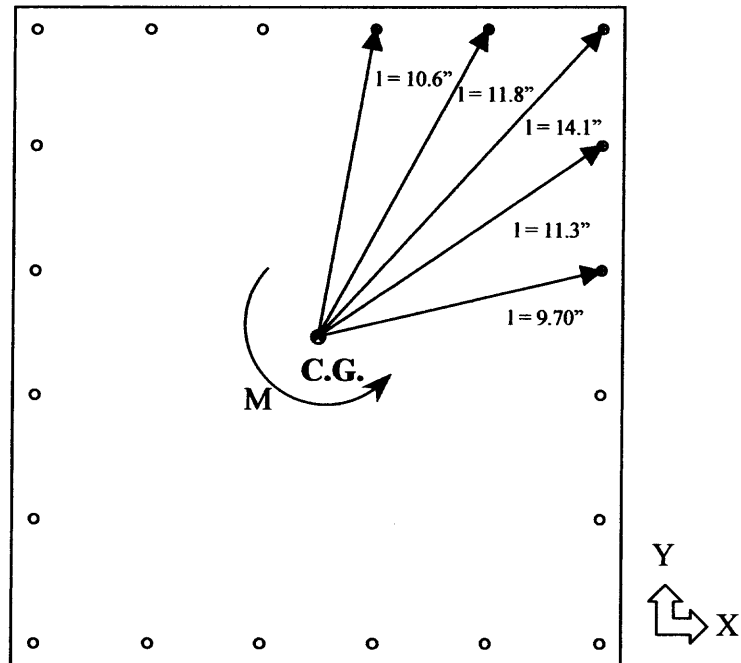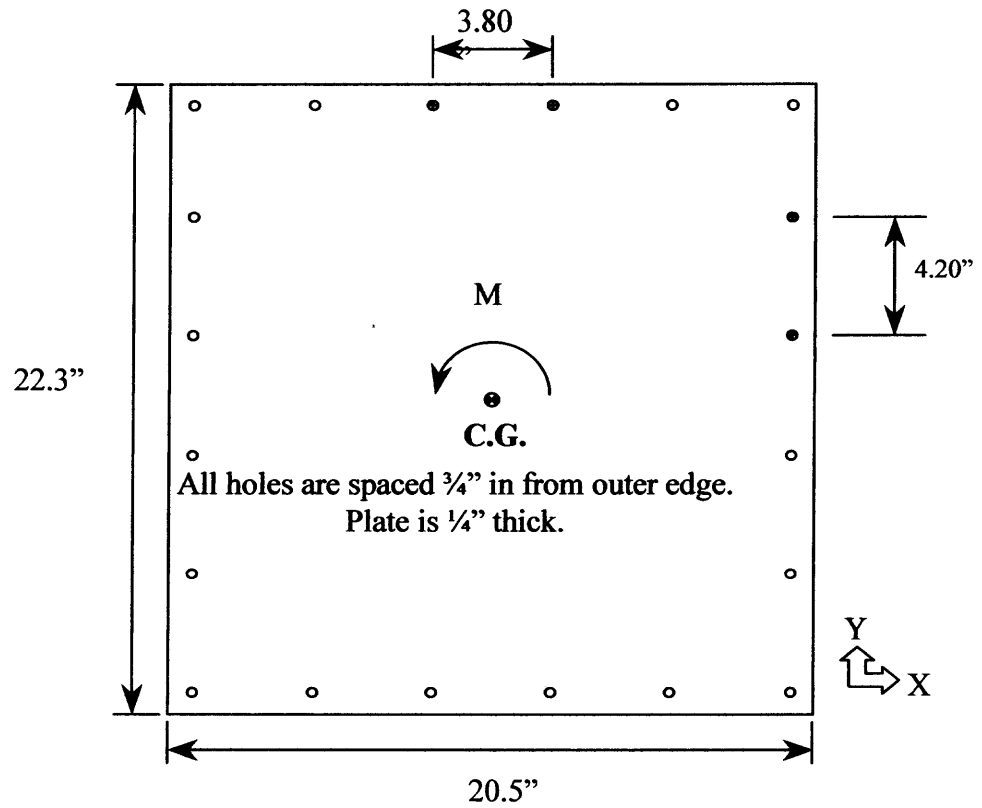$$R_y = \frac{6420lb - in \cdot 9.5in}{2690in} = 22.7lb \tag{A.15}$$

The margins of safety are

$$MS = \frac{125lb}{22.7lb} - 1 = 4.5 \tag{A.16}$$

in the y direction, and

$$MS = \frac{600lb}{25.1lb} - 1 = 22.9 \tag{A.17}$$

in the x direction.

Figure A.5 Diagram of large skirt plates used to reinforce rig at lateral loadings

A.2.3 Chamber. 6g Downward & 2g Upward Loadings

If the 6g downward loading criteria is met, then the 2g upward loading is also met, therefore only the 6g downward loading will be addressed below. The exception is the mounting of the feet to the frame rails, which is considered separately.

The chamber is mounted to a base plate. The mass of the chamber and base plate is 47.3lb.

At 6g this load is:

$$P = 6g \cdot 47.3lb = 283.8lb \tag{A.18}$$

The base plate is fastened to 4 lineal bearings via 8 grade 8 $^5/_{16}$-18 bolts. The load distribution per bolt is:

$$R = \frac{283.8}{8} lb = 35.48lb \tag{A.19}$$

Maximum allowable shearing load for a $^5/_{16}$-18 grade 8 bolt is 4265lb. Therefore, the load per bolt is less than the allowable load by over 2 orders of magnitude.

This load is transferred to the linear bearings. Each bearing is held in place with a brake, which has an allowable load rating of 125lb.

$$R = \frac{283.8}{4} lb = 70.95lb \tag{A.20}$$

The margin of safety:

$$MS = \frac{125lbs}{70.95lbs} - 1 = 0.76 \tag{A.21}$$

A.2.4 Horn/Booster Mount. 6g Downward & 2g Upward Loadings

The central mounting plate is bolted via 4 ¼-20 screws to 2 cross plates, which are then bolted to the frame members via 4 corner brackets.

The horn and mount weigh 15lb in total. The load is spread among 4 brackets, so the load per bracket is

$$R = \frac{6g \cdot 15lb}{4} = 22.5 \qquad (A22)$$

The allowable lateral load on each bracket is 600lb. The margin of safety is:

$$MS = \frac{600lb}{22.5lb} - 1 = 25.7 \qquad (A.23)$$

Two horizontal aluminum bars mount the holder to the brackets via 2 $^5/_{16}$-18 grade 8 bolts at each bracket. Earlier it was established that the allowable shear load on each of these bolts is 4265lb, so the total allowable load is 8530lb, higher than 2 orders of magnitude above the maximum load.

Lastly, the mount itself is bolted to the two horizontal aluminum bars via 4 ¼-20 grade 8 screws. The maximum shear load for each screw is 2730lb. The total allowable load for the 4 screws is then 109204b, over120 times greater than the maximum load requirement.

A.2.5 Frame Feet

This connection must be checked for the 2g upward load. The weight of the frame under 2g is 216 lb.

There are 2 corner brackets holding each leg to each foot. Since there are 4 legs, there are 8 brackets connecting the frame to the feet. The manufacturer's load rating under direct loading, as is the case here, is 250lb per bracket. The total allowable load then is:

$$P = 250lb \cdot 8 = 2000lb \qquad (A.24)$$

The margin of safety is given by the ratio of the allowable load to the actual load:

$$MS = \frac{2000lb}{216lb} - 1 = 8.26 \qquad (A.25)$$

A.2.6 9g Loading on Aircraft Attachment Points

The total weight of the frame including all mounted apparatus at 9g distributed over the 2 sides of the frame. The load on each side is

$$R = \frac{9g \cdot 108lb}{2} = 486lb \qquad (A.26)$$

The turning moment of the frame under the same conditions for each side of the frame:

$$M = \frac{108lb \cdot 22in \cdot 9g}{2} = 10692lb - in \qquad (A.27)$$

The attachment points span 20 in. The vertical load per attachment point is:

$$R_T = \frac{10692lb - in}{20in} = 534.6lb \qquad (A.28)$$

The horizontal load per attachment point is calculated as:

$$Rs = \frac{W}{2} = \frac{486lb}{2} = 243lb \qquad (A.29)$$

The tensile and shear yield strengths of the attachment point are 5000 lb.

The tensile and shear margins of safety are given by:

$$MS_{YT} = \frac{5000lb}{534.6lb} - 1 = 8.35 \qquad MS_{YS} = \frac{5000lb}{243lb} - 1 = 19.6 \qquad (A.30)$$

A.3 Control Unit

This unit is built based on a Vertical Equipment Rack (Bare Rack and Shelves supplied by NASA.). A diagram of the Control Unit is shown in Figure A.6. A Laptop computer

is mounted on the top of the rack using a 1/8th inch thick aluminum base plate. The computer is stowed in a bag during take-off and landing and is installed for experiments only during the flight.
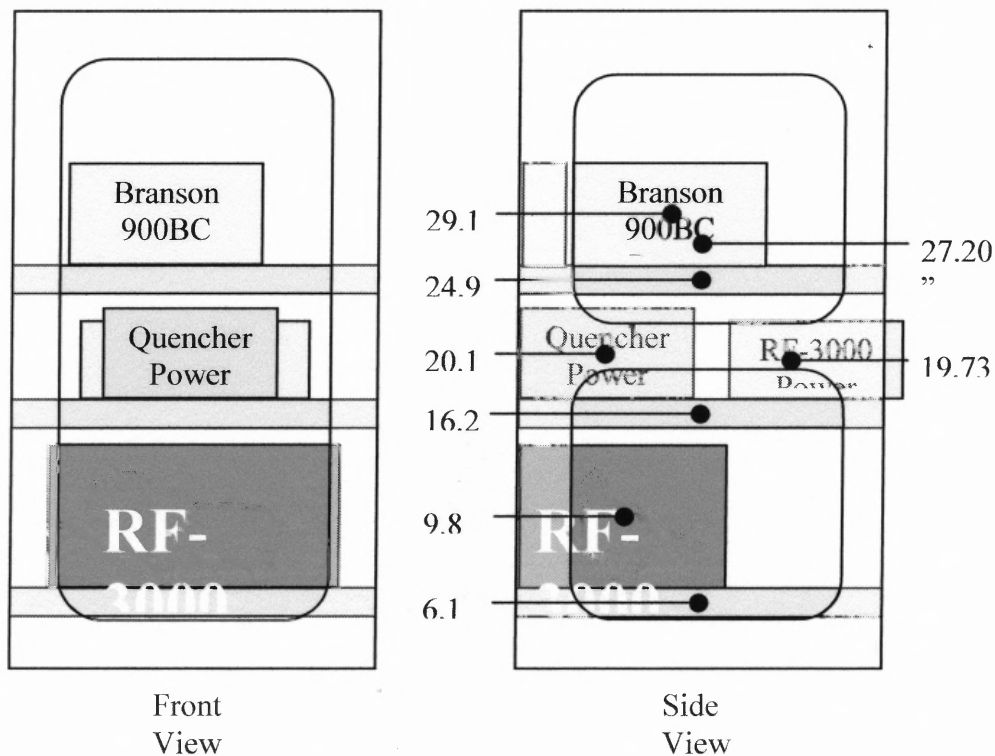
Figure A.6 Diagram of the configured Control Unit built in a NASA supplied Vertical Equipment

Total turning moment:

$$M = 7.50 lb \cdot 6.19 in + 36 lb \cdot 9.80 in + 7.5 lb \cdot 16.3 in + 21 lb \cdot 19.7 in +$$
$$+20 lb \cdot 20.1 in + 7.5 \ lb \cdot 24.9 in + 39 lb \cdot 27.2 in + 36 lb \cdot 29.1 in +$$ (A.31)
$$+7.1 lb \cdot 42 in + 7.0 lb \cdot 43 in = 4240 lb - in$$

This value is well within the allowable limit of 6130 lb-in as long as the rack is oriented so that the open face of the rack is facing laterally, i.e. not with the axis of the

aircraft. Therefore, this is the orientation the rack will be mounted for experiments.

The shelves in similar racks are typically installed with M5 AN machine screws. They have strength ratings nominally equivalent to Grade 5. We used screws of a higher Grade 8 (nominally 33% stronger than Grade 5) due to the lack of availability of the typical screws through our supplier, McMaster-Carr.

A.4 Process Chamber Structural Strength Analysis

The chamber is constructed as a cube nominally 10" on a side. The largest flat area exposed to internal pressure is 8"X8" (the doors).

The chamber consists of an internal frame constructed of the 6061-T6 aluminum covered with either aluminum or Lexan® sides.

Four sides have fixed plates, 2 Lexan® and 2 6061-T6 aluminum. All plates are ½" thick. The remaining 2 sides are doors made of 1" x 1 ½" 6061-T6 bar stock with ½" thick Lexan® windows. The doors are hinged by a heavy piano hinge and are held closed by 2 cam-over toggle clamps on the opposing edge (from the hinges) of each door. The doors and all plates are sealed via an o-ring.

The chamber is expected to run at a maximum differential pressure of 5 psid (taking into account a possible cabin depressurization). The box frame and door frames are de-rated to 6061-0 strength since the frames are all welded together and were not re-tempered; however they were water quenched so their strength is expected to be much greater than that for 6061-0.

The chamber has been pressure and vacuum tested and certified.

A.4.1 Box Frame

The largest areas exposed to internal pressure of the chamber are the 8"x8" sections of the door windows defined by the window O-rings. This load is applied to the box frame through the door hinge and the door toggle clamps. The box frame is constructed of 1" square 6061-T6 aluminum bars welded together.

The yield strength for 6061-0 aluminum is 7980 psi. With 4 in^2 available to resist the load:

$$P = 4.00 \ in^2 \cdot 7980 psi \ = \ 31,920 lb \tag{A.32}$$

Maximum chamber pressure based on this load is:

$$p = \frac{31920 lb}{64 in^2} = 499 psi \tag{A.33}$$

This is nearly 100x higher than the pressure at which the chamber will be operated.

## A.5 Coolant Tank/Pump Support Frame

The coolant system includes a centrifugal pump to circulate the cooling water and an accumulator to minimize the pressure rise associated with an increase in temperature, as well as a guard frame assembly to protect the accumulator and prevent contact between personnel and components of the coolant system (Figure A.7). Note that the assembly includes the installation of panels to retain the volume of water in the coolant tank. For clarity, these panels are not shown in many of the figures of the following paragraphs.

FOR CLARITY, INTERCONNECT
HOSES NOT SHOWN.

GUARD FRAME

38.00

ACCUMULATOR

COOLANT TANK

PUMP

22.00

29.00
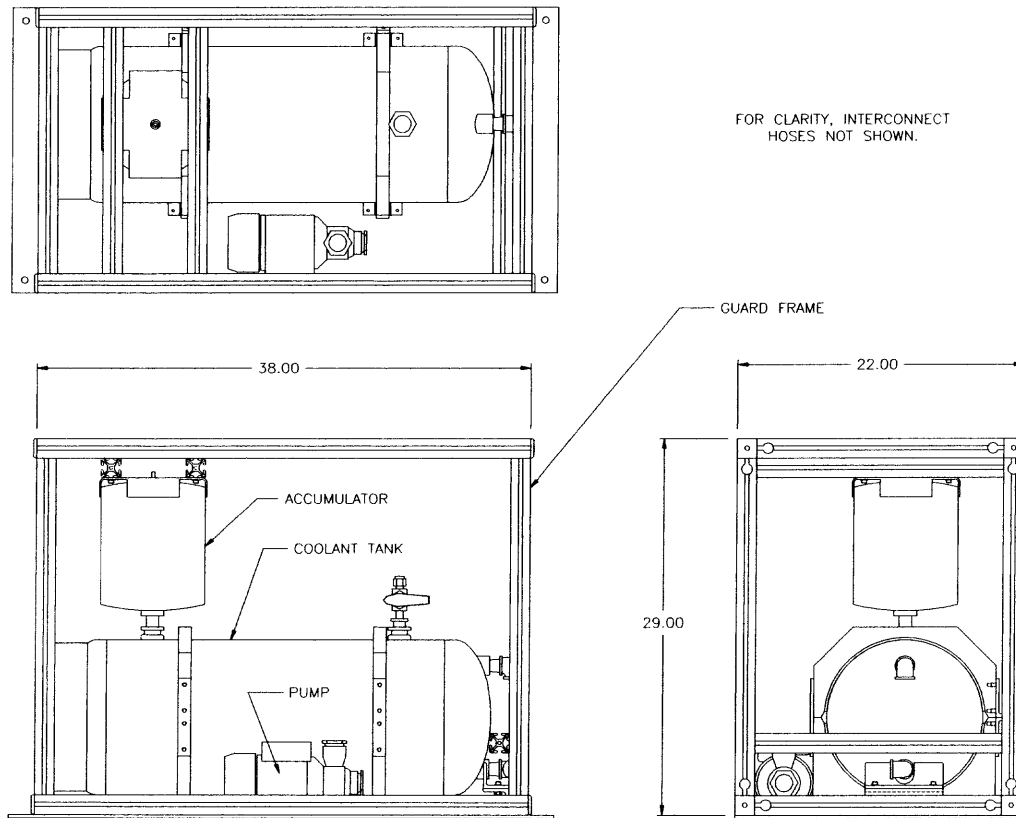
Figure A.7 Coolant tank assembly.

A.5.1 Accumulator Restraint

The accumulator is installed to the top of the coolant tank by means of a single pipe
fitting. When subjected to load factors in the horizontal plane, the accumulator tends to
rotate about the pipe fitting in a way that induces bending in the material of the shell
surrounding the pipe fitting. In order to eliminate these bending loads, a support
assembly has been installed to support the top of the accumulator (Figure A.8).
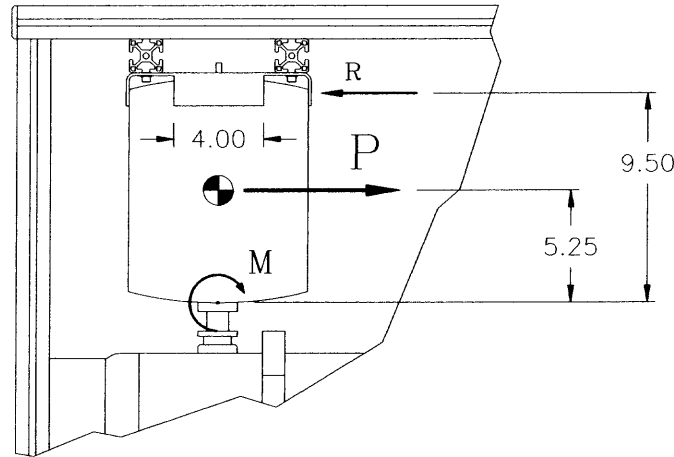
Figure A.8 Accumulator supports.

The weight of the accumulator is estimated at 3.0 lb, and when subject to the 9g forward load factor, the applied load P is 27 lb. Assuming, conservatively, that the material of the accumulator shell near the pipe fitting contributes no resistance to the applied moment, then the reaction R at the support is computed as:

$$\sum M = 0 = (27lb)(5.25in) - R(9.50in)$$

$$R = \frac{(27lb)(5.25in)}{9.50in} = 14.9lb \tag{A.34}$$

This reaction is applied to the support assembly as a bending load acting on one tab of the retaining bracket (Figure A.8). The retaining bracket is fabricated from .13 in. thick 6061-T6 Aluminum alloy plate. The maximum moment in the bracket occurs at the base of the bend in the bracket, 1.25 in. from the point of application. The bending stress developed in the bracket is calculated as:

$$\sigma = \frac{Mc}{I}$$

$$M = R(1.25in) = (14.9lb)(1.25in) = 18.7lb - in$$

$$I = \frac{4.00in}{12}(.13in)^3 = 7.32 * 10^{-4} in^4$$

(A.35)

$$\sigma = \frac{(18.7lb - in)(.063in)}{7.32 * 10^{-4} in^4} = 1610psi$$

This applied stress is one order of magnitude less than the strength value for the material of the bracket, suggesting large margins against failure in all modes.

The reaction R is transferred to the frame assembly through two cross-beams connected to the frame assembly. As this reaction is assumed to be equally supported by the two cross-beams, the load acting on each cross-beam is 7.5 lb., and structural failure in these components is not expected.

A.5.2 Coolant Tank Supports

The coolant tank is restrained by several mechanisms, as illustrated in Figure A.9.
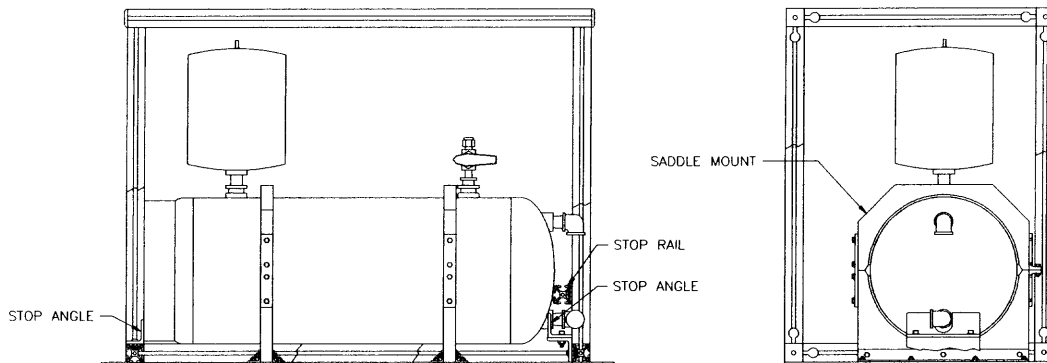
Figure A.9 Coolant tank restraints.

When the load factor is applied parallel to the long axis of the coolant tank, the tank is restrained by the either the single stop angle (at the left side in the figure) or the combination of the stop angle and stop rail (at the right side in the figure). This ignores, conservatively, the contribution of the saddle mount system to restraint along this axis (any contribution would be a result of the friction force exerted on the tank by the vinyl/nitrile elastomer gap seal of the saddle mount. The flexibility of this material would render the reaction force small in comparison to the reaction at the stops.). If it is assumed that the load factor acts to the left in Figure A.9, then translation of the tank is resisted solely by one stop angle, and the reactions are as illustrated in Figure A.10. The ring at the end of the tank provides a contact surface between the tank and the stop angle, the geometry of this contact is such that the load is applied to the angle in the plane of the horizontal leg, effectively eliminating any bending moments on the angle.
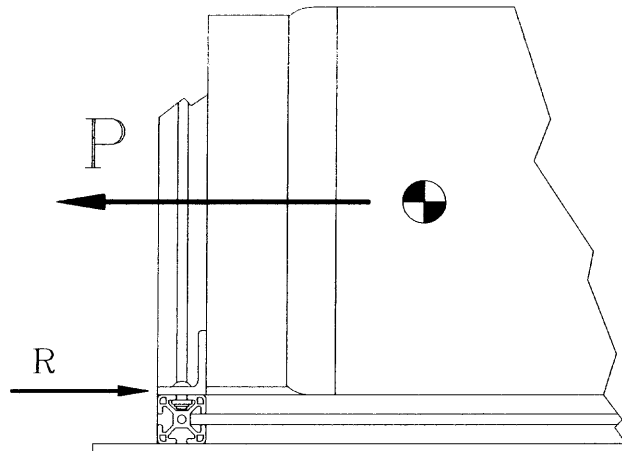
Figure A.10 Load on the stop angle. The ring end.

The stop angle is attached to the base frame component using three ¼-28 socket head cap screws, and the critical failure mode is shear failure in these screws. Assuming application of the 9g forward load factor, the shear load acting on any of these screws is

computed as:

$$R_S = \frac{P}{3} = \frac{9g \cdot 188.3lb}{3} = 565lb \qquad (A.36)$$

Because these screws are relatively short, they are threaded for the full length and the determination of the applied stress is calculated on the basis of the thread minor diameter as:

$$\tau = \frac{R_S}{A} = \frac{565lb}{0.25d^2\pi} = \frac{565lb}{0.0326in^2} = 17331psi \qquad (A.37)$$

The shear strength of socket head cap screws is given as 90 *ksi*. Comparing the applied stress to the material strength yields:

$$MS_{US} = \frac{90ksi}{1.5 \cdot 17331psi} - 1 = 2.5 \qquad (A.38)$$

This same shear load is exerted on the stop angle as a bearing load, for which the bearing stress is determined as:

$$\sigma_{BR} = \frac{R_S}{A} = \frac{565lb}{(0.25in)^2} = 9040psi \qquad (A.39)$$

The bearing strengths of the 6061-T6 Aluminum alloy angle are obtained as $S_{BRU} = 88000$ psi and $S_{BRY} = 58000$ psi.

Comparing the applied stress to the material strengths:

$$MS_{UBR} = \frac{88ksi}{1.5 \cdot 9040psi} - 1 = 5.5 \qquad MS_{YBR} = \frac{58ksi}{9040psi} - 1 = 5.4 \qquad (A.40)$$

If it is assumed that the load factor acts to the right in Figure A.10, then translation of the tank is resisted one stop angle and a stop rail, and the reactions are as illustrated in Figure A.11.

In order to determine the applied stress in either the stop angle or the stop rail, it is

necessary to determine the share of the load carried by each member. This can be approximated reasonably well on the basis of the relative flexibility of each member, obtained as the effective spring rate of the members. Using standard beam deflection relationships and applying these relationships to Hooke's law, the spring rate of the stop angle (assumed to react as a cantilever beam) and the stop rail (assumed to react as a beam on fixed supports) are computed. Width of each of the two "tabs" of the stop angle (on either side of the cut-out for the pipe fitting) is obtained as 2.25 in., and the thickness of the angle is .25 in.

$$I_{Angle} = \frac{2 \cdot 0.25in}{12} \cdot (0.25in)^3 = 5.86 \cdot 10^{-3} in^4$$

$$I_{Rail} = .1853in^4$$

$$k_{Angle} = \frac{3EI}{l^3} = \frac{3 \cdot 10^7 psi \cdot 5.86 \cdot 10^{-3} in^4}{(1.75in)^3} = 32800 lb/in \qquad (A.41)$$

$$k_{Rail} = \frac{192EI}{l^3} = \frac{192 \cdot 1.2 * 10^7 psi \cdot 0.1853in^4}{(19.0in)^3} = 52910 lb/in$$
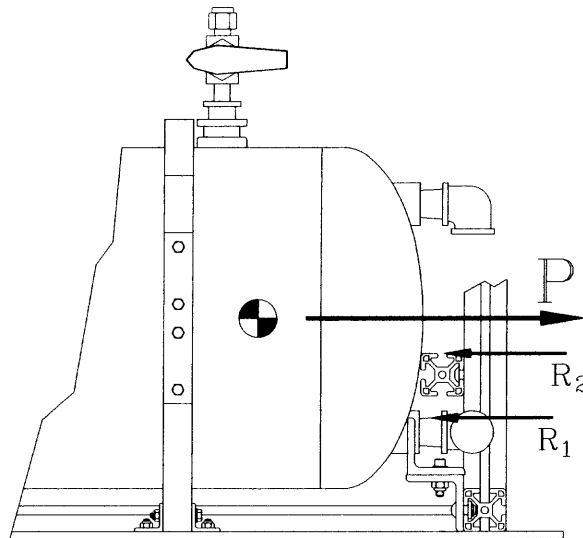
Figure A.11 Loads on the stop angle. The stop rail.

When the coolant tank begins to move under the influence of external loads, the two stops react to resist this movement. Based on the effective spring rates just computed, the proportion, c_i, of the load carried by each stop is determined:

$$c_{Angle} = \frac{k_{Angle}}{k_{Angle} + k_{Rail}} = \frac{32800lb/in}{32800lb/in + 52910lb/in} = .38$$

$$c_{Rail} = 1 - c_{Angle} = .62$$

(A.42)

When the coolant tank is subject to the 9g forward load factor, the stops react in these proportions, and the actual loads on each stop are determined as:

$$R_{Angle} = 0.38P = 0.38 \cdot 9g \cdot 188.3lb = 644lb$$

$$R_{Rail} = 0.62P = 0.62 \cdot 9g \cdot 188.3lb = 1050lb$$

(A.43)

The bending stress developed in the stop angle is computed as:

$$\sigma = \frac{Mc}{I}$$

$$M = R_{Angle} \cdot 1.75in = 644lb \cdot 1.75in = 1127lb - in$$

$$\sigma = \frac{1127lb - in \cdot 0.125in}{5.86 \cdot 10^{-3} in^4} = 24040 psi$$

(A.44)

Comparing this stress to the material strength of the 6061-T6 aluminum alloy angle:

$$MS_{UT} = \frac{42ksi}{1.5 \cdot 24040psi} - 1 = 0.16 \qquad MS_{YT} = \frac{35ksi}{24040psi} - 1 = 0.46$$

(A.45)

The stress bending developed in the stop rail is computed as:

$$\sigma = \frac{Mc}{I}$$

$$M = \frac{Pl}{8} = \frac{9g \cdot 188.3lb \cdot 19.0in}{8} = 4025lb - in$$

$$\sigma = \frac{4025lb - in \cdot 0.75in}{0.1853in^4} = 16290 psi$$

(A.46)

Comparing this stress to the material strength of the 6105-T5 aluminum alloy section:

$$MS_{UT} = \frac{38ksi}{1.5 \cdot 16290psi} - 1 = 0.56 \qquad MS_{YT} = \frac{35ksi}{16290psi} - 1 = 1.15 \qquad (A.47)$$

The two saddle mounts are fabricated from 1.0 in. thick 6061-T6 Aluminum alloy plate, and support the coolant tank in the vertical axis as well as the horizontal axis perpendicular to the long axis of the tank. Loads in the horizontal plane produce reactions as indicated in Figure A.12.
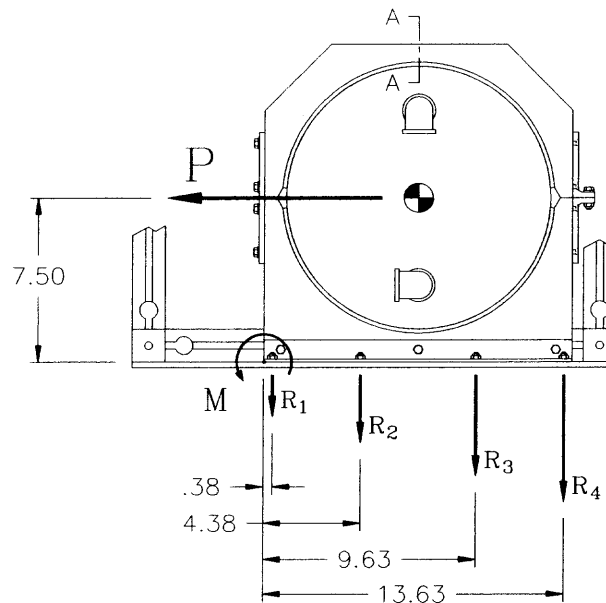
Figure A.12 Saddle mount loads. Reactions.

The applied load indicated in Figure A.12 produces an effective hoop stress in the saddle mount, which reaches a maximum value at the smallest cross section area, identified here as section A-A. The dimensions of the saddle mount at this section are 1.0 in. x .813 in. The reactions to the hoop stress are such that ½ of the load is reacted at section A-A, and the load is shared between the two saddle mounts, so that the total load

reacted at section A-A of the saddle mount is *P/4*. The tensile stress associated with this load is calculated as:

$$\sigma = \frac{P}{4A} = \frac{9g \cdot 188.3lb}{4 \cdot 1.0in \cdot 0.813in} = 520psi \qquad \text{(A.48)}$$

The resulting stress is two orders of magnitude less than the material strength of the saddle mount, suggesting large margins against failure in this mode.

The saddle mounts are each connected to the base plate by two angle brackets, with three AN3 (10-32) screws attaching the saddle mount to the angle bracket. These screws are installed on 6.25 in. centers, and react to the direct shear of the applied load as well as the applied overturn moment. The direct shear acting on any screw is determined as (3 screws at each of two angles, 6 screws total):

$$R_{S,direct} = \frac{P}{6} = \frac{9g \cdot 188.3lb}{6} = 282lb \qquad \text{(A.49)}$$

The shear load associated with the reaction to the overturn moment is computed as:

$$R_{S,overturn} = \frac{M}{4l} = \frac{9g \cdot 188.3lb \cdot 7.50in}{4 \cdot 6.25in} = 508lb \qquad \text{(A.50)}$$

Combining these two shear components:

$$R_S = \sqrt{R_{S,direct}^2 + R_{S,overturn}^2} = \sqrt{(282lb)^2 + (508lb)^2} = 581lb \qquad \text{(A.51)}$$

Comparing this load to the failure loads of the 10-32 screw (S_{US} = 2126 lb, S_{YS} = 1644 lb):

$$MS_{US} = \frac{2126lb}{1.5 \cdot 581lb} - 1 = 1.44 \qquad MS_{YS} = \frac{1644lb}{581lb} - 1 = 1.83 \qquad \text{(A.52)}$$

This analysis ignores, conservatively, that the screws are placed in double shear by the nature of the installation, which would have the effect of halving the shear loads. The shear load is reacted at the angle as a bearing stress, the magnitude of which is

determined as:

$$\sigma_{BR} = \frac{R_S}{A} = \frac{581lb}{0.19in \cdot 0.125in} = 24463psi \qquad (A.53)$$

Comparing the applied stress to the material strengths:

$$MS_{UBR} = \frac{88ksi}{1.5(24463psi)} - 1 = 1.4 \qquad MS_{YBR} = \frac{58ksi}{24463psi} - 1 = 1.4 \qquad (A.54)$$

Again, these results ignore, conservatively, that the screws are placed in double shear.

The direct shear and overturn moment acting on the coolant tank assembly produce shear and tensile loads in the screws attaching the angles to the base plate. The direct shear supported by each screw is computed by dividing the load into the 16 screws attaching the angles to the base, as:

$$R_{S,direct} = \frac{P}{16} = \frac{9g \cdot 188.3lb}{16} = 106lb \qquad (A.55)$$

The tensile load applied to the screws as a result of the overturn moment reaches a maximum in the screws farthest from the heeling line. The tensile load in one of the four screws at this location is computed:

$$R_T = \frac{Pld_k}{4\sum_i nd_i^2} = \frac{9g \cdot 188.3lb \cdot 7.50in \cdot 13.63in}{4 \cdot (0.38in^2 + 4.38in^2 + 9.63in^2 + 13.63in^2)} = 145lb \qquad (A.56)$$

where: P - overturn load, l - vertical distance from overturn line to center of gravity, d_k - distance from overturn line to location of interest, d_i -distance from overturn line to row i

These reactions are one order of magnitude less than the failure loads for AN3 (10-32) screws, suggesting large margins against failure.

A.5.3 Pump Installation

The pump is installed to the base plate of the support frame using four ¼-28 cap screws. When subject to the 9g forward load factor, the reactions are as illustrated in Figure A.13.
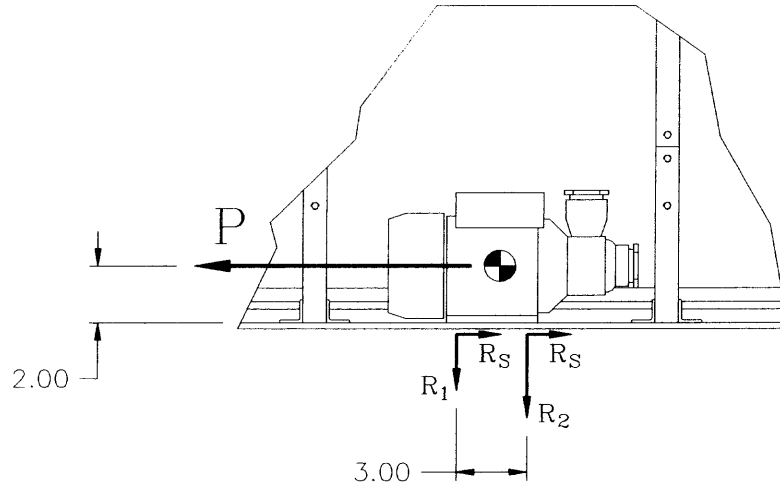
Figure A.13 Pump installation. Loads.

The direct shear acting on each of the four screws is computed as:

$$R_{S,direct} = \frac{P}{n} = \frac{9g(15.3lb)}{4} = 34lb \tag{A.57}$$

The tensile load associated with the overturn moment is computed as:

$$R_2 = \frac{Pld_k}{2\sum_i d_i^2} = \frac{9g \cdot 15.3lb \cdot 2.00in \cdot 3.44in}{2 \cdot (0.44in^2 + 3.44in^2)} = 40lb \tag{A.58}$$

These reactions are two orders of magnitude less than the failure loads for ¼-28 cap screws, suggesting large margins against failure.

A.5.4 Frame Analysis

The function of the frame structure is primarily to guard against inadvertent contact between personnel and components of the cooling tank system, and most attachments of the components are made directly to the base plate. However, the installation of the stop rail (to provide for partial restraint of the coolant tank) and the accumulator restraint impose loads on the structural components of the frame. It is noted that the stop rail imposes a load on the frame only when the load factor acts parallel to the long axis of the tank. In addition, the weight of the frame structural components must be supported. The loads from these components, leading to determination of the effects on the frame, are illustrated in Figure A.14.
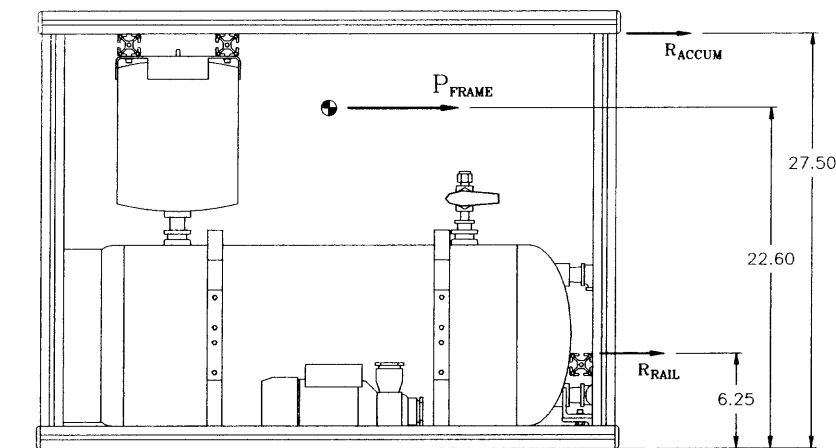
Figure A.14 Loads acting on the frame.

The load resulting from the frame structural components, P (19.3 lb), and the location of the CG (22.60 in.) are computed from known properties of the components and the geometry of the frame assembly. The reaction at the stop rail was determined in paragraph 3.2 as .62*(188.3 lb) = 116.7 lb, and the reaction at the accumulator restraint

was determined in paragraph 3.1 as 1.65 lb (14.9 lb when adjusted for the 9g load factor).

Based on these values, the moment applied to the frame under application of the 9g

forward load factor is calculated as:

$$M = 9g \cdot (116.7lb \cdot 6.25in + 19.3lb \cdot 22.60in + 1.65lb \cdot 27.50in) = 10900lb - in \qquad \text{(A.59)}$$

This moment load is supported by four corner connections between the vertical

members and the base members. The manufacturer's specification for the strength of this

joint is given as 4200 lb-in, and for four such joints the failure load is computed as 16800

lb-in. Comparing the applied load to the maximum strength of the joint system:

$$MS = \frac{16800lb - in}{1.5 \cdot 10900lb - in} - 1 = 0.03 \qquad \text{(A.60)}$$

The 9g forward load factor also imposes a shear load on the joints. The

magnitude of the load on application of the 9g forward load factor is obtained as:

$$R_S = 9g(116.7lb + 19.3lb + 1.65lb) = 1239lb \qquad \text{(A.61)}$$

The manufacturer's specification for the shear strength of this joint is given as

1200 lb, and for four such joints the failure load is computed as 4800 lb. Comparing the

applied load to the maximum strength of the joint system:

$$MS_{US} = \frac{4800lb}{1.5 \cdot 1239lb} - 1 = 1.6 \qquad \text{(A.62)}$$

A.5.5 KC-135 Interface Loads

The coolant tank/pump support frame interfaces with the KC-135 structure through the

support frame base plate, by means of four $^3/_8$-24 aircraft grade studs, one at each corner.

Assuming that the 9g forward load factor imposes the greatest load on this interface, the

reactions are illustrated in Figure A.15. Note that, because the interface plate is installed

on spacers in the aircraft, two of the interface studs lie on the heeling line, and the tension load reaction to the overturn moment only occurs in the two studs not located on the heeling line.
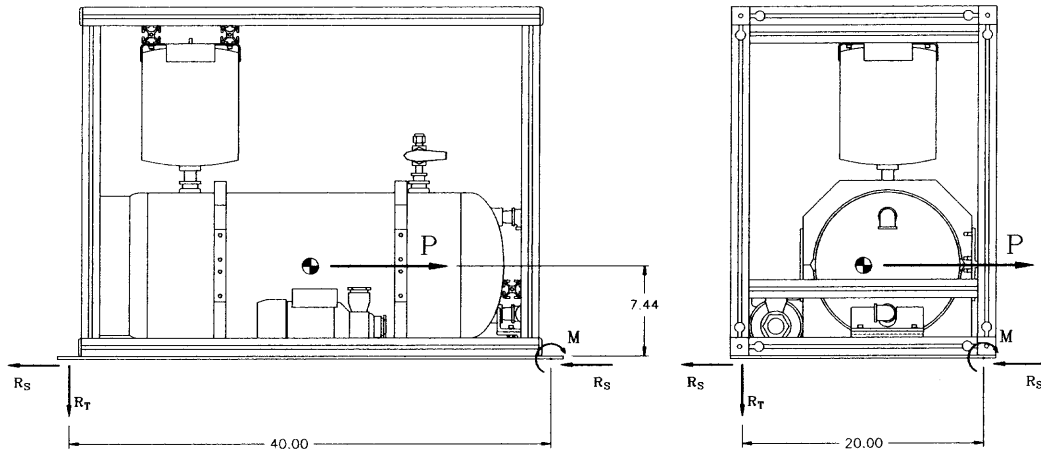
Figure A.15 KC-135 interface loads.

The 9g forward load factor induces a shear load in the studs, the magnitude of which is independent of the orientation of the support rack. The shear load per stud is calculated as:

$$R_S = \frac{9g \cdot 260.9lb}{4} = 587lb \tag{A.63}$$

When the forward load factor acts parallel to the long axis of the support rack, the reaction to the overturn moment is determined as (refer to dimensions of the left-hand view in Figure A.15):

$$R_T = \frac{Pld_k}{2\sum_i d_i^2} = \frac{9g \cdot 260.9lb \cdot 7.44in \cdot 40.00in}{40.00in^2} = 218lb \tag{A.64}$$

When the forward load factor acts perpendicular to the long axis of the support

rack, the reaction to the overturn moment is determined as (refer to dimensions of the right-hand view in Figure A.15):

$$R_T = \frac{Pld_k}{2\sum_i d_i^2} = \frac{9g \cdot 260.9lb \cdot 7.44in \cdot 20.00in}{2 \cdot 20.00in^2} = 437lb \qquad (A.65)$$

The tensile stress in the stud resulting from this load is obtained as:

$$\sigma = \frac{P}{A} = \frac{437lb}{0.0809in^2} = 5400psi \qquad (A.66)$$

The shear stress in the stud from the 9g load factor is calculated as:

$$\tau = \frac{P}{A} = \frac{587lb}{0.0878} = 6686psi \qquad (A.67)$$

Determining the principal stresses on the basis of Mohr's circle analysis:

$$\tau_1 = \sqrt{\left(\frac{5400psi}{2}\right)^2 + (6686psi)^2} = 7210psi$$

$$\sigma_1 = \left(\frac{5400psi}{2}\right) + \sqrt{\left(\frac{5400psi}{2}\right)^2 + (6686psi)^2} = 9910psi \qquad (A.68)$$

Comparing these principal stresses to the material strength for the studs (S_{UT} = 125ksi, S_{YT} = 100 ksi, S_{US} = 75 ksi):

$$MS_{UT} = \frac{125ksi}{1.5 \cdot 9910psi} - 1 = 7.4 \qquad MS_{YT} = \frac{100ksi}{9910psi} - 1 = 9.1$$

$$MS_{US} = \frac{75ksi}{1.5 \cdot 7210psi} - 1 = 5.5 \qquad (A.69)$$

The shear load induces a bearing stress in the material of the base plate, the magnitude of which is determined as:

$$\sigma_{BR} = \frac{P}{A} = \frac{587lb}{0.375in \cdot 0.25in} = 6261psi \qquad (A.70)$$

This stress value is one order of magnitude less than the bearing strength of the

6061-T6 Aluminum plate (S_{BRU} = 88000 psi, S_{BRY} = 58000 psi), suggesting large margins against failure.

A.5.6 Liquid Retention Panels

The volume of cooling water contained in the coolant tank could present a significant hazard if a leak occurs. In order to mitigate such an event, panels are installed to the support rack so that the entire volume of water (15 gal.) may be contained in the event of a gross leak (see Figure A.16). These panels are sealed with RTV to create a water-tight containment.
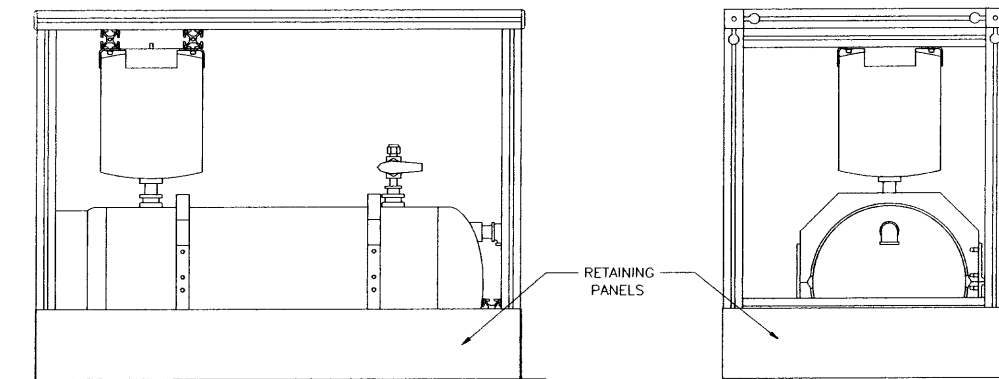
Figure A.16 Retaining panel configuration.

APPENDIX B

LABVIEW VIRTUAL INSTRUMENT

The LabVIEW 5.1 Virtual Instrument (VI) custom designed software that was used for the control of the experiments is described below.

The main Virtual Instrument 'Laser Control' provides the control panel for the experimentalists (Figure B.1). It consists of standard subVIs which are part of LabVIEW 5.1 package, and nonstandard ones created by the user. Only nonstandard subVIs are described here. For each subVI, the general information about the purpose and functions of the subVI is given, then the connector pane is shown, the controls and indicators are described, and, finally, the block-diagram of each subVI is presented. The list of all subVIs used in the Virtual Instrument completes this chapter.

B.1 'Laser Control' Virtual Instrument.

This VI is used with the National Instrument data acquisition board DAQ 6062 and has several functions:

1. Control of the data acquisition on the analog input channels of the board. The analog data acquisition must be initiate by digital trigger.

2. Generating digital pulse on the corresponding board otput (counter output). This pulse was used to gate the CO_2 laser and trigger the data acquisition thus synchronizing the laser activation with data acquisition.

3. Generating another digital pulse. This pulse was used in the experiments to activate the quenching mechanism. It was triggered by the high-to-low transition of the laser

gate pulse which allowed to synchronized the end of the laser heating with the quenching.

4. Assigning a number to each experiment.

5. Saving data into the text file.
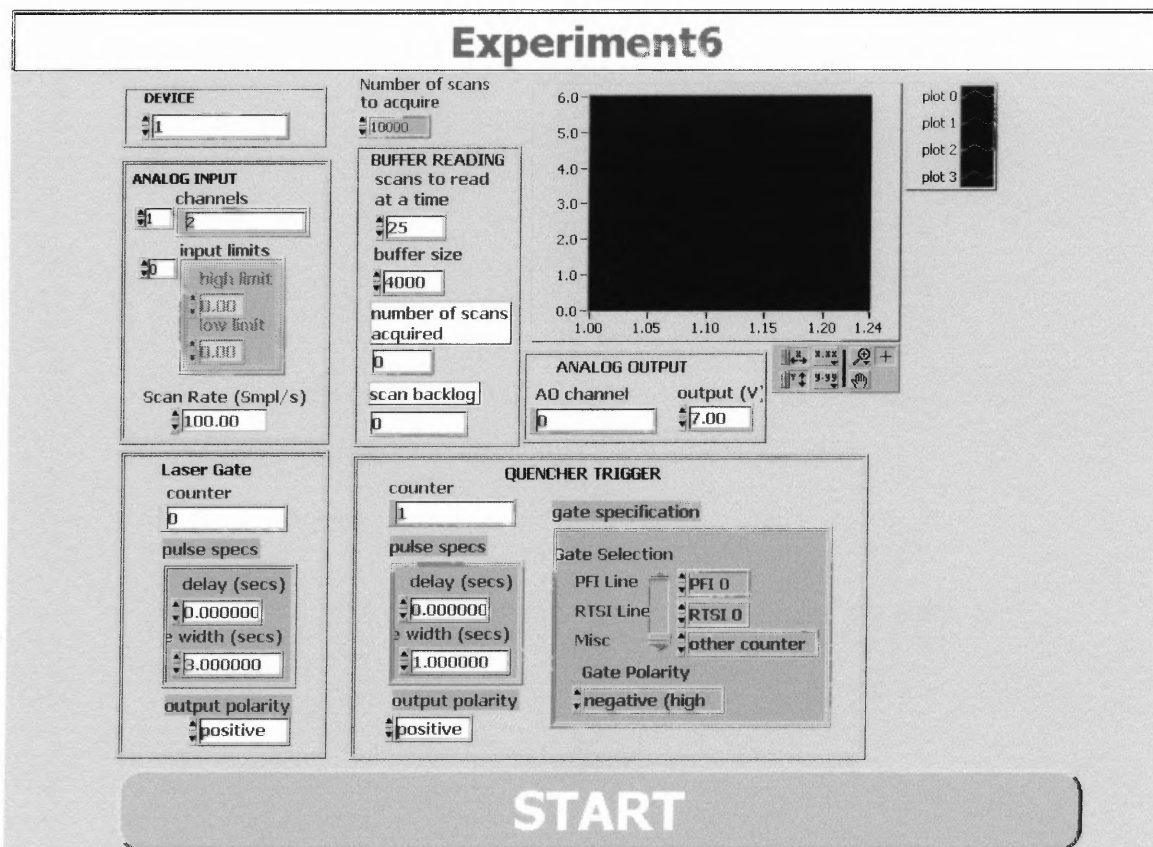
Figure B.1 The front panel of the 'Laser Control' Virtual Instrument.

Table B.1 Controls and indicators of the 'Laser Control' Virtual Instrument.

I16	**Device** The device number you assigned to the plug-in DAQ board during configuration. This parameter defaults to 1.

Analog Input

Table B.1 (Continued)

[F⋅b]	**Analog Input** The list of the analog input channels used, their input limits,and the scan rate.
[abc]	**Channels** The list of the analog channels used.
[⊡0s]	**Input limits** Enter the input limits settings for the channels selected in the "channels" array control. This determines the input measurement range that each channel is configured for. Leave this empty for hardware default configuration. Each element of this array corresponds to each element of the channel array, and same input limits setting will apply to all channels listed in each element of the channel array. If you need a different input limits setting for each individual channel, they must be listed separately in the channels array, one channel per element.
[SGL]	**High Limit** The upper limit of the input measurement range.
[SGL]	**Low Limit** The lower limit of the input measurement range.
[SGL]	**Scan Rate** The rate, in samples per second, at which you wish to acquire and write to the input channels. The default settings is 100 samples/sec.

Analog Output

[abc]	**AO Channel** Data acquisition board output channel that controls the laser power. The default value is 0.
[DBL]	**Output, V** AO channel voltage. 1 V of the analog output corresponds to 10% of the laser power. The default value is 5V (50 % of the laser power).

Laser Gate

Table B.1 (Continued)

[F.b]	**Laser Gate** The laser gate signal parameters: counter, pulse specifications, and pulse output polarity.
[abc]	**Counter** The number of the counter you want to use for the laser gate signal generation and for the data acquisition triggering. The default input is 0. The counter number must be different from the 'quencher trigger' counter.
[905]	**Pulse Specs** The laser gate signal specifications: pulse width and delay.
[DBL]	**Width** The width of the laser gate pulse in seconds.
[DBL]	**Delay** The delay of the laser gate pulse in seconds.
[U16]	**Output Polarity** The polarity of the laser gate pulse. This polarity can be positive or negative. The default value is 'positive'.

Quencher Trigger

[F.b]	**Quencher Trigger** The quencher trigger pulse parameters: counter, pulse specifications, and pulse output polarity. The pulse activates the quencher. The pulse generation must be in turn triggered by another pulse. By default the quencher trigger pulse is triggered by the high-to- low transition of the laser gate signal thus ensuring the synchronization of the laser and quencher operations.
[abc]	**Counter** The number of the counter you use for the quencher trigger pulse generation. The default input is 1. The counter number must be different from the 'laser gate' counter.
[905]	**Pulse Specs** The quencher trigger signal specifications: pulse width and delay.

Table B.1 (Continued)

`DBL`	**Width** The width of the quencher trigger pulse in seconds.
`DBL`	**Delay** The delay of the quencher trigger pulse in seconds.
`U16`	**Output Polarity** The polarity of the quencher trigger pulse. This polarity can be positive or negative. The default value is 'positive'.
`enu`	**Gate Specification** The source and polarity of the pulse that triggers the quencher trigger pulse.
`U16`	**Gate Polarity** The polarity of the pulse that triggers the quencher trigger pulse. It is positive by default.
`U32`	**Gate Selection** The selected gate of the counter, i.e. the input of the pulse that triggers the quencher trigger pulse. The default value is 'other counter'.
`I32`	**PFI Line** PFI n, where n=0-9 or default.
`U16`	**RTSI Line** RTSI n, where n=0-6
`I32`	**Misc** Options: in start trigger, in stop trigger, other counter output, low..

Buffer Reading

`I32`	**Buffer Size** This is the size of the internal acquisition buffer in scans. Data is stored in this buffer as it is acquired. If you are acquiring more data than will fit in the buffer, the buffer acts as a circular buffer, filling more than once. In this case, faster acquisitions need larger buffers so the data is not overwritten before you have a chance to read it from the buffer. The size of the buffer is limited by the amount of memory available. The default value is 4000.
`I32`	**Scans to Read at a Time** The number of scans to read from the acquisition buffer at each loop iteration. To keep up with a fast acquisition that is filling

Table B.1 (Continued)

the buffer quickly, you might need to read more data from the buffer each time. The default value is 25.

[I32] **Number of Scans Acquired** Number of scans that were acquired by this VI.

[U32] **Scan Backlog** Scan backlog is the amount of data remaining in the buffer after this VI completes. If scan backlog increases steadily, you are not reading data fast enough to keep up with the acquisition, and your newly-acquired data may overwrite unread data. Decrease the scan rate, increase the number of scans to read, read the scans more often, or increase the buffer size.

[I32] **Number of Scans to Acquire** Number of scans you want this VI to acquire.

[abc] **Experiment Number** The number of the experiment which increases by 1 each time the 'start-stop' switch initiates the laser gate signal generation and data acquisition process.

[⌗] **Transposed Waveform Graph** This waveform graph displays the data acquired on the specified channels.

[TF] **Start-Stop Switch** The switch that initiates or terminates the laser gate signal generation and data acquisition processes. This switch has two states: 'OFF' - the switch is unpressed, the caption 'start' appears on the switch, the program is awaiting the command to start the laser gate signal generation and data acquisition processes. 'ON'-the switch is pressed, the caption 'stop' appears on the switch. The laser gate signal is being generated and the data are being acquired. Each time the switch is pressed it changes its state.
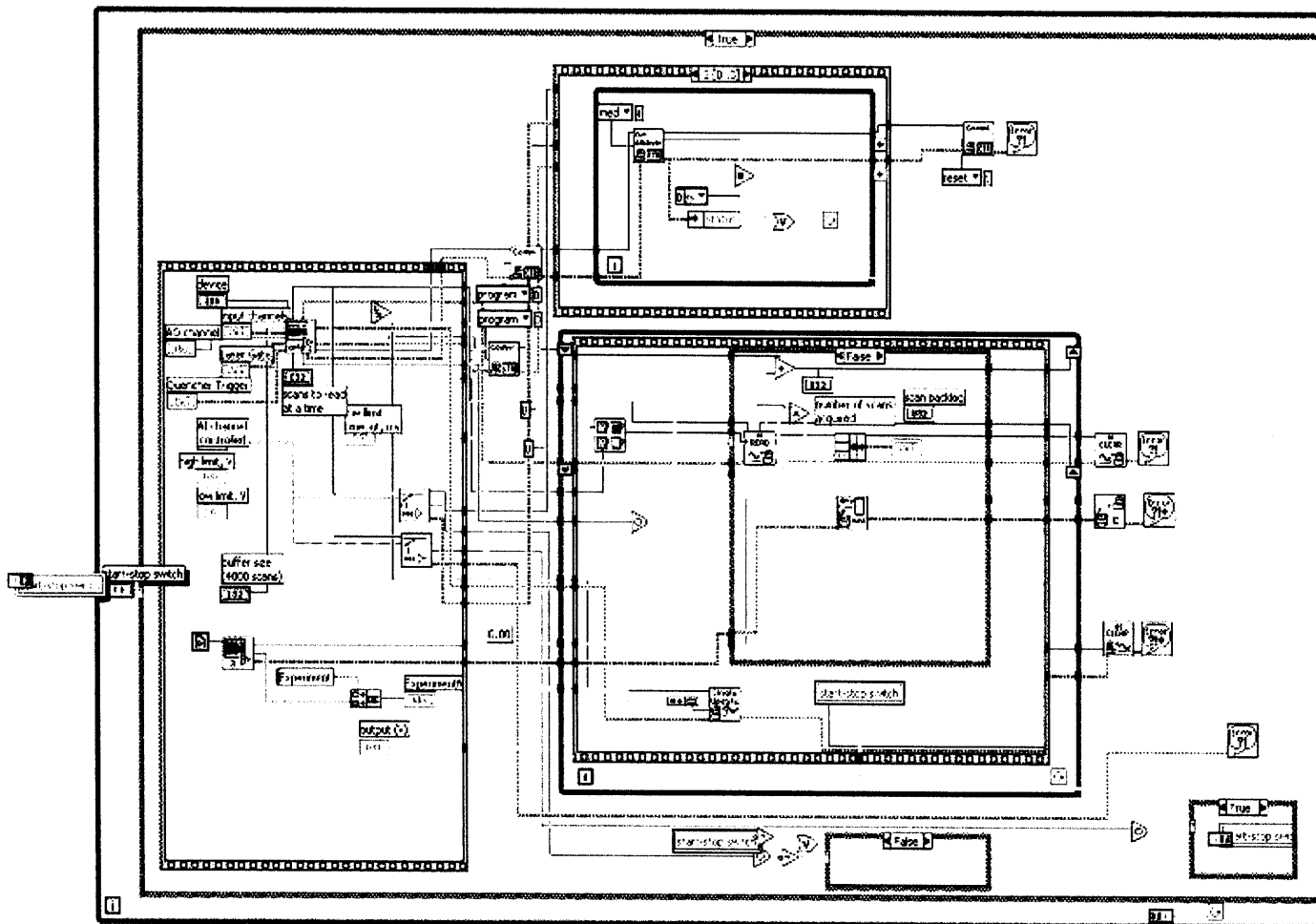
Figure B.2 The block-diagram of the 'Laser Control' Virtual Instrument.
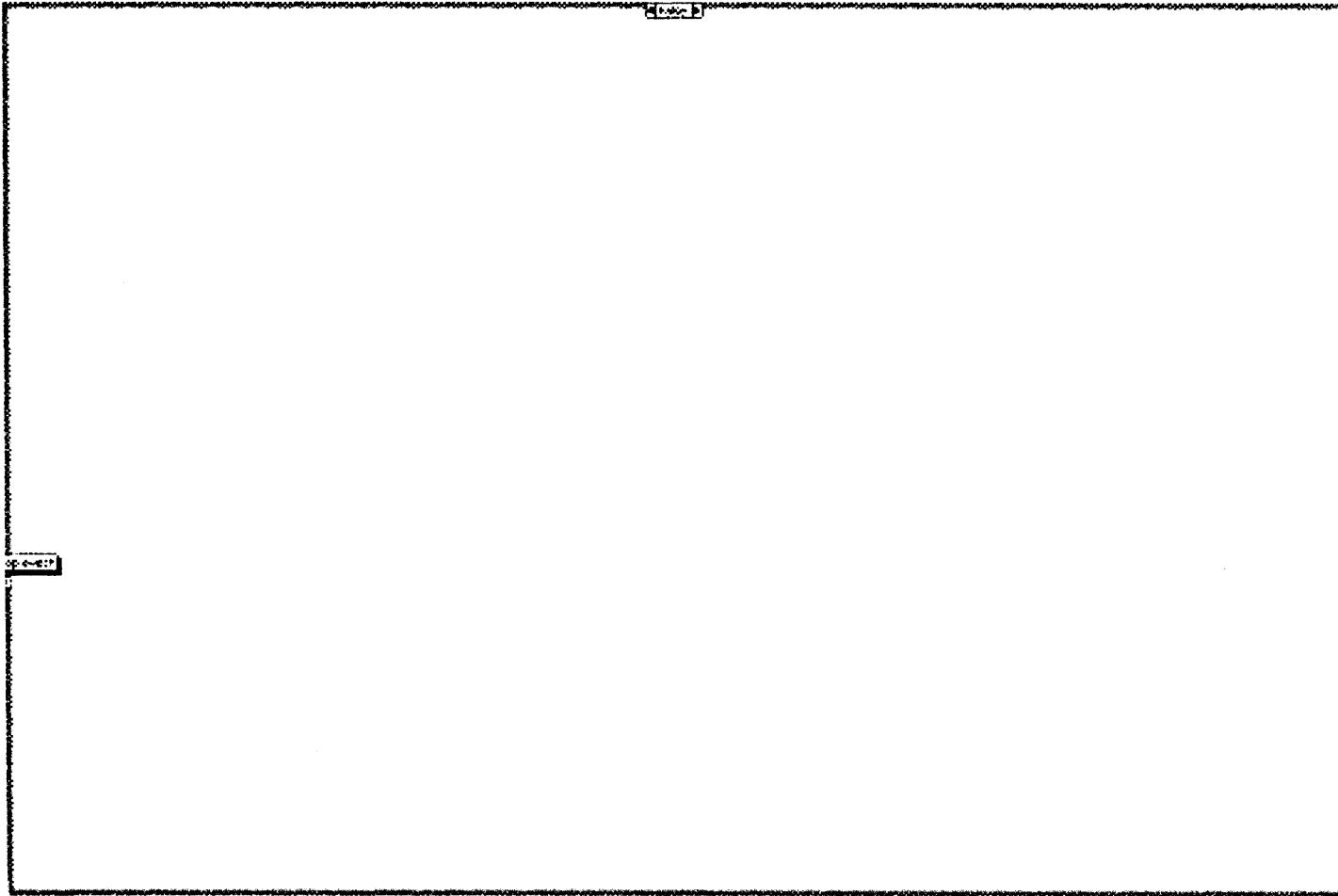
Figure B.3 The block-diagram of the 'Laser Control' Virtual Instrument. (Continued)
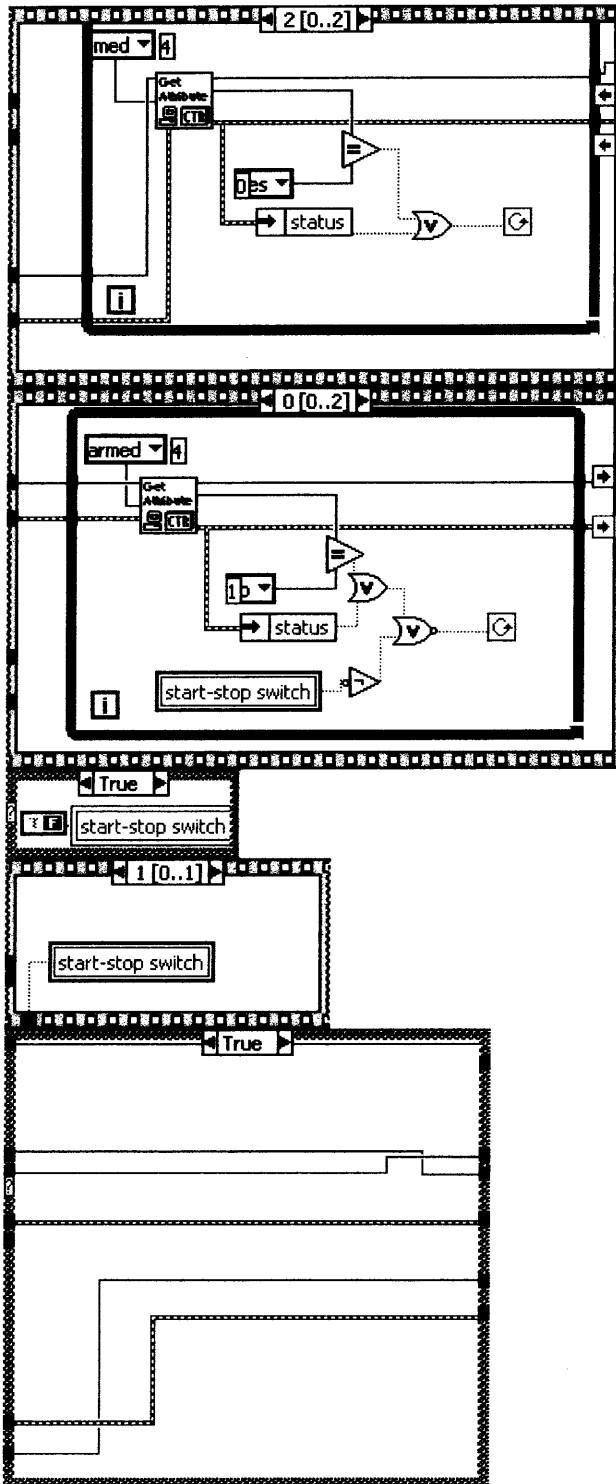
Figure B.4 The block-diagram of the 'Laser Control' Virtual Instrument (Continued).

B.2 'Configuration' SubVI

This vi configures the analog input channels, the analog output channel and the counters, i.e. the laser gate pulse and the quencher trigger pulse generators.
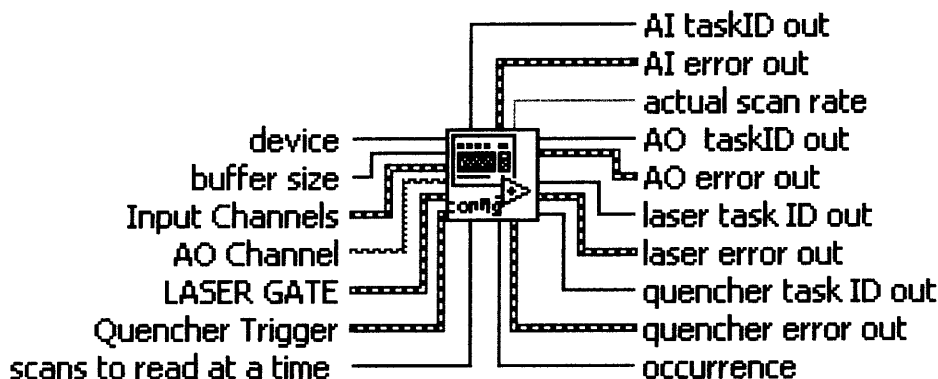

Figure B.5 The connector pane of the 'Configuration' subVI.

Table B.2 Controls and indicators of the 'Configuration' SubVI.

AO Channel cf. 'Laser Control' Virtual Instrument description, Table B.1.	
Quencher Trigger cf. 'Laser Control' Virtual Instrument description, Table B.1.	
Input Channels cf. 'Laser Control' Virtual Instrument description, Table B.1.	
Device cf. 'Laser Control' Virtual Instrument description, Table B.1.	
Laser Gate cf. 'Laser Control' Virtual Instrument description, Table B.1.	
Scans to Read at a Time cf. 'Laser Control' Virtual Instrument description, Table B.1.	
Buffer Size cf. 'Laser Control' Virtual Instrument description, Table B.1.	
Quencher Task ID Out Uniquely identifies the device, group and I/O operations of the counter that generates the quencher trigger pulse.	

Table B.2 (Continued)

[F.B]	**AO Error Out** AO error out contains error information of the analog output channel configuration. If the error in cluster indicated an error, the error out cluster contains the same information. Otherwise, error out describes the error status of this VI.
[U32]	**AO TaskID Out** Uniquely identifies the device, group and I/O operations of the analog output channels.
[F.B]	**Laser Error Out** Laser error out contains error information of the laser gate counter configuration. If the error in cluster indicated an error, the error out cluster contains the same information. Otherwise, error out describes the error status of this VI.
[U32]	**Laser Task ID Out** Uniquely identifies the device, group and I/O operations of the counter that generates the laser gate pulse.
[F.B]	**Quencher Error Out** Quencher error out contains error information of the quencher trigger pulse counter configuration. If the error in cluster indicated an error, the error out cluster contains the same information. Otherwise, error out describes the error status of this VI.
[F.B]	**AI Error Out** AI error out contains error information of the analog input channel configuration . If the error in cluster indicated an error, the error out cluster contains the same information. Otherwise, error out describes the error status of this VI.
[U32]	**AI TaskID Out** Uniquely identifies the device, group and I/O operations of the analog input channels.

Table B.2 (Continued)

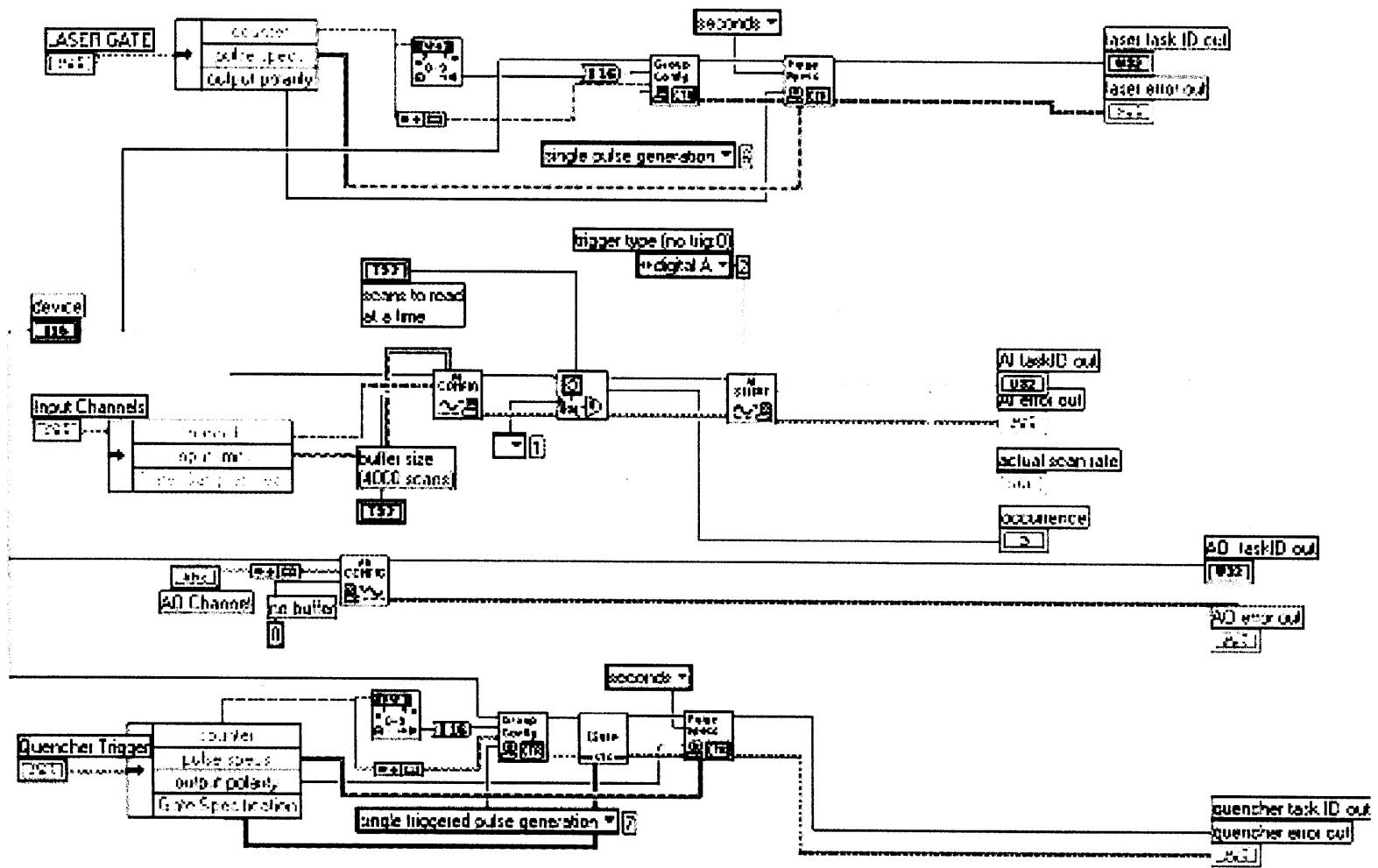|	
`SGL`	**Actual Scan Rate** Actual scan rate may differ slightly from the requested scan rate, depending on the hardware capabilities.
`D`	**Occurrence** The occurrence that is set by the following event: the number of scans equal to the value of 'Scans to Read at a Time' control was acquired..

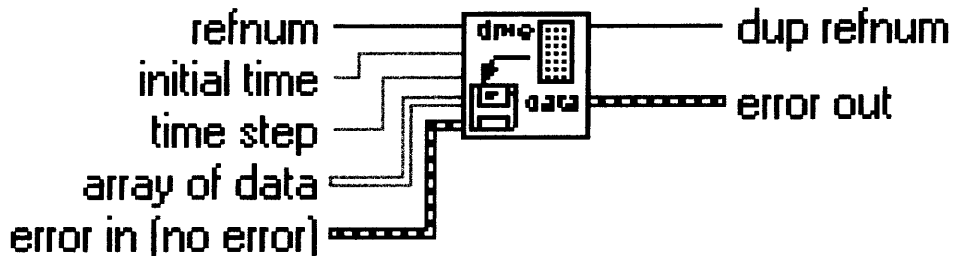**Figure B.6** The block-diagram of the 'Configuration' Virtual Instrument.

B.3 'Time Data To Spreadsheet' SubVI.

This VI takes the array of data, composes the cooresponding array of time and writes the data

and the time into a text file. As a result, the text file contains data in the columns arranged in

the following order:

array1   array2   array3   ...   time

....

....

Figure B.7 The connector pane of the 'Time Data To Spreadsheet' subVI.

Table B.3 Controls and indicators of the 'Time Data To Spreadsheet' subVI.

[□]	**Refnum** Refnum is the reference number of the open file. The value is Not A Refnum if the file cannot be opened.
[DBL]	**Initial Time** Initial time value.
[DBL]	**Time step** Interval between two consecutive moments of time.
[[DBL]]	**Array of Data** 2x2 array of data
[⊡]	**Error In** Error in describes error conditions occurring before this VI executes. If an error already occurred, this VI does not start the acquisition.

Table B.3 (Continued)

|	
🔲	**Dup Refnum** Dup refnum is the flow-through parameter with the same value as refnum.
🔲	**Error Out** Error out contains error information. If the error in cluster indicated an error, the error out cluster contains the same information. Otherwise, error out describes the error status of this VI.
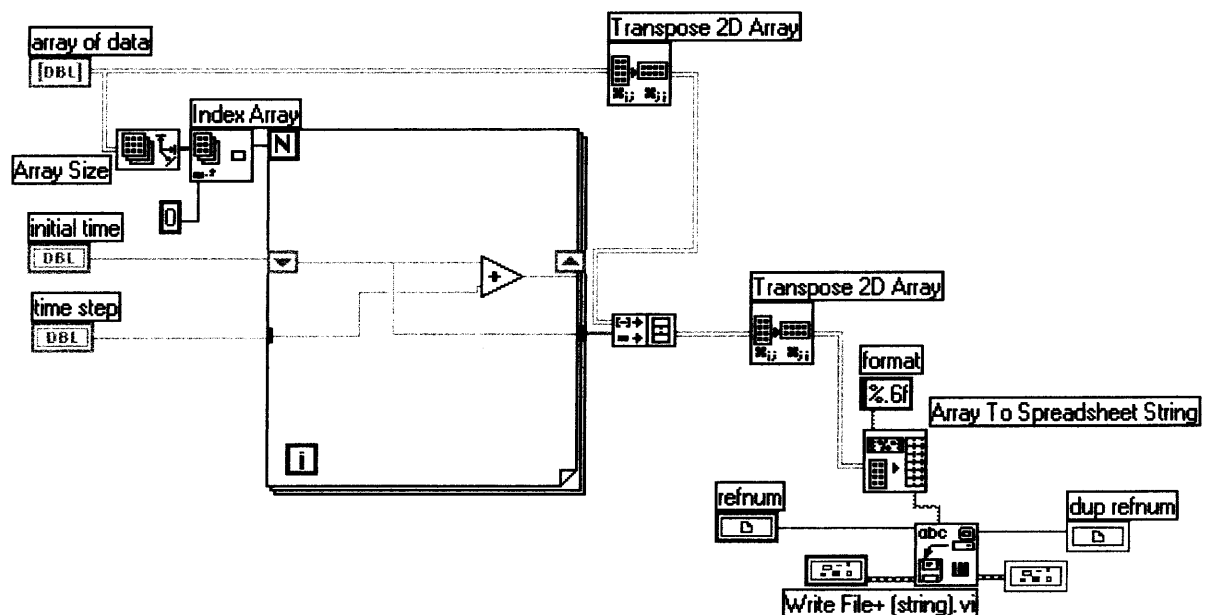
Figure B.8 The block-diagram of the 'Time Data To Spreadsheet' subVI.

B.4 'MyCreateOpenTextFile' SubVI.

This VI creates the ExperimentTracker.my file where the date and the number of the experiment are stored. It calls the 'Define Experiment Number' subVI that determines the current date and the number of the experiment. The VI also creates and opens a new text file. The name of the file is ^^run**.txt, where ^^ - the date when the experiment was performed,

**- the number of the experiment. For example, if the current experiment is #5, and the date

is February 15, the file 15run05.txt will be created and opened.
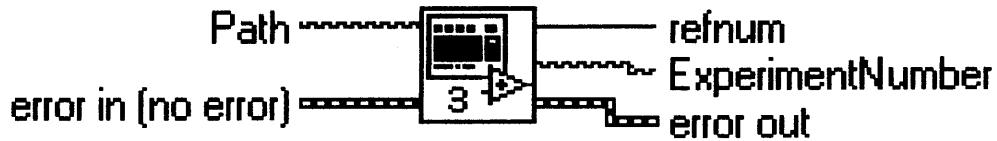
Figure B.9 The connector pane of the 'MyCreateOpenTextFile' subVI.

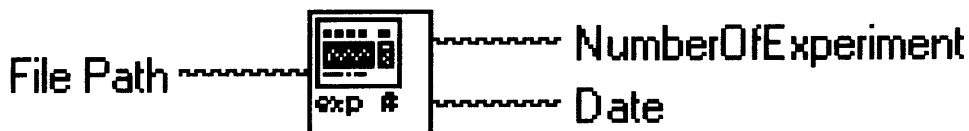**Table B.4** Controls and indicators of the 'MyCreateOpenTextFile' subVI.

	Path The path of the ExperimentTracker.my file, and the path of the file that will be created and opened.
	Error In The cluster can accept error information wired from VIs previously called. Use this information to decide if any functionality should be bypassed in the event of errors from other VIs.
	Error Out The cluster passes error or warning information out of a VI to be used by other VIs.
	Refnum Refnum is the reference number of the open file. The value is Not A Refnum if the file cannot be opened.
	ExperimentNumber The number of the experiment.
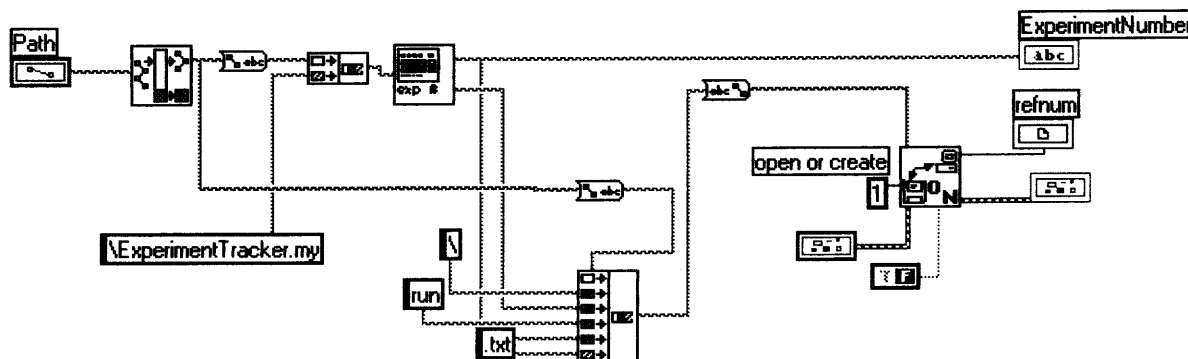
Figure B.10 The block-diagram of the 'MyCreateOpenTextFile' subVI.

B.5 'Define Experiment Number' SubVI

This VI determines the date when the experiment is being performed and the number of the experiment. This information is stored in the file determined by the 'File Path' control. The VI reads the date from this file and compares it with the current date according to the computer system. If the dates coincide, the number of experiment increases by one, this new value is assigned to the 'NumberOf Experiment' indicator and the new experiment number is saved into the file. Otherwise, the number of experiment is set equal to one and both the new date and the experiment number are saved into the file. The indicator 'NumberOfExperiment' acquires the value one.

Figure B.11 The connector pane of the 'DefineExperimentNumber' subVI.

Table B.5 Controls and indicators of the 'DefineExperimentNumber' subVI.

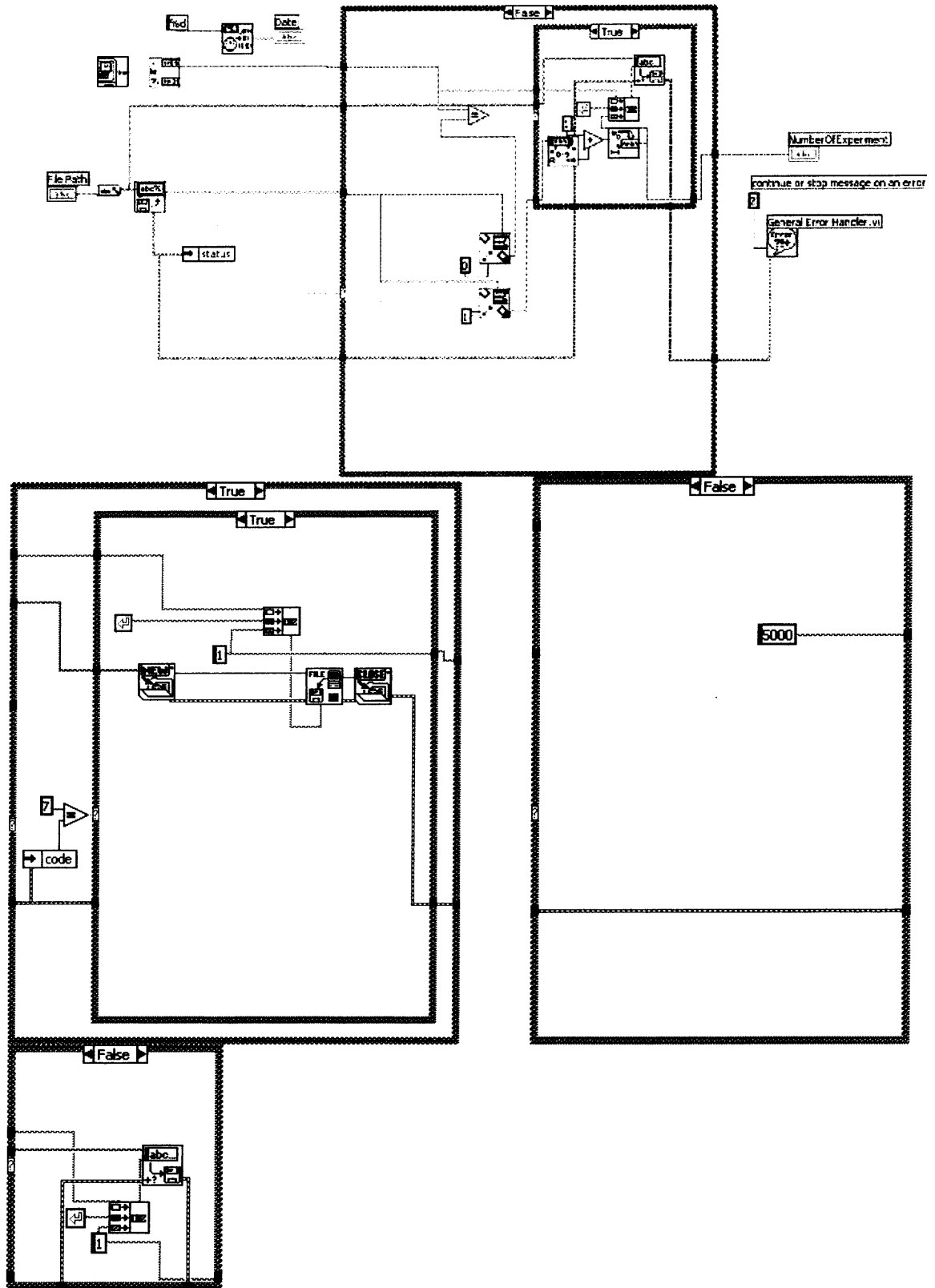|	
[abc]	**File Path** The path to the file where the date and the number of experiment are stored.
[abc]	**NumberOfExperiment** The number of the experiment.
[abc]	**Date** The date when the experiment is being performed.

Figure B.12 The block-diagram of the 'DefineExperimentNumber' subVI.

B.6 'My Open Read Lines From File' Virtual Instrument

This VI is the standard *Read Lines From File.vi* with the only change : the *error out* control

is added.

B.7 'MyWrite Characters To File' Virtual Instrument

This VI is slightly changed standard *Write Characters To File.vi*: 'Error in' control and the

'Error Out' indicator are added, and no advisory dialog appears when the VI is performed.

B.8 List of SubVis.

Table B.6 List of subVIs that are called directly by the 'Laser Control' Virtual Instrument.
Dots stand for the current Labview directory.

Icon	SubVI	Path
	Counter Control.vi	...\vi.lib\daq\zadvdctr.llb\Counter Control.vi
	Simple Error Handler.vi	...vi.lib\Utility\ERROR.LLB\Simple Error Handler.vi
	AI Read.vi	...\vi.lib\daq\ai.llb\AI Read.vi
	AI Clear.vi	...\vi.lib\daq\ai.llb\AI Clear.vi
	AO Single Update.vi	...\vi.lib\DAQ\zadvd.llb\AO Single Update.vi
	AO Clear.vi	...\vi.lib\daq\ao.llb\AO Clear.vi
	General Error Handler.vi	...\vi.lib\Utility\error.llb\General Error Handler.vi

Table B.6 (Continued)

Icon	SubVI	Path
	Counter Gate (STC).ctl	...\EXAMPLES\DAQ\Counter\DAQ-STC.llb\Counter Gate (STC).ctl
	MyCreateOpenTextFile.vi	...\user.lib\MyCreateOpenTextFile.vi
	Time Data To Spreadsheet.vi	...\user.lib\Time Data To Spreadsheet.vi
	Close File+.vi	...\vi.lib\Utility\file.llb\Close File+.vi
	Configuration.vi	...\user.lib\Configuration.vi
	DAQ Occurrence Config.vi	...\vi.lib\daq\misc.llb\DAQ Occurrence Config.vi
	Counter Get Attribute.vi	...\vi.lib\DAQ\zadvdctr.llb\Counter Get Attribute.vi

APPENDIX C

RECONSTRUCTION OF 3D POSITION OF A POINT BY TRIANGULATION

3D coordinates of a point can be reconstructed from two video camera images of this point by 'triangulation' method which is briefly considered below.

The video cameras are supposed to be calibrated, i.e. their internal and external parameters are known. For convenience, we'll cal two cameras 'the left camera' and 'the right camera' with the following relations between their reference frames and the world reference frame:

$$\mathbf{X}_L = \mathbf{R}_L \mathbf{X}_W + \mathbf{T}_L \qquad (C.1)$$

$$\mathbf{X}_R = \mathbf{R}_{RL} \mathbf{X}_L + \mathbf{T}_{RL} \qquad (C.2)$$

where subscript L stands for the left camera reference frame, and subscript R means the right camera reference frame, W – the world reference frame, $\mathbf{X}$ –coordinates of the point in the corresponding reference frame. $\mathbf{R}$ and $\mathbf{T}$ are the matrices of rotation and translation accordingly. The mirror image that we used instead of the second camera can be treated as a 'virtual camera', and the same relations (C.1), (C.2) are true for this 'virtual camera' with the only difference that the corresponding matrix $\mathbf{R}$ includes both rotation and transformation.

The following distortion model is used:

$$\begin{pmatrix} x_{d1} \\ x_{d2} \end{pmatrix} = \begin{pmatrix} \dfrac{X_c}{Z_c} \\ \dfrac{Y_c}{Z_c} \end{pmatrix} + (s_1 r^2 + s_2 r^4 + s_5 r^6) \begin{pmatrix} \dfrac{X_c}{Z_c} \\ \dfrac{Y_c}{Z_c} \end{pmatrix} + \mathbf{dx} \qquad (C.3)$$

where the term in brackets is the radial distortion,

150

$$r = \left(\frac{X_c}{Z_c}\right)^2 + \left(\frac{Y_c}{Z_c}\right)^2 \qquad (C.4)$$

and

$$\mathbf{dx} = \begin{pmatrix} 2s_3 \dfrac{X_c Y_c}{Z_c^2} + s_4\left(r^2 + 2\dfrac{X_c^2}{Z_c^2}\right) \\[4mm] s_3\left(r^2 + 2\dfrac{Y_c^2}{Z_c^2}\right) + 2s_4 \dfrac{X_c Y_c}{Z_c^2} \end{pmatrix} \qquad (C.5)$$

is the tangential distortion, s_1, s_2, s_2, s_3, s_4, s_5 are distortion coefficients. x_{d1} and x_{d2} are the components of the distorted coordinates.

The distorted coordinates $\mathbf{x_d}$, are found from the pixel coordinates of projection of the point on camera images using Eq. (4.5), and we need to find $\mathbf{x_n}$.using Eqs. (C.3)-(C.5). The problem is nonlinear and to solve it, the following iterative approach was used (Heikkila and Silven, 1997, Heikkila, 2000):

$$\mathbf{x_n^0} = \mathbf{x_d} \qquad (C.6)$$

$$\begin{pmatrix} \dfrac{X_C}{Z_C} \\[3mm] \dfrac{Y_C}{Z_C} \end{pmatrix}^i = \frac{1}{\left(1 + s_1 r^2 + s_2 r^4 + s_5 r^6\right)^{i-1}}\begin{pmatrix} x_{d1} \\ x_{d2} \end{pmatrix} - \mathbf{dx}^{i-1} \quad \text{for } i > 0 \qquad (C.7)$$

Here the superscript i stands for the iteration number. 20 iterations were used in the software. Using this procedure the normalized coordinates $\mathbf{x_{nl}}$ and $\mathbf{x_{nr}}$ of the reflector and the center of the sample in the left and the right camera reference frames correspondingly are found.

The 3D coordinates of the point can be found by triangulation method as illustrated in Figure C.2 (Shapiro and Stockman, 2001). Two vectors $\mathbf{x_{nl}}$ and $\mathbf{x_{nr}}$ determine two rays O_1P_1 and O_2P_2. The intersection of these rays would give the point in

3D space. Because of approximation errors in the camera model and image points, these rays will not actually intersect. The solution of this problem is to find such points P1 and P2 that P_2P_1 would be the shortest line segment connecting the rays O_1P_1 and O_2P_2. The following expression is true for the vector P_2P_1 in the left camera reference frame:

$$\mathbf{P_2P_1} = a\mathbf{x}_{nl} - b\mathbf{R}_{RL}^{-1}\mathbf{x}_{nr} - \mathbf{T}_{RL} \tag{C.8}$$

where a and b are some constants.
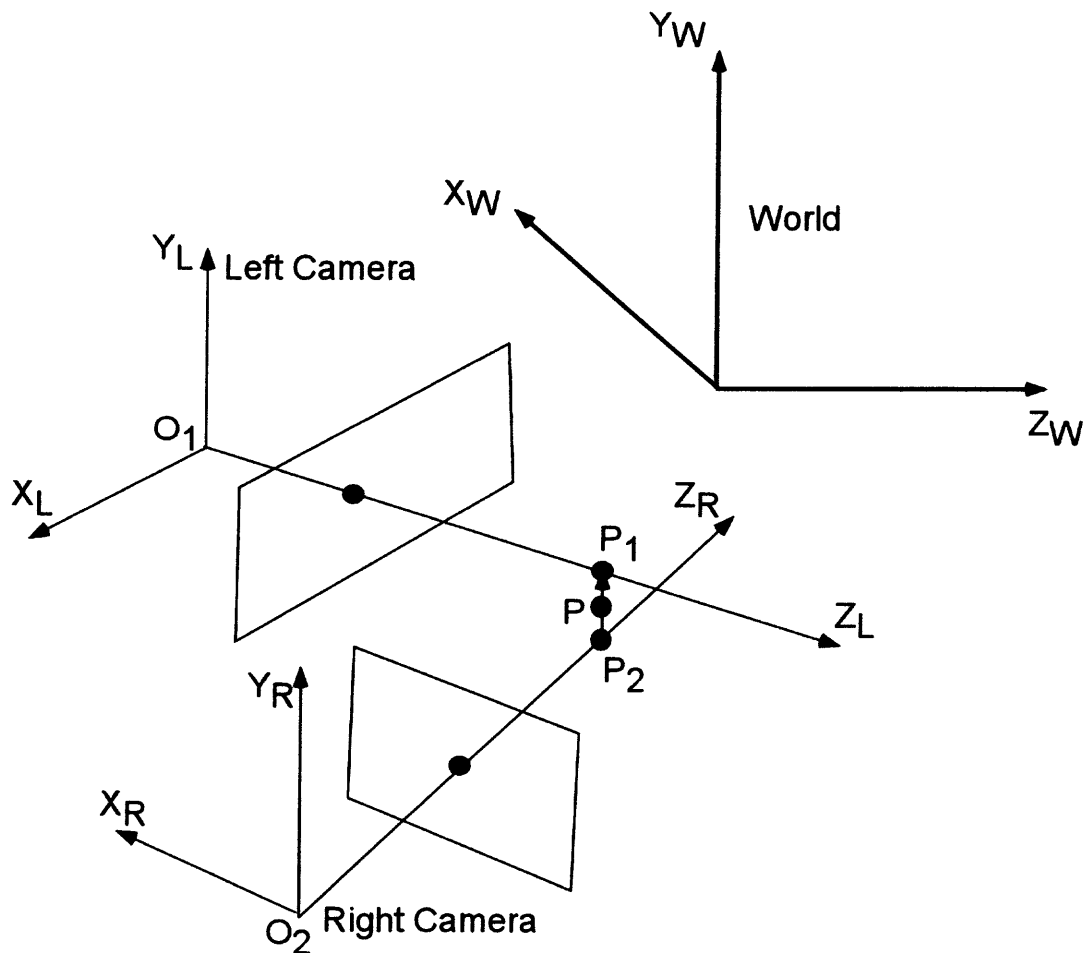
Figure C.1 The triangualation method of reconstruction of 3D coordinates of a point using two camera images.

On the other hand, the vector P_2P_1 is proportional to the vector product of the vectors x_{nl} and x_{nr} with some coefficient c :

$$\mathbf{P}_2\mathbf{P}_1 = c\mathbf{x}_{nl} \times \mathbf{R}_{RL}^{-1}\mathbf{x}_{nr} \qquad (C.9)$$

It follows from Eqs.(C.8), (C.9) that:

$$a\mathbf{x}_{nl} - b\mathbf{R}_{RL}^{-1}\mathbf{x}_{nr} - \mathbf{T}_{RL} = c\mathbf{x}_{nl} \times \mathbf{R}_{RL}^{-1}\mathbf{x}_{nr} \qquad (C.10)$$

Solving these equations relative to a, b, c, we find the points P1 and P2 in the left camera reference frame. The midpoint P of the segment P_1P_2 vector can be considred as the approximation of the intersection of the rays O_1P_1 and O_2P_2 with the accuracy equal to the half of the length of P_1P_2. The coordinates of this point can be transformed into the world reference frame using Eq. (C.1):

$$\mathbf{X}_W = \mathbf{R}_L^{-1}(\mathbf{X}_L - \mathbf{T}_L) \qquad (C.11)$$

REFERENCES

1. Abbud Madrid A,. and Branch M.-C. (November 6, 1997). A study of heterogeneous and homogeneous combustion of bulk metals in a reduced-gravity environment. *Bull. Soc. Chim. Belgique, 106,* 331-336.

2. Abriata, J. P., Versaci, R., and Garces, J. (1986). The O-Zr (oxygen - zirconium) system. *Bull. Alloy Phase Diagrams, 7,* 116-124.

3. Ansell S., Krishnan S., Weber J. K. R., Felten J. J., Nordine P. C., Beno M. A., Price D. L., and Saboungi M. - L. (1997). Structure of liquid aluminum oxide. *Phys. Rev. Lett., 78,* 464-466.

4. Aoyama T., Takamura Y., and Kuribayashi K. (1998). Containerless solidification of Se-Ge binary alloy by means of laser heating electromagnetic levitation. *Jpn. J. Appl.Phys., 37,* L687-L690.

5. Arai Y., Paradis P. - F., Aoyama T., Ishikawa T., and Yoda S. (2002). An aerodynamic levitation system for drop tube and quenching experiments. *Rev. Sci. Instrum., 74,* 1057-1063.

6. Awatani J. (1955). Studies on acoustic radiation pressure: I. General considerations. *J. Acoust. Soc. Am., 27,* 278-280.

7. Awatani J. (1957). Note on acoustic radiation pressure, *J. Acoust. Soc. Am., 29,* 392.

8. Babin F., Gagné J. - M., Paradis P. - F, Coutures J. - P., and Rifflet J. - C. (1995). High temperature containerless laser processing of dielectric samples in microgravity - study of aerodynamic trapping. *Micrograv. Sci. Technol., 7,* 283-289.

9. Belyansky M., Trenary M., and Ellison S. (1995). Boron chemical shifts in B_6O. *Surface Science Spectra, 3,* 147-150.

10. Bouguet J. Y. (2000). Matlab camera calibration toolbox [Computer Software]. TRCalTech.

11. Branch M. C., Abbud-Madrid A., and Daily J.W. (1997). The effect of gravity on the combustion of bulk metals. *The Fourth International Microgravity Combustion Workshop, NASA Conf. Publ. 10194,* 31-36.

12. Brown D. C.. (1966). Decentering distortion of lenses. *Photometric Engineering, 32* 444-462.

13. Brown D. C. (1971). Lens distortion for close-range photogrammetry. *Photometric Engineering*, 37, 855-866..

14. Chase Jr. M. W. (Ed.). (1988). *NIST-JANAF termochemical tables*. American Chemical Society, American Institute of Physics for the Natural Institute of Standard and Technology.

15. Chiacci F. T., Crane K. M., and Badwal S. P .S. (1994). Evaluation of commercial zirconia powders for solid oxide fuel cells. *Solid State Ionics*, 73, 49 -61.

16. *CRC handbook of chemistry and physics*. (1997). New York: CRC Press.

17. Dobreva A., and Gutzow I. (1997). Kinetics of vitrification under electric fields. *J. Non-Cryst. Solids*, 220, 235-242.

18. Dreizin E. L., Suslov A. V., and Trunov M. A. (1993). General trends in metal particles heterogeneous combustion. *Combust. Sci. Techn.*, 90, 79-99.

19. Dreizin E. L. (1996). Experimental study of stages in aluminum particle combustion in air. *Combust. Flame*, 105, 541-556.

20. Dreizin E. L., Keil D. G., Felder W., and Vicenzi E. P. (1997). On the mechanism of boron ignition. *1997 JANNAF Combustion Subcommittee, Propulsion Systems Hazards Subcommittee and Airbreathing Propulsion Subcommittee Joint Meeting*.

21. Dreizin E. L. (1998). Experimental study of aluminum particle evolution in normal and micro-gravity. *Combust. Flame*, 116, 323-333 .

22. Dreizin E. L., Keil D. G., Felder W., and Vicenzi E. P. (1999). Phase changes in boron ignition and combustion. *Combust. Flame*, 119, 272-290.

23. Dreizin E. L., and Hoffmann V. K. (1999). High-temperature phases in ternary Zr-O-N systems. *J. Mater. Res.*, 14, 3840-3842.

24. Dreizin E. L. (2000). Phase changes in metal combustion. *Prog. Energy Combust. Sci.*, 26, 57-78.

25. Enderby J. E., Ansell S., Krishnan S., Price D. L., and Saboungi M. - L. (1997). The electrical conductivity of levitated liquids. *Appl. Phys. Lett.*, 71, 116-118.

26. Fujii H., Matsumoto T., and Nogi K. (2000). Analysis of surface oscillation of droplet under microgravity for the determination of its surface tension. *Acta Materialia*, 11, 2933-2939.

27. Gammel P.M., Cronquist A.P., and Wang T.G. (1988). A high-powered siren for stable acoustic levitation of dense materials in the Earth gravity. *J. Acoust. Soc. Am*, *83*, 496-501.

28. Gao J. R., Gao C.D., and Wei B. (1999). Containerless processing of materials by acoustic levitation. *Adv. Space Res.*, *24*, 1293-1297.

29. Glorieux B., Millot F., Rifflet J .- C., and Coutures J. - P. (1999). Density of superheated and undercooled liquid alumina by a contactless method. *Int. J. Thermophys.*, *20*, 1085-1094.

30. Glorieux B., Saboungi M. - L., Millot F., Enderby J., and Rifflet J. -C. (2001). Aerodynamic levitation: An approach to microgravity. *Space Technology and Applications International Forum – 2001. AIP Conference Proceedings:* Vol. **552.** Albuquerque, New Mexico:American Institute of Physics.

31. Gor'kov L. P. (1962). Forces acting on a small particles in a sound field in an ideal fluid. *Sov. Phys. Dokl. 6*, 773-775.

32. Gribaudo, L., Arias, D., and Abriate J. P. (1994). *J. Phase Equilibria*, *15*, 441-449.

33. Heikkilä, J., and Silvén, O. (1997)/ A Four-step camera calibration procedure with implicit image correction. *IEEE Computer Society Conference on Computer Vision and Pattern Recognition (CVPR'97), San Juan, Puerto Rico,* 1106-1112.

34. Heikkilä J. (2000). Geometric camera calibration using circular control points. *IEEE Trans. On Pattern Analysis And Machine Intelligence*, *22*, 1066-1076.

35. Hennet L., Thiaudière D., Gailhanou M., Landron C., Coutures J. -P., and Price D. L. Fast x-ray scattering measurements of molten alumina using a 120° curved position sensitive detector. *Rev. Sci. Instrum.*, *73*, 124-129.

36. Ishikawa T., Paradis P. -F., and Yoda S. (2001). New sample levitation initiation and imaging techniques for the processing of refractory metals with an electrostatic levitator furnace. *Rev. Sci. Instrum.*, *72*, 2490-2495.

37. Ishikawa T., Paradis P. –F., Itami T., and Yoda S. (2003). Thermophysical properties of liquid refractory metals: Comparison between hard sphere model calculation and electrostatic levitation measurements. *J. Chem. Phys.*, *18*, 7912-7920.

38. Jones H. (1999.) Rapid Solidification. In C. Suryanarayana (Ed.), *Non-equilibrium processing of materials* (pp.22-45). Oxford: Pergamon.

39. Kartha S., and Grimes P. (1994). Fuel cells. Energy conversion for the next century. *Physics Today*, *11*, 54-61.

40. Kelton K. F., Lee G. W., Gangopadhyay A. K., Hyers R. W., Rathz T. J., Rogers J. R., Robinson M. B., and Robinson D. S. (2003). First X-ray scattering studies on electrostatically levitated metallic liquids: demonstrated influence of local icosahedral order on the nucleation barrier. *Phys. Rev. Lett.*, *90*, 195504-1 - 195504-4.

41. Kervalishvili P.J., Oganezov K.A., Tabutsidze M.L., and Andriasova I.A. (1992). Hydrogen, nitrogen, and oxygen behavior in boron. *J.Mater. Res.*, *7*, 1822-1828.

42. Kim Y. J., Busch R., Johnson W. L., Rulison A. J., and Rhim W. K. (1994). Metallic glass formation in highly undercooled $Zr_{41.2}Ti_{13.8}Cu_{12.5}Ni_{10.0}Be_{22.5}$ during containerless electrostatic levitation processing. *Appl. Phys. Lett.*, *65*, 2136 –2138.

43. King L. V. (1934). On the acoustic radiation pressure on spheres. *Proc. Roy. Soc. (London) A*, *147*, 212-240.

44. King, M. K. (1993). In Kuo K. K. and Pein R. (Eds.), *Combustion of boron-based solid propellants and solid fuels* (pp. 1–80). Boca Raton: CRC Press,.

45. Kobayashi K.F. (1999). in Suryanarayana (Ed.), *Non-equilibrium Processing of Materials* (p.93). Oxford: Pergamon.

46. Kofstad P. (1988). *High temperature corrosion.* London: Elsevier.

47. Landron C., Hennet L., and Coutures J.-P. (1982). Aerodynamic laser-heated contactless furnace for neutron scattering experiments at elevated temperatures. *Rev. Sci. Instrum.*, *71*, 1745-1751.

48. Landron C., Hennet L., Jenkins T.E., Greaves G.N., Coutures J.P., and Souper A.K. (2001). Liquid alumina: detailed atomic coordination determined from neutron diffraction data using empirical potential structure refinement. *Phys. Rev. Lett.*, *86*, 4839-4842.

49. Landron C., Hennet L., Thiaudiere D., Price D.L., and Greaves G.N. (2003). Structure of liquid oxides at very high temperatures. *Nucl. Instr. And Meth. B.*, *199*, 481-488.

50. Langen M., Hibiya T., Eguchi M., and Egry I., (1998). Measurement of the density and the thermal expansion coefficient of molten silicon using electromagnetic levitation. *J.Cryst. Growth*, *186*, 550-556.

51. Lee M.C. and Feng I. (1982). Acoustic levitating apparatus for submillimeter samples. *Rev. Sci. Instrum.*, 53, 854-859.

52. Lee C.P. and Wang T.G. (1984). The acoustic radiation force on a heated (or cooled) rigid sphere – theory. *J. Acoust. Soc. Am*, 75, 88-96.

53. Lee C.P. and Wang T.G. (1988). Acoustic radiation force on a heated sphere including effects of heat transfer and acoustic streaming. *J. Acoust. Soc. Am*, 83, 1324-1331.

54. Lerch, M., Füglein, E., and Wrba, J. (1996). Synthesis, crystal structure, and high temperature behavior of Zr_3N_4. *Zeitschrift für Anorganische und Allgemeine Chemie*, 62, 367-372.

55. Lerch, M. (1998). Phase relationships in the Zr_2-Zr_3N_4 system, *J. Mater. Sci.*, 17, 441-443.

56. Leung E. W., and Wang T.G. (1985). Force on a heated sphere in a horizontal plane acoustic standing wave field. *J. Acoust. Soc. Am*, 77, 1686-1691.

57. Levinsky I. V. (1990). *P-T-X binary phase diagrams of metal systems.* Moscow: Metallurgia (In Russian).

58. Li D. L., Volkmann T., Eckler K., and Herlach D. M. (1995). Crystal growth in undercooled germanium. *J. Cryst. Growth*, 152, 101-104.

59. Li S. C. (1990). *Ph.D. thesis.* Princeton University.

60. Li S. C., and Williams, F. A. (1990). *Twenty-Third International Symposium on Combustion*, Pittsburgh, PA, pp. 1147–1154.

61. Massalski T. B., Okamoto H., Subramanian P.R., and Kasprzak L. (Eds). (1990). *Binary alloy phase diagrams.* Materials Park, OH: ASM Publ..

62. McDaniel J.G., and Holt R.G. (2000). Measurement of aqueous foam rheology by acoustic levitation. *Phys. Rev. E, 61*, R2204-R2207.

63. Molodetsky I.E., Dreizin E.L., and Law C.K. (1997). Evolutionof particle temperature and internal composition for zirconium burning in air. *Twenty-Sixth Symposium (Int'l) on Combustion*, The Combustion Institute, Pittsburgh, pp. 1919-1927.

64. Molodetsky I. E., Vicenzi E. P., Dreizin E. I., and Law C. K. (1998). Phases of titanium combustion in air. *Combust. Flame, 112*, 522-532.

65. Nakamura T., Awa Y., Shimoji H., and Karasawa H. (2002). Control system of electrostatic levitation furnace. *Acta Astronautica, 50*, 609–614.

66. National Aeronautics and Space Administration Lyndon B. Johnson Space Center, Houston. (2003, February). *Experiment design requirements and guidelines, NASA 931 KC135 A.* Retrieved June 5, 2003 from NASA Web site: http://jsc-aircraft-ops.jsc.nasa.gov/kc135/docs/AOD_33897.pdf.

67. National Aeronautics and Space Administration Lyndon B. Johnson Space Center, Houston. *NASA Glenn safety manual.* Retrieved June 5, 2003 from NASA Web site: http://smad-ext. grc.nasa.gov /gso/ manual/ chapter_index. shtml.

68. National Aeronautics and Space Administration Lyndon B. Johnson Space Center, Houston. (2003, February). *Test equipment data package requirement and guidelines, NASA JSC RGO.* Retrieved June 5, 2003 from NASA Web site: http://jsc-aircraft-ops.jsc.nasa.gov/kc135/docs/AOD_33896.pdf.

69. Nelson L.S., and Richardson N.L. (1964). The use of flash heating to study the combustion of liquid metal droplets. *J. Phys. Chem., 68,* 1268-1270.

70. Nelson L.S.. (1965). Nature of the spearpoints observed during the combustion of zirconium droplets. *Nature, 207,* 741.

71. Nelson L.S., Rosner D.E., Kurzius S.C., and Levine H.S. (1968). Combustion of zirconium droplets in oxygen/rare gas mixtures – kinetics and mechanism. *Twelfth Symposium (International) on Combustion.* The Combustion Institute, Pittsburgh, PA, 59-70.

72. Notthoff C., Franz H., Hanfland M., Herlach D. M., Holland-Moritz D., Jacobs G., Lippok R., Petry W., and Platzek D. (1999). Energy dispersive X-ray diffraction on undercooled metallic melts. *J.Non-Cryst. Solids, 250-252,* 632-636.

73. Okamoto H., and Massalsky T.B. (1994). *Journal of Phase Equilibria, 15,* 500.

74. Olsen H., Wergeland H., and Westerwelt P.J. (1958). Acoustic radiation force. *J. Acoust. Soc. Am., 30,* 633-634.

75. Paradis P.-F., Babin F., and Gagné J. - M. (1996). Study of the aerodynamic trap for containerless laser materials processing in microgravity. *Rev. Sci. Instrum., 67,* 262-270.

76. Paradis P.F., Babin F., Gagné J. - M., and Lévesque S. (1997). Analysis of the fluorescence of a ND-doped 50% CaO-50% Al_2O_3 glass, pumped at 810 nm, between 1050 and 1100 nm. *J. Opt. Soc. Am. B, 14,* 1009-1012.

77. Paradis P.–F., Ishikawa T., and Yoda S. (2003). Noncontact density measurements of tantalum and rhenium in the liquid and undercooled states. *Appl. Phys. Lett.*, *83*, 4047-4049.

78. Powder Diffraction File PDF-2. (1988). JCPDS ICDD, Newton Square, PA.

79. Price E.W. (1984). In K.K.Kuo and M.Summerfield (Eds.), *Fundamentals of solid propellant combustion* (pp. 479-514) New York:AIAA.

80. Rhim W. K., Collender M., Hyson M.T., Simms W.T., and Elleman E. (1985). Development of an electrostatic positioner for space material processing. *Rev. Sci. Instrum.*, *56*, 307-317.

81. Rhim W. K., Chung S. K., Barber D., Man K. F., Gutt G., Rulison A., and Spjut R. E. (1993). An electrostatic levitator for high temperature containerless materials processing in 1-g. *Rev. Sci. Instrum.*, *64*, 2961-2970.

82. Rhim W. K. and Ohsaka K. (2000). Thermophysical properties measurement of molten silicon by high-temperature electrostatic levitator: density, volume expansion, specific heat capacity, emissivity, surface tension and viscosity. *J. Cryst. Growth*, *208*, 313-321.

83. Robey J. and Trinh E. (1983). Sample transport of levitated objects in a dual temperature resonance chamber. *J. Acoust. Soc. Am. Suppl.*, *74*, S27-S28.

84. Rogers J. R., Hyers R. W., Rathz T., Savage L., and Robinson M. B. (2001). Thermophysical property measurement and materials research in NASA/MFSC electrostatic levitator. *Space Technology and Applications International Forum – 2001, AIP Conference Proceedings, Vol. 552.* American Institute of Physics.

85. Saboungi M. - L., Enderby J., Glorieux B., Schnyders H., Sungaila Z., Krishnan S., and Price D. L. (2002). What is new on the levitation front? *J. Non-Cryst. Solids*, *312-314*, 294-298.

86. Schaefers K., Rösner-Kuhn M., and Frohberg M.G. (1995). Enthalpy measurements of undercooled melts by levitation calorimetry: the pure metals nickel, iron, vanadium and niobium. *Mat.Sci. Eng. A*, *197*, 83-90.

87. Schaefers K. and Frohberg M. G. (1996). Electromagnetic levitation and its application in high-temperature calorimetry. *Thermochimica Acta*, *271*, 75-84.

88. Schenk T., Holland-Moritz D., Bender W., and Herlach D. M. (1999). Statistical analysis of nucleation in undercooled Co-base alloys. *J. Non-Cryst. Solids*, *250-252*, 694-698 (1999).

89. Shapiro L.G., Stockman G.S. (2001). *Computer vision*. Upper Saddle River: Prentice Hall, Inc.

90. Stratton S.A. (1941). *Electromagnetic theory*. New York:McGraw-Hill.

91. Sung Y. S., Takeya H., and Togano K. (2001). Containerless solidification of Si, Zr, Nb, and Mo by electrostatic levitation. *Rev. Sci. Instrum.*, *72*, 4419-4423.

92. Sung, Y.S., Takeya, H., Hirata, K., and Togano, K. (2003). Spherical Nb single crystals containerlessly grown by electrostatic levitation. *Appl. Phys. Lett.*, *82*, 3638-3640.

93. Suryanarayana C. (1991). Rapid solidification. In R. W. Cahn (Ed.) *Materials science and technology: Vol.15* (pp.57-110). New York: VCH Publishers Incorporated,.

94. Tian Y., Holt R. G., and Apfel R. E. (1995). A new method for measuring liquid surface tension with acoustic levitation. *Rev. Sci. Instrum.*, *66*, 3349-3354.

95. Toloukian K. S., Liley P. E., and Saxena S. C. (1970). *Thermophysical properties of matter: Vol.3*. New York: IFI/Plenum.

96. Trinh E. H., and Apfel R. E. (1980). Sound velocity of supercooled water down to -35°C using acoustic levitator. *J. Chem. Phys.*, *72*, 6731.

97. Trinh E.H., Wang T., and Robey J. (1981). A nonuniformly heated resonance chamber for levitation studies in air. *J. Acoust. Soc. Am. Suppl.*, *70,* S90.

98. Trinh E.H. (1985). Compact acoustic levitation device for studies in fluid dynamics and material science in the laboratory and microgravity. *Rev. Sci. Instrum. 56*, 2059-2065.

99. Trinh E.H. and Hsu C.J. (1986). Equilibrium shapes of acoustically levitated drops. *J. Acoust. Soc. Am*, *79*, 1335.

100. Trinh E.H., Robey J., Jacoby N., and Wang T. (1986). Dual-temperature acoustic levitation and sample transport apparatus. *J. Acoust. Soc. Am*, *79*, 604-612.

101. Weber J.K.R., John J., Cho F. B., and Nordine P. C. (1998). Glass fibres of pure and erbium- or neodymium-doped yttria-alumina compositions. *Nature*, *393*, 769-771.

102. Westerwelt P.J. (1951). The theory of steady forces caused by sound waves. *J. Acoust. Soc. Am.*, *23*, 312-315.

103. Whymark R.R. (1975). Acoustic field positioning for containerless processing. *Ultrasonics*, 13, 251-261.

104. Zehringer R., Kunzli H., Oelhafen P., and Hollenstein C. (1990). Oxidation behaviour of boron carbide. *J. Nucl. Mater.*, *176 & 177*, 370-374.

105. Zhang X. (1998). Solidification modes and microstructure of Fe–Cr alloys solidified at different undercoolings. *Mat. Science Eng.*, *A, 247*, 214-221.